Control of CO_2 Vibrational Dynamics via Shaped-Pulse Coherent Anti-Stokes Raman Spectroscopy

by

Adriaan Jacobus Hendriks

Thesis presented in partial fulfillment of the requirements
for the degree of

Doctor in Philosophy
(Laser Physics)

at the University of Stellenbosch

Supervisor:
Dr. Hermann Uys

Co-Supervisors:
Dr. Christine Steenkamp
Dr. Anton Du Plessis

March 2017

Declaration

I, the undersigned, hereby declare that the work contained in this thesis is my own original work and that I have not previously in its entirety or in part submitted it at any university for a degree.

.....
Signature

.....
Date

Abstract

In this work we investigate the coherent control of carbon dioxide (CO_2) vibrational dynamics using Coherent anti-Stokes Raman Scattering (CARS). During CARS, vibrational modes are excited via stimulated Raman scattering (SRS). Subsequently a narrowband probe field interacts with the molecular ensemble providing not only information about the modes populated, but also on the evolution of the wave-packet created during excitation. By spectrally shaping one of the SRS pump fields the vibrational dynamics can be controlled. In this work it was assumed that the pump pulse structure which will lead to a desired dynamics is unknown. To find that structure, a learning algorithm was developed which utilizes a spatial light modulator (SLM) in a 4f-optical configuration to spectrally shape the pump. Both a time-frequency representation of the shaped pulse (called the von Neumann basis) and a standard Fourier domain representation were bench-marked during optimization of a second harmonic generation (SHG) signal in a BBO crystal to ascertain which will suit the optimization problem best in terms of convergence rate and parameter space size. It was found that the von Neumann basis converged faster than the standard Fourier domain representation while still operating on a larger parameter space and therefore it was used in all subsequent work. In addition, we developed a quantum mechanical theoretical model of the CARS process to ensure proper understanding of our measurements. We demonstrated experimentally that mode excitation selectivity can be achieved using the pump fields extracted by the learning algorithm, and we explore the underlying selectivity mechanisms. Control of the relative phase of oscillation of different vibrational modes is also observed. Our work demonstrates coherent quantum control of all relevant aspects of the molecular vibrational dynamics of CO_2.

Opsomming

In hierdie werk ondersoek ons die koherente beheer van koolstofdioksied (CO_2) vibrasionele dinamika met behulp van koherente anti-Stokes Raman verstrooiing(KARV). Gedurende KARV word vibrasionele modusse opgewek deur middel van gestimuleerde Raman verstrooiing (GRV). Vervolgens meet n nou-bandwydte meet puls die molekulêre toestand asook die tydsontwikkeling van die golf-pakkie wat geskep is tydens opwekking. Deur een van die GRV velde spektraal te vervorm kan die vibrasionele dinamika beheer word. In hierdie werk is aanvaar dat die pomp puls struktuur wat sal lei tot 'n gewenste dinamika onbekend is. Om daardie struktuur te vind, word n leer algoritme ontwikkel wat n ruimtelike lig modulator (RLM) in 'n 4f-optiese opstelling gebruik om die pomp te vervorm. Beide 'n tyd-frekwensie voorstelling van die gevormde veld (bekend as die von Neumann basis) en 'n standaard Fourier voorstelling was getoets gedurende optimering van 'n tweede harmoniese opwekking (THO) in 'n BBO kristal om vas te stel wat die optimering probleem die beste sal pas in terme van konvergensie koers en parameter ruimte grootte. Daar is bevind dat die von Neumann basis vinniger konvergeer as die standaard Fourier verteenwoordiging terwyl dit op 'n groter parameter ruimte werk en is dus gebruik in alle werk wat daarop volg. Daarbenewens het ons 'n kwantummeganiese teoretiese model van die proses ontwikkel om behoorlike begrip van ons metings te verseker. Ons demonstreer eksperimenteel dat modus opwekking selektief gedoen kan word met behulp van die pomp velde verkry vanaf die leer algoritme, en ons ondersoek die onderliggende selektiwiteit meganismes. Beheer van die relatiewe fase van ossillasie van verskillende vibrasionele modusse is ook waargeneem. Ons werk toon kwantum beheer van alle relevante aspekte van die molekulêre vibrasionele dinamika van CO_2.

ACKNOWLEDGEMENTS

During my academic career several people contributed tremendously to the success of the work presented in this study for which I'm exceedingly grateful. First and foremost, I would like to thank Dr. Lourens Botha who would not accept that I would not finishing my PhD. Unfortunately he isn't with us anymore. I would like to extend gratitude towards my family and friends for their endless support and encouragement. In particular my mother and best friend Darryl Naidoo whom without I would have given up most likely at the beginning of this enormous fight. /midway of this work

I'm extremely grateful for my supervisor Dr. Hermann Uys who felt it distasteful (for a lack of better words) to present a PhD of not exceptional quality. I can distinctively remember numerous times spending after hours in the lab where he joint me in the hope of achieving the goals set out for this study. Thank you Dr. Uys for all your guidance and wealth of knowledge contributed towards this project. You surely are what a supervisor and scientist should set out to be. I also give thanks to my co-supervisors Dr. Christine Steenkamp and Dr. Anton Du Plessis for their efforts and aid with regards to the work presented here. I would like to extend my gratitude towards Dr. Steenkamp who as a person helped me translate the work presented here from complicated concepts into a language even the common folk (like myself) can understand.

A special thanks goes out to all the technical personal at the National Laser Centre. During my studies there weren't a single technician that did not play a role in the work presented here. I would like to thank Gary King, Hendrik Kloppers, Johan Stuyn, Henk, and anyone I might have accidently left out. You are the hart and soul of the NLC due to your selflessness and desire to help others.

Last but surely not least, I would like to thank the Lord my God whom without I would never have been able to do this.

My studies were funded by the Council for Scientific and Industrial Research (CSIR) under the National Laser Centre (NLC).

Contents

List of Figures

List of Tables

Chapter 1

Introduction and Overview

1.1 The Quest for Coherent Control

This thesis explores the use of temporally shaped ultrafast laser pulses for manipulating the vibrational dynamics of CO_2 molecules. The study lays the groundwork for our long term objective to manipulate chemical reaction dynamics by using light to prepare molecules in modes that favour particular chemical reaction pathways.

Indeed, some progress has been made in laser control of chemical reactions [4, 5, 6, 7]. In particular it was first demonstrated by Crim and co-workers that preparing the H-OD stretch mode to the 3rd overtone in combination with H atoms predominantly produced $H_2 + OD$ [8]. Other examples of vibrational state control of poly-atomic molecular reactions include $Cl + H_2O \rightarrow OH + HCl$ [9] as well as $Cl + HCN \rightarrow ClH + CN$ [10], just to name a few.

The coherent nature of light in principle allows the coherent control of the quantum mechanical wave function of molecules. This control is however in competition with decoherent phenomena such as ro-vibrational energy distribution, collisions, and spontaneous emission, which decrease the lifetime of laser-preprared quantum mechanical states and limits reaction control capabilities. Historically, these effects dampened the early hopes for a new era of light controlled chemical reactions. These challenges were partially circumvented with the advent of ultra-fast lasers which can excite molecular dynamics on time scales shorter than typical decay processes.

Controlling the outcome of a chemical reaction has always been a prime goal of chemists. The outcome of a reaction lies in one's ability to steer atoms and/or molecules from some initial state to a desired final state. Typically in industry these goals are primarily achieved using methods based on thermodynamics; exploiting thermodynamical laws and concepts to synthesize materials and manipulate reaction outcomes incoherently. However, at an early stage in the study of materials it became apparent that thermodynamics could not explain all the phenomena observed during interactions. Today we know chemical and light-matter interactions exhibit quantum mechanical behaviour where the particles are assumed wave-like in nature [11]. One such quantum mechanical behaviour is if there is an energy barrier to a

reaction in which hydrogen atoms are responsible for bond cleaving and/or bonds forming due to a quantum tunneling effect [12]. Another is laser control of a chemical reaction using quantum interference whereupon different reaction pathways lead to the same final state of the molecules [4]. Thermodynamics is not only unable to account for these effects but also lead to undesired byproducts during a chemical reaction because the processes are driven indirectly and not by the physical mechanism responsible for the reaction.

These quantum interference effects rely on coherence between different modes which left scientists with a different type of dilemma. Coherent excitations can only be achieved through the means of using coherent sources. As a pure form of energy as well as being coherent, lasers were considered as the perfect starting point to take advantage of the effects of coherence. However, the first few attempts made towards light induced coherent control were not as successful as anticipated. Clearly the way scientists approached the problem were flawed because it was assumed a narrowband laser tuned to a particular electronic excitation should excite the molecules leading to neutral reaction products. What was however found was ro-vibrational energy redistribution, due to short excited life-times, occurred before chemical reactions or photo-induced cation could occur [13]. It was not taken into consideration that the coherence between wavefunctions has limited lifetimes. Ro-vibrational redistribution is also not the only decoherent phenomena which can occur. It was also established that decoherence can take place due to relaxation from excited modes through collision with other particles as well as through spontaneous emission. It became clear for effective control it would be of no use trying to drive a coherent process with a source of which the pulse duration exceeds the time related to these quantum mechanical phenomena. The advent of pulsed laser sources proved invaluable in this regard which easily circumvented these problems due to their coherent attributes. In 1980, Ahmed Zewail, proposed using femtosecond pulses to overcome this obstacle for which he also received the Nobel prize in chemistry in 1999 for his contributions made towards femtochemistry [14].

Since the 1980s several approaches to quantum mechanical coherent control has been proposed and verified over time. In 1985 Tanner and Rice [15, 16] proposed a method using single or multiple pulses to manipulate quantum mechanical wave packets within a molecular ensemble. This method was first demonstrated in the early 1990s by the groups of Gerber and Zewail during multi-photon ionization [17, 18]. In 1986 Brumer and Shapiro proposed a scheme which exploits the interference between different pathways that connect initial and final states of the quantum mechanical system [19]. This was also demonstrated in 1990 for the first time by the group of D. S. Elliott [20]. The process of stimulated Raman adiabatic passage (STIRAP) was also demonstrated in 1988 [21]. Since then the successful control of various processes has been shown and their control dynamics established [5, 22].

In particular, the scientific community showed a strong interest in the work done by M. Dantus [23] illustrating the vibrational and rotational excitation of molecules using lasers. This opened up new avenues of research raising numerous questions of how different excitations can or might relate to chemical reactions and if it is possible to coherently control these? For example, if a particular reaction is strongly dependent on a particular reactant's mode would it be possible

to increase the product rate of this reaction while suppressing others and if so, to what extent? However, before one can address these questions effectively one should possess the tool set to do state preparation selectively.

1.2 Motivation and Objectives

Light-matter interaction can lead to rotational,vibrational and/or electronic excitations. In turn these can lead to molecular rearrangement, molecular cation or reaction with other molecules, to name a few. A large amount of effort has gone into theoretically finding the mechanisms for certain reactions to occur while others are suppressed [24, 12, 25, 26]. We know that many reactions are driven by the energetic states of molecules followed by collisions causing rearrangement of atoms and molecules. It has been shown that the reactivity of molecules are strongly influenced by vibrational and/or rotational excitations [27, 28, 29]. In particular, vibrationally exciting a molecule changes the position of the nuclei. During a chemical reaction one also observe a rearrangement of the nuclear position. The molecular state that carries the ensemble from its current arrangement to that of the product state is referred to as the reaction coordinate. Therefore, a chemical reaction will occur if a vibrational excitation directly maps onto the reaction coordinate of the reaction [30, 31]. This seldom occurs and for most cases a vibrational excitation will at best only closely resembles the reaction coordinate. This implies one requires knowledge of the reaction coordinate as well as knowledge of the reactant's state which will best map onto the reaction coordinate of a particular chemical reaction. It also implies one should possess the capability to selectively prepare molecules in this state. The transition to this optimal state does not have to be a single transition from initial to final, but might require several intermediate steps where the wave-packet is allowed to evolve. It should be noted that the mode which best map onto the reaction coordinate could be rotational, vibrational or electronic excitations. It can also be combinations and/or superpositions of these. Figure 1.1 shows a graphical representation of a typical chemical reaction requiring vibrational mode excitation for the chemical reaction to occur. In this particular case one reactant is vibrationally excited and then allowed to collide with another.

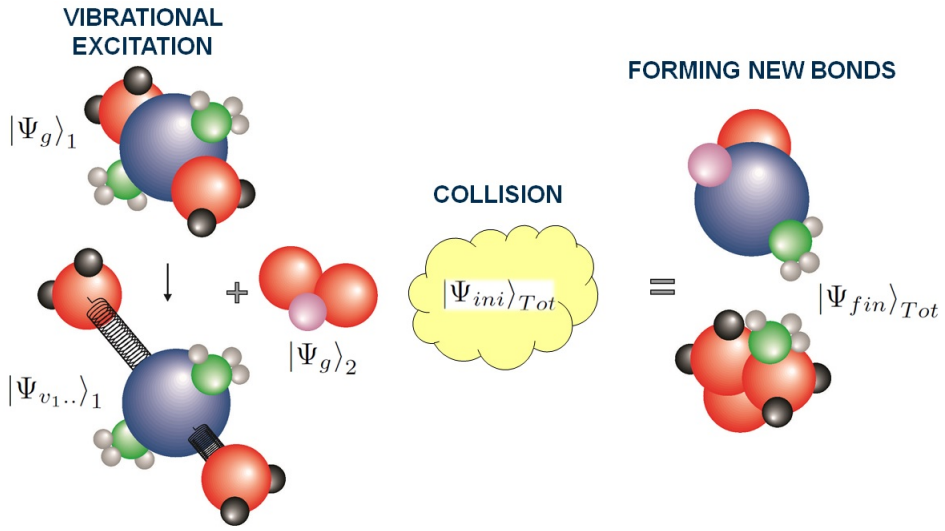

Figure 1.1: Graphical depiction of induced chemical reaction. This diagram illustrates how a molecule undergoes a vibrational excitation. This molecule is then allowed to interact via collision with other molecules which might lead to chemical rearrangements.

Electronic state preparation accompanied by vibrational excitation has been achieved numerous times due to the energies involved in electronic excitations closely resembled by the photon energies of laser sources available [32, 33]. However, vibrational and rotational mode preparation without electronic excitation require long wavelength (low energy) laser sources not so easily attainable. Therefore, not much thought has gone into vibrational state preparation.

The work presented here concentrates on achieving vibrational mode preparation making use of shaped ultrafast pulses. We focus our attention on selective vibrational excitation of two vibrational modes of CO_2 . Vibrational excitation is achieved making use of coherent anti-Stokes Raman scattering (CARS) which allows us to not only vibrationally excite the ensemble, but also measure the state occupied. Using a learning algorithm and pulse shaping we aim at selectively exciting the modes. We also investigate how the coherence between the modes can be influenced by pulse shaping. This investigation will provide answers to what extent quantum mechanical control of the molecular ensemble is achievable.

1.3 Pulse Shaping and Adaptive Control

The notion of laser pulse shaping has fascinated the scientific community dating back as far as the invention of the laser itself, and with good reason. Each pulse delivered by a femtosecond laser consists of a range of frequencies confined to a very short time interval. Pulse shapers are optical elements allowing one to change the amplitude or retard these frequencies relative to each other at will. The concept of arbitrarily changing the temporal and spectral characteristics of a pulse leaves us seemingly with an endless number of possible applications. Early attempts made towards pulse shaping were primarily achieved by chirping a pulse through an optical medium or using spectral filters to select certain spectral components which evidently also increase the

temporal width of the pulse [34]. Unfortunately, these approaches are only effective for certain quantum mechanical phenomena which do not rely on complex pulse structures. Dynamical control of molecules rely on the temporal control of laser pulses. In other examples molecular excitation is dependent on the photon energy (or frequency) of the incident light as well as the pulse arrival time at the ensemble.

The control scheme used in the work presented here is based on the Tanner-Rice scheme [15, 16] where a shaped pulse is used to manipulate quantum mechanical wave packets within a molecular ensemble. This approach is an application of optimal control theory, where an optimal controlled pulse is used to sculpt a desired final quantum mechanical state as depicted in Figure 1.2.

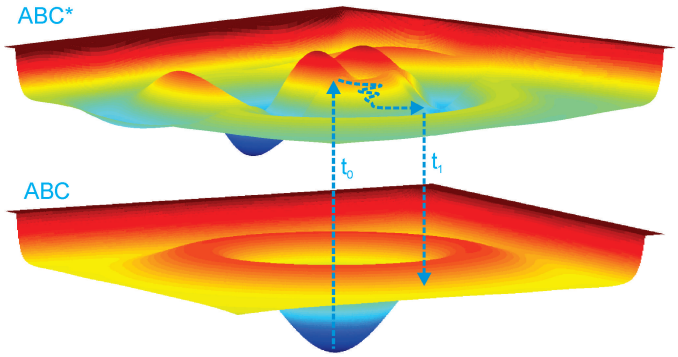

Figure 1.2: Graphical depiction of Tannor & Rice scheme leading to coherent control. An optimal controlled pulse excites a molecule which is now allowed to evolve on the potential surfaces. This may be followed by a probe field providing information about the potential surface of the molecule.

Optimal control theory does however have its limitations. One requires knowledge of the control mechanism leading to the desired outcome which can be very difficult to ascertain depending on the complexity of the process under investigation. Furthermore, quantum mechanical calculations leading to control mechanisms can also be very intricate depending on the complexity of the process. More complex reactions require rigorous mathematical manipulation and computational power not presently available. The limited research in the field of potential energy surfaces also leads to insufficient knowledge of the molecules under investigation which in most cases makes it impossible to calculate control mechanisms during a reaction.

Alternatively to calculating the control mechanisms, we can also make use of experiments to extract the control mechanisms of processes. Contrary to calculating the control mechanisms, minimal information is required when extracting the control mechanisms experimentally. Experimentally extracting the control mechanism is achieved by exposing the reactants to different pulses while observing the reactant's response to the fields. Different pulse shapes will initiate different control mechanisms depending on which quantum mechanical conditions are satisfied. However, due to the vast number of pulse shapes and possible reactions which can occur it is physically impossible to test the reactants response for each pulse shape. Alternatively one can combine the concepts of coherent control and learning algorithms, thus iteratively progressing

towards better solutions.

For the first time in 1992 Judson and Rabitz suggested "closed-loop" control as a useful tool for control of light-matter interactions [35]. This type of control relies on shaping pulse structures according to physical data collected from the ensemble which establishes whether that particular pulse shape optimizes the desired process. Since its first introduction closed loop feedback control has been used in several different laser applications. It has been used to improve the output of processes like high harmonic generation by improving pulse compression [36], it lead to user define pulses created with high fidelity [37, 38, 39], it allowed laser induced polarization and rotational alignment [40, 41] and clearly also lead to coherent control of certain quantum mechanical phenomena [42, 43, 44, 5], to name a few. The scheme on how this process works is illustrated in Figure 1.3.

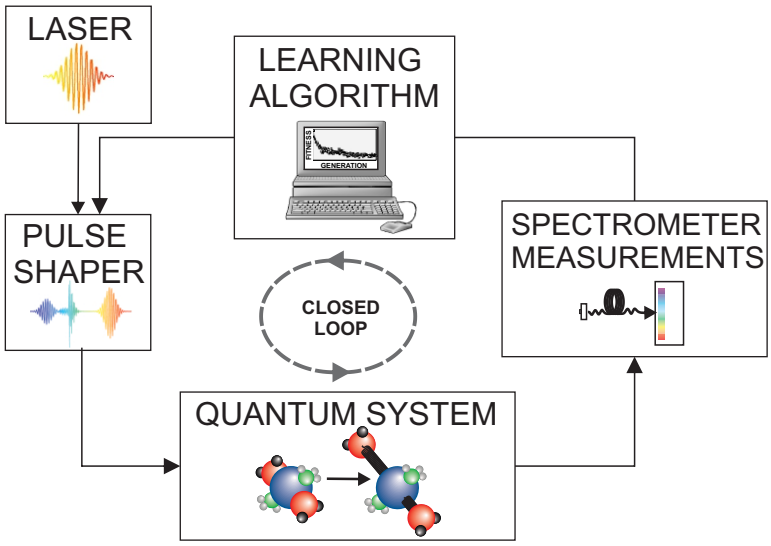

Figure 1.3: Scheme of closed-loop learning control where a pulse shape is determined using empirical data highlighting which pulse shapes lead to good solutions for a particular problem.

During the closed loop control algorithm light interacts with matter such that a molecular ensemble is modified in different ways by different shaped laser pulses. After modifying a molecular ensemble a measurement is made on the ensemble which quantifies the molecular response to the field. The way in which the molecules responded to the different pulse shapes are compared to each other and the pulse structures which increases the desired response are modified to create new pulse shapes. The molecular response is once again measured for these new fields and compared to each other. Typically the software learns what pulse structures are desired. This cycle is repeated until the learning algorithm converges or no improvement is obtained. For these measurements no information about the molecular potential energy curve or the reaction mechanism is required a priori. The only requirement is that the empirical data should yield a measure of the desired response. It should be mentioned that closed loop control is

not opposing the effort of understanding mechanisms of reactions. It is rather a complementary process which through post processing of the pulses constructed can be used to provide insight into the reaction mechanisms.

1.4 Coherent Anti-Stokes Raman Scattering (CARS)

In this work we specifically focus on vibrational excitation. Vibrationally exciting molecules typically rely on a pump process exciting particles to either a single mode of vibration or that of several modes which if coherently excited is non-stationary (also known as a wave packet). The excited molecules are now allowed to evolve over time followed by a de-excitation process which typically probe the particles at different time intervals providing information about their excited modes. Efficient excitation requires that the molecular ensemble interacts with a coherent external control field where the temporal pulse width of the control field is close to the vibrational period of the molecular ensemble. To efficiently control wave interference of molecules, the use of coherent, ultrafast pulses of light is required. Typically atoms in molecules with negligible thermal population vibrate with characteristic periods of generally 50 fs and lower. To drive a vibrational excitation coherently a broadband optical source within the IR region which corresponds to a controlled sub-50 fs pulse duration is required. A well known technique used to overcome this problem is stimulated Raman scattering (SRS). Rather than making use of a single excitation pulse SRS makes use of a temporally overlapped pump and Stokes field to vibrationally excite molecules with a temporal difference between the overlapping light sources less than 50 fs. The energy sources are chosen such that the energy difference between the pump and Stokes pulses matches the energy required to excite molecules to specific vibrational modes. However, the vibrational modes excited should still be verified. A probe pulse now interacts with the molecules and emits an anti-Stokes signal which is a signature of the occupied modes. The complete process using a pump, Stokes and probe field as shown in Figure 1.4 is known as coherent anti-Stokes Raman scattering (CARS).

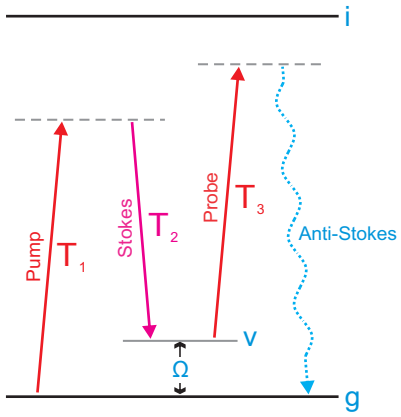

Figure 1.4: The energy diagram for SRS and CARS are shown. Here you can see the ground electronic state,g, the first electronic excited state,i, and the vibrational excited modes,v, used during the processes of SRS and CARS. The dotted lines indicate these processes are detuned from the first excited electronic state.

The CARS energy signature is similar to that obtained using Raman scattering, but with the difference that Raman scatters light close to the pump frequency while CARS signals are blue detuned separating the signal from the driving source. These excitations will only take place if the addressed modes are Raman active compared to the normal infrared active modes.

Since the CARS process was first observed in 1965 it has become a highly valued spectroscopic tool enabling one to observe excited levels without destroying the sample. This was clearly illustrated by the work done by M. Motzkus controlling the vibrational modes of polymers [45] Not only does CARS populate higher order modes, but does so coherently and allow one to probe the modes populated. Knowing the molecules are excited to a particular mode one can allow collision with other molecules while observing the outcome of possible chemical reactions. From these it is possible to infer correlation between excited vibrational levels and the reactions that took place. This however falls outside the scope of the work presented here.

1.5 Outline of this Dissertation

Good understanding of ultrashort pulses are required before shaping can be implemented effectively. In chapter 2 we discuss the general theory related to femtosecond pulses and pulse shaping techniques, as well as show how to measure and characterize ultrashort pulses. The different shaping apparati used are discussed and how shaping was achieved. The techniques used to spectrally and temporally characterize the fields using frequency resolved optical gating (FROG) traces is also explained.

In chapter 3 the learning algorithms used within this dissertation is discussed as well as how we mathematically represent laser pulses to be used within the learning algorithms. Standard one dimensional operators are used when making use of the Fourier basis to create new pulse structures. A 2-d lattice representing information in a joint time-frequency domain called the

von Neumann basis is introduced to address the laser pulses in a more natural way [46, 47]. Furthermore, 2-d operators are developed to accommodate the special features of the von Neumann basis. The solutions obtained by the different bases are compared as well as taking into consideration how fast the bases traversed the solution landscape towards optimal solutions. These considerations were used to decide which bases to use in the subsequent chapters.

The aim of the work presented here is to create tools achieving selective mode population which in the future can be beneficial for chemical reactions. In chapter 4 the theory is developed for the process of Coherent Anti-Stokes Raman Scattering (CARS) considering two vibrational modes of CO_2. Theory for time-resolved CARS is also derived explaining the distinctive beating between modes [48].

Chapter 5 shows the experimental results obtained for the process of CARS compared to the simulations from chapter 4. The learning algorithm from chapter 3 is also used to extract pulse shapes which leads to mode selectivity both in theory and experiment. An enhanced mode beating as well as coherent control is also shown.

Finally in chapter 6 the thesis is concluded with a summary and possible future experiments.

Chapter 2

Ultrafast Optical Pulse Shaping

2.1 Overview

To control a process we need to know what its control mechanism is, as well as how to induce and manipulate it. In the case of laser induced processes: what pulse shape will facilitate transition from an initial molecular state to a desired final state? Some key points need to be addressed to understand this process such as: what laser sources are at our disposal, how will beam shaping occur and how will we characterize the pulses generated, just to name a few. In this chapter the basics of ultrafast laser sources will be discussed [49]. Pulse shaping apparatus and techniques will be shown as well as how we characterize the lasers before and after shaping. Control mechanisms will, however, be discussed in Chapter 4.

2.2 Ultrafast Lasers

Conventional continuous wave (CW) laser sources are not only coherent, but also monochromatic. However, in femtosecond oscillators, several electromagnetic fields consisting of a range of frequencies, oscillate within the cavity at the same time. When these frequencies oscillate in phase (also known as mode-locking) interference occurs leading to localized laser pulses. Typically these pulses have time durations proportional to the inverse of the range of frequencies it consist of. Furthermore, for a Gaussian envelope the temporal and spectral bandwidths are governed by the uncertainty principle,

$$\triangle t_{FWHM} \triangle v_{FWHM} \geq 0.441. \tag{2.1}$$

This can also be expressed in angular frequency which is related by $\omega = 2\pi v$. However, $\triangle t \triangle v$ will only be equal to 0.441 in the case of a Fourier-transform-limited pulse. An ultrafast laser produces electromagnetic pulses whose time duration is of the order of femtoseconds. Such short pulse durations typically consists of high peak powers of up to several terawatts. A description

of the electric field is typically given in either time, $E(t)$, or frequency, $E(\omega)$, by specifying the amplitude and phase of the different temporal or frequency components. However, the pulse shapers used in this work, require information in the spectral domain which is why we designed the learning algorithm to work in the spectral rather than the temporal domain. We can describe an electric field pulse with a Gaussian amplitude profile in the spectral domain as follows:

$$\tilde{E}(\omega) = \underbrace{\exp\left[\frac{-(\omega-\omega_0)^2}{4\Gamma}\right]}_{A(\omega)} \exp\left(i\phi(\omega)\right). \tag{2.2}$$

We will denote the spectral amplitude as $A(\omega)$ and phase as $\phi(\omega)$ while the width of the frequency spectrum is set by Γ. In this notation ω is defined for all positive real values. The spectral and temporal domains are Fourier transform pairs and can be interchanged using,

$$\tilde{E}(t) = \frac{1}{2\pi}\int_{-\infty}^{\infty} \tilde{E}(\omega)\, \mathrm{e}^{i\omega t} d\omega, \qquad \tilde{E}(\omega) = \int_{-\infty}^{\infty} \tilde{E}(t)\, \mathrm{e}^{-i\omega t} dt. \tag{2.3}$$

The Fourier transform from the frequency domain to the temporal domain is, however, done over the complete real space to ensure the required symmetry. Laser fields typically exhibit Gaussian transverse spatial intensity profiles which implies a higher intensity in the field center than on the field side skirts. This is not included within equation 2.2 for the simple reason that it drastically complicates matters. For the work presented here we consider the transverse intensity profile of the field uniformly and therefore the averaged spectral intensity of a pulse relates to the electric field as

$$I(t) = \frac{\epsilon_0 c}{4\pi}\left|E^2(t)\right|. \tag{2.4}$$

The ultrafast laser source used in this work consist of several components as shown in Figure 2.1.

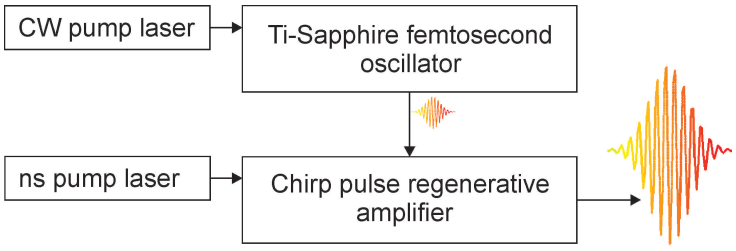

Figure 2.1: Block diagram of the femtosecond laser system used in this work. Femtosecond pulses at 795 nm, with power around 500 mW, are generated in a Ti-sapphire oscillator which is pumped by a Nd:Yag CW laser in the regenerative amplifier. The pulses from the oscillator are stretched, amplified in a Ti-sapphire crystal and re-compressed to a central wavelength of 797 nm with a pulse energy close to 1 mJ and time duration close to 108 fs.

A CW source (Verdi Coherent at 532 nm) pumps a Ti-sapphire (Mira Coherent, titanium-doped sapphire, $Ti^{3+} : Al_2O_3$) oscillator to generate 15 nm bandwidth non-transform limited pulses at a center wavelength of 795 nm and a time duration approximately 110-120 fs with an average power of approximately 500 mW. At this stage the power output is too low to effectively generate four wave mixing and consequently electric fields at different wavelengths. The fs pulses are thus amplified in a chirped pulse regenerative amplifier (Coherent Legend) pumped by a nanosecond pump laser (Coherent Evolution, solid-state Q-switched Nd:YLF laser). This reduces the repetition rate from 80 MHz to 1 kHz while increasing the pulse energy to 1 mJ. The amplifier gain is not the same for all wavelengths. Passing multiple times through the gain medium lead to spectral narrowing where the spectral bandwidth decreased to roughly 13 nm. Close to saturation the red edge of the pulse spectrum is amplified first leading to energy quenching red-shifting the central wavelength to 797 nm [50]. The pulse duration after compression was measured as 108 fs.

2.3 Wavelength Conversion

Two main attributes of light play a significant role in light-induced processes: the energy each photon possesses (not considering multi-photon processes) and the time when it interacts with the material. The wavelength (or energy) emitted by a light source can be changed through the means of non-linear processes where light is coupled non-linearly to the electrons within bulk material which then radiates light at different wavelengths. For this a commercial collinear optical parametric amplifier (OPA) (Coherent, TOPAS-C) capable of generating light from 200 nm to 2000 nm is used. The TOPAS-C consists of two amplification stages allowing conversion from the input field wavelength to the desired wavelength. The pump field is split into 3 fractions. The smallest fraction of pump energy is used to generate a stable white-light continuum within a Ti-sapphire plate. The white light continuum is now allowed to interact non-linearly with the second pump fraction in a BBO crystal which forms part of the first amplification stage. The white light components do not temporally overlap but are temporally separated due to different velocities within the material. Temporal overlap as well as phase matching allows selectivity of the pulse wavelength generated after the first stage.

The pulse generated within the first stage is now used as a seed beam in a second amplification stage ensuring higher output powers. Frequency down-conversion can now be used to cover the lower wavelengths. In the study presented here we typically used a TOPAS-C pumped with light pulses centered at 797 nm to generate light centered around 890 nm. Several other wavelengths will also be generated during the generation of 890 nm which is easily disposed of by making use of wavelength selective filters.

2.4 Apparatus used for Pulse Shaping

Ultrashort pulse shaping entails altering the arrival time and intensities of different frequency components of a laser pulse. To change the temporal attribute of the different frequencies, shapers typically make use of bi-axial nonlinear materials where one axis is defined as a slow propagating axis and the other a fast propagating axis (also referred to as retarders). The intensity of the frequency components on the other hand can be modified using polarization and polarization separation methods to discard any unwanted light exhibiting a particular polarization. Polarization therefore plays a key role in shaped pulse polarization filtering. Pulse amplitude and phase shaping can mathematically be expressed as an ordinary phase mask applied to an arbitrary input pulse. The output pulse in time after the shaper can be seen as a convolution between the input pulse and the mask,

$$\tilde{E}_{out}(t) = R(t) \otimes \tilde{E}_{in}(t), \tag{2.5}$$

or in frequency as a multiplication between the mask and the input pulse,

$$\tilde{E}_{out}(\omega) = T(\omega)\,\tilde{E}_{in}(\omega). \tag{2.6}$$

Several apparatus have the capability of altering pulse shapes. The devices used in this work are an acoustic-optic programmable dispersive filter (AOPDF) placed directly in the beam line and a spatial light modulator (SLM) within a dispersion free$4f$ optical configuration which will be discussed in the sections which will follow.

2.4.1 Using an AOPDF

An AOPDF from *Fastlite* called the *Dazzler* was used before the amplifier, mainly due to it's low diffraction efficiency and low damage threshold, to shape pulses which will be amplified. One should note that the pulse before and after the amplifier will not exactly match due to pump seed phase mismatch and intensity dependence of the amplification process. An in-depth discussion of these attributes can be found in [51, 52, 53]. Therefore, there might be a substantial difference between shaping before and after the amplifier.

In the *Dazzler* frequency mixing is performed between the input pulse $E(\omega)$ and a controlled pulse $f(\omega)$, where the controlled pulse is that of an acoustic wave. The acoustic wave creates a longitudinal transient grating in the propagation direction of the input pulse. If phase matching conditions are met between the acoustic wave and input pulse the ordinary polarised light incident on the crystal will undergo a polarization change to extra-ordinary polarization. The acoustic frequency changes at different crystal positions allowing different frequencies (those satisfying phase matching) to change polarization and henceforth change from a fast propagating axis (ordinary) to a slower propagating axis (extra-ordinary). Due to group velocity differences

between the two axes different arrival times are expected at the output of the crystal. A pictorial representation of this can be seen in Figure 2.2.

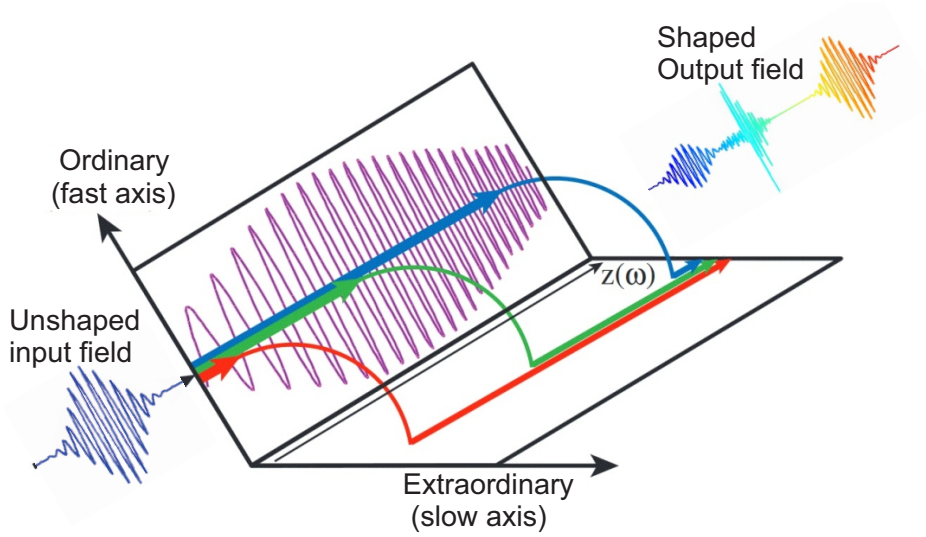

Figure 2.2: Schematic of the Dazzler obtained from [1]. An ordinary-polarized broadband light source enters the Dazzler where upon different spectral components are transferred at different locations within the media to the extra-ordinary axis. The coupled out light within the slow axis is spatially shifted and considered as the shaped field while the ordinary-polarized light is discarded. In the figure it is shown that the red specral component is transferred first, followed by the green and then lastly the blue. As the extra-ordinary axis is the slow axis it implies that the blue spectrum will emergy first from the Dazzler while the red spectrum will be last.

The ordinary polarised light is emitted at an angle of 3.6° which is discarded while the shaped extra-ordinary light is diffracted at 1°with regards to the initial input pulse. Interference between the sound and light waves are dependent on the intensity of the applied acoustic wave. If one considers the incident light field to be monochromatic then the output intensity is:

$$I_{out}(\omega) = \frac{P}{P_0}\frac{\pi^2}{4} sinc^2\left[\frac{\pi}{2}\sqrt{\frac{P}{P_0}+\triangle\Phi^2}\right] I_{in}(\omega), \tag{2.7}$$

where $I_{in}(\omega)$ is the input optical power density, P is the acoustical power density, $\triangle\Phi$ is an asynchronism factor dependent on crystal length and phase matching mismatch and in our case P_0 is an acoustic power given by $P_0 = 4.5\text{x}10^{-6}(\lambda/L)^2$. L is the crystal length and λ the optical wavelength in vacuum. The output to the first diffraction order requires $\frac{P}{P_0}+\triangle\Phi^2 = 4$ while the amplitude coupled to this order is determined by the acoustical power density which change over the crystal length. The Dazzler used in this work consists of a 45 mm long crystal with an acoustic power of $P_0 = 2.17\ m\text{W}/m\text{m}^2$ for a central wavelength of 800 nm. The spectral resolution (or smallest wavelength interval for which the Dazzler can introduce a phase shift) of the AOPDF is given by

$$\delta\lambda_{1/2} = \frac{\triangle\Phi\lambda^2}{\delta nLcos^2\left(\phi_{in}\right)} \tag{2.8}$$

where δn is the difference in index of refraction between ordinary and extra-ordinary axes and ϕ_{in} is the injection angle which is considered 0. A TeO_2 crystal was used in the AOPDF such that $\delta n = 0.04$ and $\triangle\Phi = 0.8$ were considered leading to a resolution of $\delta\lambda_{1/2} = 0.44$ nm. Therefore the time difference between an ordinary and extra-ordinary pulse propagating through the crystal results to a time shaping window of roughly 5.4 ps. Using the spectral resolution and considering the bandwidth, $\triangle\lambda$, of the input optical signal as 30 nm the number of programmable points are determined as

$$N = \frac{\triangle\lambda}{\delta\lambda_{1/2}} = 68. \tag{2.9}$$

The shaping resolution as well as the number of programmable points defines the shaping freedom one has and should be taken into consideration when developing software for pulse shaping. More theory related to the *Dazzler* can be found in [54].

2.4.2 SLM Pulse Shaping in a Dispersion free 4f Configuration

Pulse shaping using a SLM is done by placing a SLM in a $4f$ optical arrangement at the focal plane of the setup such that the bandwidth of the pulse is spatially dispersed transverse to the propagation direction of the light. In this work a folded-reflection geometrical setup was used. From Figure 2.3 one can see the frequency components of the input pulse spatially dispersed using a Bragg-grating (BG_1). The dispersed light is now collimated with lens L_1 and falls incident on the SLM in the Fourier plane of the lens. A flat mirror (M_2) directly behind the SLM directs the light back onto the incoming path but with a slight vertical displacement relative to the injected field to separate the input and modulated fields. L_1 and BG_1 now recombines the spatially separated (according to frequency, ω) fields. Using the folded-reflection geometry resulted in distinctive advantages and disadvantages. Double passing the SLM doubles the maximum phase allowed on the SLM therefore doubling the temporal shaping window, but at the cost of efficiency and/or beam reconstruction fidelity.

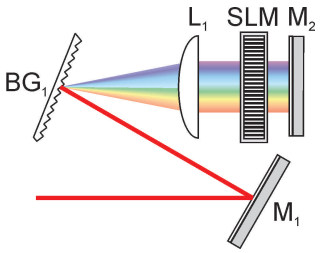

Figure 2.3: Optical 4-f system integrated with a SLM used for pulse shaping. Bragg-grating (BG_1) separates different frequency components spatially which is then collimated by lens L_1. The light passes through the SLM and is reflected by mirror M_2 back onto the incoming path, but slightly vertical displaced to separate the input and modulated fields. Using the L_1 and $BG_1$the spatially separated fields are recombined.

The SLM consists of 2 anisotropic liquid crystal cells placed perpendicular to each other and rotated by an angle of 45° with respect to the incoming light field. Each of these cells are made up of 640 vertical pixels. With the 45° rotation the light field is divided into same parts on ordinary and extraordinary polarization modes of the liquid crystal. Applying an electric field across the pixels will change the pixels orientation resulting in change of its anisotropy. A diagram of the SLM and its liquid crystals are shown in Figure 2.4.

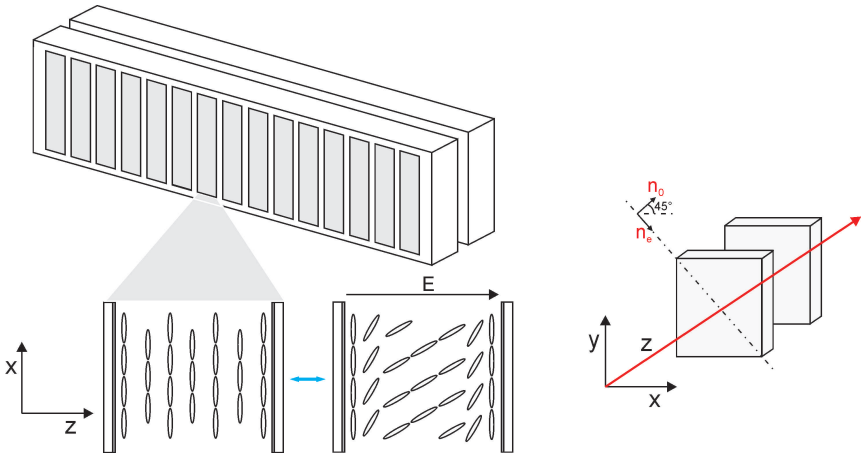

Figure 2.4: (a) The SLM consists of 2 anisotropic crystal cells of 640 vertical pixels each. (b)The first cell is rotated to an angle of 45° and the second cell is rotated to an angle of −45° with respect to the incoming light field. (c) When a voltage is applied over a cell the crystal rotates resulting in a change of its anisotropy.

Typically, shaping is considered as linear filtering. Using the Jones matrix formalism the transmission function of the first crystal rotated to an angle of 45°can be expressed as

$$T_{c_1} = \begin{bmatrix} \cos\left(-\frac{\pi}{4}\right) & \sin\left(-\frac{\pi}{4}\right) \\ \sin\left(-\frac{\pi}{4}\right) & \cos\left(-\frac{\pi}{4}\right) \end{bmatrix} \begin{bmatrix} 1 & 0 \\ 0 & e^{i\triangle\phi_1} \end{bmatrix} \begin{bmatrix} \cos\left(\frac{\pi}{4}\right) & \sin\left(\frac{\pi}{4}\right) \\ \sin\left(\frac{\pi}{4}\right) & \cos\left(\frac{\pi}{4}\right) \end{bmatrix} \tag{2.10}$$

Similarly this can be obtained for the second crystal rotated to $-45°$. As was previously mentioned a folded-reflection geometry is used such that the light double passes the SLM with intermediate reflection by a 90° mirror. It can be shown the effect of all the components together simplifies to a transmission function of

$$\tilde{E}_{out} = \frac{1}{2}\begin{bmatrix} e^{2i\triangle\phi_1} + e^{2i\triangle\phi_2} & -e^{2i\triangle\phi_1} + e^{2i\triangle\phi_2} \\ e^{2i\triangle\phi_1} - e^{2i\triangle\phi_2} & -e^{2i\triangle\phi_1} - e^{2i\triangle\phi_2} \end{bmatrix} \tilde{E}_{in}. \tag{2.11}$$

If we consider the input light to be horizontally polarized and use a horizontal polarizer after the $4f$-setup then the transmission function reduces to

$$T = \frac{1}{2}e^{2i\phi_1} + \frac{1}{2}e^{2i\phi_2}. \tag{2.12}$$

It can easily be shown that the transmission function can be rewritten as

$$T = \underbrace{\cos\left(\triangle\phi_1 - \triangle\phi_2\right)}_{A} \exp\underbrace{\left[i\left(\triangle\phi_1 + \triangle\phi_2\right)\right]}_{\phi}, \tag{2.13}$$

consisting of an amplitude, A, and a phase,ϕ, term. Due to separation of the amplitude and phase it is possible to apply a phase mask with arbitrary amplitude and phase values onto the SLM. For a particular amplitude and phase modulation the phase which should be applied to the various LC's are

$$\triangle\phi_1 = \left[\phi + \arccos\left(A\right)\right], \tag{2.14}$$

and

$$\triangle\phi_2 = \left[\phi - \arccos\left(A\right)\right]. \tag{2.15}$$

The calibration of the SLM and determining the spatial separations of the frequencies fall outside the scope of the work presented here. The resolution and number of addressable pixels for the SLM were measured as 0.4 nm and 40 pixels were used during this work.

2.5 Pulse Measurement and Characterization/Diagnostic Techniques

In the frequency domain, it is fairly simple to measure the pulse spectrum directly with a spectrometer however determining the temporal aspects of these pulses have been found to be challenging. In order to measure a short temporal-event an even shorter time duration is required to measure the event. Temporal resolution of electronic equipment are limited to a few nanoseconds which makes it unfeasible to resolve temporal attributes with regards to femtosecond pulses using electronic equipment directly. Several different techniques exist capable of measuring pulse characteristics; each with its own advantages and disadvantages. In this work intensity auto-correlation and FROG trace measurements were sufficient to characterize the pulse structures. These are indirect techniques where the pulse serves to measure itself and is sometimes referred to as self-referencing measurements.

For intensity auto-correlation the initial pulse is split into two replicas where the one is temporally delayed with respect to the other and spatially overlapped within a nonlinear optical medium. If a BBO crystal is used and the non-linear process considered is second harmonic generation, light will be generated at double the input frequency with a field strength given by:

$$E_{sig}^{SHG} \propto E(t)\, E(t-\tau), \tag{2.16}$$

where τ is the delay between the fields. This can also be represented by its intensity which is equivalent in inferring that the SHG field has an intensity proportional to the product of the intensities of the two input fields. Detectors are however too slow to temporally resolve the SHG intensity directly such that the measurement of the generated signal produce the time integral at different overlap positions between the fields,

$$A = \int_{-\infty}^{\infty} I(t)\, I(t-\tau)\, dt, \tag{2.17}$$

where $A \propto \left(E_{sig}^{SHG}\right)^2$. Expression 2.17 is known as the auto-correlation function supplying information about the field intensity, but nothing about the phase. A feature of this technique is the measurement of a short event in time is transferred to the measurement of a short distance. A typical intensity auto-correlation setup can be seen in Figure 2.5. The pulse is split in two by a 50/50 beamsplitter (BS_1). The two replicas now pass through the two arms of an interferometer, respectively. Replica 1 is reflected by mirror M_1 back onto the incoming path back onto the beamsplitter (BS_1) splitting the pulse a second time to direct 25 % of the initial pulse energy towards lens L_1. Replica 2 gets delayed with respect to replica 1 as the retro-reflector mirrors M_2 and M_3 simultaneously move away from mirror L_1. M_2 and M_3 now steer replica 2 towards lens L_1. The two spatially displaced replicas are focused with lens L_1 inside the BBO crystal such

that the two pulses also spatially overlap. A SHG signal will be generated along the bisector of the pulse replicas if the replicas overlap temporally and if phase-matching conditions are fulfilled. The two replicas as well as the SHG signals generated as a direct consequence of the replicas are blocked with a spatial filter (SP_1). The signal generated by the overlapping replicas is now measured with a photo-detector D_1.

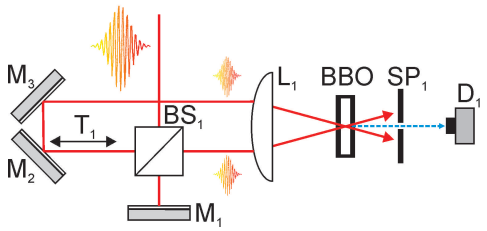

Figure 2.5: (a) Experimental setup for background free auto-correlation and FROG traces. The beam splitter creates two identical pulses. These then overlap spatially and temporally within a BBO crystal. (b) shows the effect of the translation stage on the overlap between the two pulses.

Changing the retro-reflector position will allow for different temporal overlaps between the replicas and consequently provide temporal information about the original pulse. Auto-correlation can however only provide information about the time duration of the pulse, but nothing about the phase of its spectral components. Frequency-resolved optical gating (FROG) allows us to extend the auto-correlation measurements towards a time-frequency domain where a spectrogram is created of the pulse.

This is achieved by measuring the complete SHG frequency spectra with a spectrometer (ocean optics, USB2000), rather than only measuring the intensity with a photo diode, while delaying one pulse replica relative to the other. The mathematical description and procedure to analyse FROG traces was emitted from this dissertation as it falls outside the scope of this work. However, the spectral and temporal representations obtained from FROG traces in this work were extracted using commercial software developed by R. Trebino. A complete description of Tribinos work can be found in [55]. The field trace width in time can be determined from the translation stage velocity v_T and the travelled time, t_T, as $d = v_T t_T$. The time travelled by light in this duration, and therefore the pulse duration, can now be determined as

$$t_{FWHM} = 0.707\left(\frac{t_T v_T}{c}\right). \tag{2.18}$$

Care should however be taken when using SHG-FROG to extract pulse trains. SHG-FROG traces are symmetric such that one cannot distinguish the pulse train order. The pulse order extracted might be incorrect resulting in the first pulse trailing the second. As this is a problem related to the symmetry of SHG-FROG traces and not the pulse structure itself, it should be possible to work backwards and find the correct order of the pulses.

Using a beam splitter and retro-reflector mirrors are not the only way to create and overlap

pulse replicas. Galler et. al. showed it is also possible to make use of pulse shapers to create and even change the temporal overlap between replica fields [56].

2.6 Summary

In summary, this chapter provides a basic introduction to femtosecond lasers, how they can be shaped and how they can be measured. It also provides an overview of the laser sources at our disposal and the shaping apparatus used in this work. This information is sufficient to allow us shaping of the pulses which is the first step towards control. In the chapter which will follow we discusses the procedure which allows us to steer the outcome of a reaction towards a desired outcome.

Chapter 3

Learning Algorithms and Optimal Control Fields

3.1 Introduction

Quantum control is the quest to steer a physical quantum system from some initial state towards a desired final state. The laser field or fields which will lead to this state transition depends on the molecular dynamics involved. It is easy to find a control field for a two level system, but it becomes more complicated to find control fields when working with a multi-level system. With so many control dynamics and possible processes to consider it is a futile attempt to guess the optimal field structure responsible for the outcome of a desired process.

It is sometimes possible to determine the control dynamics for a process if one has sufficient information about the molecules under investigation and if the molecules consist of only a few atoms limiting the number of modes which can be occupied. If it is possible to calculate the optimal field for a particular process the desired molecular dynamical features can now directly be activated through light-matter interactions in what is referred to as "Open-loop" control. Examples of femtosecond pulse shaping and optimal quantum control dynamics can be found in [5, 57, 58, 1] for several different light induced quantum processes.

However, it is not always possible to determine the field structure required to invoke these dynamics. Furthermore, knowing the dynamics responsible for a process does not necessarily provide information about the environment which will influence these dynamics. Also, these calculations require material properties which are not always available. In these cases alternative approaches should be considered.

Learning algorithms or self-optimization algorithms have been widely used since it was first implemented by Arthur Samuel in 1952. These algorithms are not restricted to any specific problem and can be implemented in any scenario where a controlled input leads to a well defined output. In 1992 Judson and Rabitz suggested the first "closed-loop" control experiment for light-matter interactions relying on physical data and a learning algorithm to extract pulses which will lead to the optimization of a desired process. Since then, the successful implementation of

this type of approach has been shown by several well known groups [44].

Theoretically, if a learning algorithm is constructed with no parameter nor time constraints it will always find the optimal solution to a given problem [59, 60]. This is however not feasible during experiments and one requires the solution space to be restricted to a certain amount of parameters while allowing the experiment to be completed within a given time. Furthermore, different learning algorithms traverse the process solution landscape differently such that the learning algorithm convergence time differs for the various algorithms [61]. This chapter is aimed at deciding which learning algorithm will provide feasible results within a given time as well as highlight the problems one will come across when using learning algorithms. In section 3.2 some basic considerations are highlighted for using learning algorithms. This is followed by section 3.3 breaking up the learning algorithm into its subsequent parts. Within this section the relationship between two commonly used representation bases for laser pulse structure, the Fourier and von Neumann bases, are derived. We also discuss the operators operating on the different bases to create new pulse structures. In section 3.4 we will show numerical simulations to optimise the process of SHG as well as experimental results. We investigate the impact of using different bases to represent information within the genetic algorithm. The success of optimizing the SHG signal are compared for the different bases taking into consideration both the convergence time as well as the success of convergence to the desired target. We will show that the genetic algorithm optimises faster when using the von Neumann basis in comparison to the Fourier representations of information. We will show that it is necessary to reduce the solution space drastically when using the Fourier representations while it is not necessary when using the von Neumann basis. Reasons will be given to why the von Neumann basis is better suited than the Fourier domain representation for laser fields. Finally this chapter ends with a summary and comparison discussing the findings when comparing the von Neumann and Fourier bases.

3.2 General Considerations using Learning Algorithms

The outcome of a chemical reaction relies on the environment created before or during reactions. The work represented here mainly focuses on state preparation required for chemical reactions. The successful realization of light induced chemical reactions can be summarised into 2 parts:

- The notion of controlling a chemical reaction; does a state exist which closely resembles the reaction coordinate which will lead to a chemical reaction?
- Synthesis; if there exists such a state can we find a control field which will steer an initial state towards this final state?

Of particular interest to us is synthesizing the field, which will place the molecular ensemble into a state which will enhance the reaction output rate in future studies. To be more specific we would like to control the state transition from an initial state to a predefined final state using light. Electronic state preparation accompanied by vibrational excitation has been achieved

numerous times due to the energies involved in electronic excitations overlapping so well with the energies of laser sources available [33]. However, rotational state preparation without electronic excitation require much lower energies not so easily attainable. Therefore, not much thought has gone into vibrational state preparation and how it relates to chemical reactions apart from the experiments conducted on electronic state preparation. The goal of the work presented here is to make use of a learning algorithm to investigate to what extent can we prepare arbitrary states. The learning algorithm is the key component of the software used to extract the fields required for state preparation. For this reason the way the learning algorithm works should be considered in more detail. We did not make use of commercially available learning algorithms, but rather implemented our own learning algorithms to ensure we understood all the steps thoroughly. As will be shown in this chapter; though the learning algorithm requires no information about the system being optimised, the way the learning algorithm optimises and finds solutions relates strongly to the system. Several parts of the learning algorithm contribute to the way it finds new solutions while traversing towards an optimal solution. The following points should be taken into consideration:

- The learning algorithm operates on a set of parameters which the learning algorithm should be able to change at will. This implies one should numerically quantify what should be changed in the system. One should take care to ensure the information not only represents a suitable way of representing information to the learning algorithm, but that the information would also impact directly the effects one would like to observe and alter.

- The learning algorithm makes use of operators to combine or change the numerical values of the parameters in the system. These should be adapted to accommodate the way information is presented in the point above.

- A measurement is taken of the system representing the success of optimising a particular effect. There should be a direct relationship between the effect we would like to see and what we measure.

The sections which will follows firstly define the key points mentioned above in more detail and then address the issues related to them.

3.3 Learning Algorithm Framework

A biological sample consists of several members each described by their DNA. The DNA provides the genetic information of each member of the population which can either carry phenotypic (characteristics of the individual) or genetic (a coded form of the phenotype) information. During evolution members of a population is allowed to change their phenotypic DNA or during reproduction interchange DNA with a fellow member of the current population. If this change helps the member to adapt better to a new environment the change is considered beneficial

towards the survival of the member relative to members not adapting well. Consequently, members with a good survival probability will outlive members with a poor survival probability. This also implies new generations will consist of a population predominantly produced by members which survived the longest as they had more time to reproduce. For every environment there exist a member DNA sequence best suited for that particular environment. Over several generations the DNA of members within a biological sample will naturally evolve towards the DNA sequence best suited for the environment as it will lead to longer member lifespans as well as higher reproduction rates.

A genetic algorithm (GA) is a search algorithm that optimise solutions according to a target function in such a way that it mimics micro evolution. Typically, the basic steps of reproduction, natural selection, and diversity by variation of information are used in such algorithms. To be able to take full advantage of a genetic algorithm it is important to identify the different fractions the algorithm consists of and adapt them to better fit the problem at hand rather than using the standard issued procedures provided in packages on the internet.

Every data point within the DNA of a member should be a physical parameter that can be changed. The type of information (empirical data) contained in the DNA varies according to the type of GA used as well as the type of basis used representing the information. If the parameters responsible for a process is unknown or cannot be addressed directly other parameters should be used which maps onto the parameter space one would like to address. During light-matter interaction the light-matter interaction parameter space cannot be addressed directly. In this case the laser field is responsible for the reactions such that the laser field parameter space maps onto the light-matter interaction parameter space. In this work the DNA considered for light-matter interactions are the amplitude and phase components of the laser field at different frequencies. Each member of the population is assigned a fitness which measures how well the individual has adapted to its environment. For the purpose of controlling a quantum system, the fitness is determined by evaluating some observable of the quantum system while taking into consideration on how the experimental data reflects the control dynamics investigated. A larger fitness value implies the desired dynamics are more directly driven than a small fitness value.

The primary focus of machine learning is to automatically learn to recognize complex patterns and make decisions based on empirical data which will improve the outcome of the process. The difficulty lies in the fact that the set of possible behaviors, given all possible inputs, is too large to be covered by the set of possible observed examples. Hence the learning algorithm uses a subset of solutions to produce new case scenarios which might lead to finding optimal solutions. Members with good fitness are retained in the new population. They are also favoured when deciding which members (also referred to as parents) will participate in the gene pool for the next generation. Using several different techniques, pulses with high fitness can be combined or altered creating new pulses which might retain and hopefully enhance the specific characteristic related to the dynamics. In Figure 3.1 the pseudo code for the genetic algorithm used in this work is shown. The procedure can be broken down into the following steps:

1. Initial conditions and constraints are set for the GA. A population of N members with

randomly selected DNA is constructed as the input.

2. A characteristic measurement is taken for each member and a fitness value is assigned evaluating the success of the member to generate some particular outcome. The measurement could be a spectrum, power measurement or any other defining characteristic of the optimization problem.

3. Natural selection is now used to determine which members show superiority over others whereupon only M members (denoted parents) are selected as part of the gene-pool for creating the next generation (denoted children) of members.

4. The GA now makes use of operators to create new members. Generic operators are used in all GA's which includes cross-over breeding and mutation. The diversity aspect allowing one to explore the parameter space comes from the fact that random parents are chosen to spawn new offspring. Furthermore diversity is promoted using mutation instigating small changes to the children on a random basis introducing new genetic information in children. Several others do exist, but will be explained at some later stage.

5. Step 3 up to 5 are now repeated until a satisfactory solution is obtained for the process under investigation or when an upper limit on the number of generations is reached. i Denotes the current generation and $MaxGen$ the maximum number of generations allowed.

Several learning algorithms are capable of optimising solutions to a problem [62, 63, 64, 65]. This work is only focused on a genetic algorithm approach using different ways of representing the pulse information while comparing the learning algorithm progress over time. Matlab as a program language was used due to its versatility and widely used capabilities in mathematical as well as mechanical frameworks. We only used the builtin matlab learning algorithm in part because it will only limit ones freedom in controlling the way the GA operates. An in-depth description of the matlab's genetic algorithm TOOLBOX can be read to broaden ones understanding on how learning algorithms work in general [66].

3.3.1 Representing Information in Different Bases

Several different mathematical bases exist capable of describing lasers fields. The ones most familiar to us are those of the spectral domain representation or its temporal counterpart as described in section 2.2. As was previously mentioned certain light induced processes depend on both the spectral mode as well as the energy distribution over time of the field inducing the reaction. If the learning algorithm operates on the Fourier space the information is represented in frequency or time only addressing effects within that particular domain. It is therefore difficult to optimise a time related dynamic when operating in the frequency domain and visa versa. It would be ideal to operate in both time and frequency at the same time without having to use Fourier transforms.

As an alternative to the Fourier domain bases one can also consider a combined time-frequency representation like the Husimi or Wigner representations which are continuous in frequency and time [67]. The effect pulse shaping equipment has on a pulse can mathematically

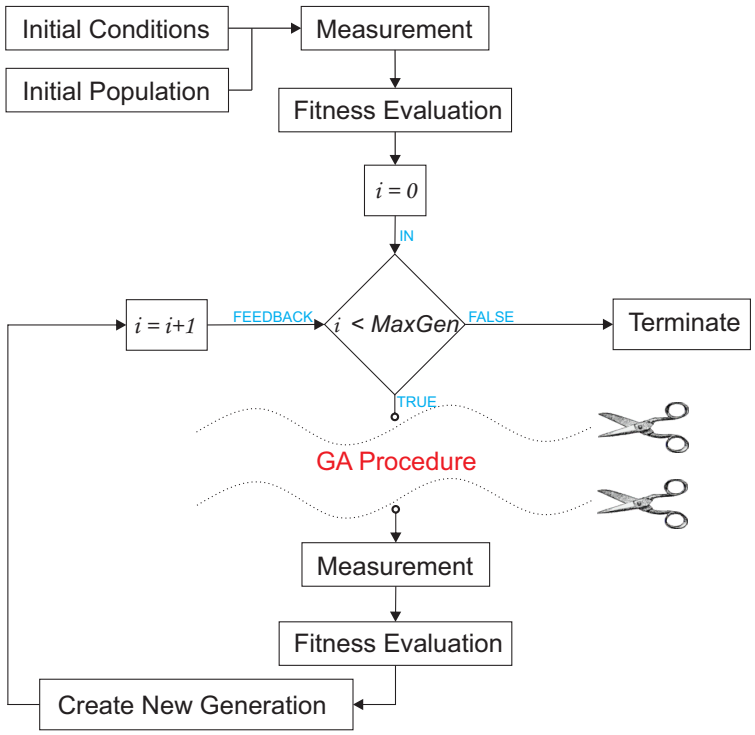

Figure 3.1: A typical pseudo algorithm used to find an electromagnetic wave which will optimise some process. A randomised initial value population is constructed and measured relative to some observable and fitness value assigned. Using a GA new pulses are constructed, effect measured and fitness assigned.

be seen equivalent to a transmission function applied to an input field. These shaping devices are pixelated which operates on the numerical representation of a transmission function, which is discretised and not continuous. Recently the group of Tannor reintroduced a discretised time-frequency basis very similar to the Husimi representation called the von Neumann basis [68, 69]. This basis should be able to address the problem mentioned of searching for a solution in a domain not directly related to the problem at hand. To convert information between the Fourier domains and the von Neumann domain one once again start by representing the field according to its spectra as,

$$\tilde{E}(\omega) = A(\omega) e^{i\phi(\omega)}, \tag{3.1}$$

which consists of a spectral amplitude $A(\omega)$ and spectral phase $\phi(\omega)$ component spanned over a region of frequencies. The spectral and time domains are related to each other via a Fourier transform as follows:

$$\tilde{E}(t) = \frac{1}{2\pi}\int_{-\infty}^{\infty}\tilde{E}(\omega)\,e^{-i\omega t}d\omega. \tag{3.2}$$

Both the temporal and spectral phases are commonly expanded as a function of their derivatives in a Taylor series around the central time t_0 and frequency ω_0, respectively. For frequency we find,

$$\phi(\omega) = \phi_0^0 + \phi'(\omega-\omega_0) + \frac{1}{2}\phi''(\omega-\omega_0)^2 + ... + \frac{1}{n!}\phi^n(\omega-\omega_0)^n. \tag{3.3}$$

where ϕ^n indicate the n^{th} derivative of the phase at ω_0. An in depth description can be found in [49]. This expansion supplies valuable information about the pulse structure.

- ϕ^0 is known as the Carrier Envelope Phase (CEP) which corresponds to the phase between the envelope of the electric field and the carrier.
- ϕ^1 simply corresponds to a time delay between the pulse and an arbitrary origin of time.
- $\phi^2$is the group delay dispersion (GDD), also known as linear chirp. Traversing through any medium will induce GDD due to different frequency components travelling at different velocities within the medium.
- ϕ^3 corresponds to the cubic phase which leads to pre- or post-pulses within the time domain.

This expansion can be of value if the control mechanism is connected to one of these terms and has been used in learning algorithms to a great extent [70]. It is worth knowing that not all phases can be expanded in a Taylor series. For instance phase-jumps as well as any repetitive structure like sinusoidal varying phase cannot be represented by the Taylor series. The group of Radzewicz showed the importance of being able to create phase jumps when considering control mechanisms based on destructive interference [42]. The Taylor expansion approach is therefore not used in this work, but each pixelated element of the pulse shaping device is allowed to be changed independently of its neighboring pixels. This allows phase solutions outside the Taylor expansion, but at the expense of increasing the number of solutions drastically. A larger solution space will take longer to traverse the solution space which on the other hand might defeat the purpose of using a learning algorithm to decrease the time to find an optimal solution. It also increase the risk of ending up in a local minima. One can decrease the solution space by grouping and assigning the same phase value to adjacent pixels. This will however influence the resolution and shaping capabilities of the SLM.

As highlighted in [71] many control mechanism relate to pulse trains rather than a single pulse shaped into a certain structure. This can easily be addressed in the time domain, but

require several GA (operational) steps in the frequency domain. This alone is enough reason to consider an alternative approach of a combined time-frequency representation which provides interpretation of temporal and spectral properties at the same time. A pulse in time or frequency is represented in the von Neumann basis as a combination of a number of discrete two dimensional phase-space lattice elements Q_{ω_n,t_m} which represents non-orthogonal Gaussians.

This bases stems from the Wigner function presenting signals consisting of an infinite continuous spectrum [72]. It was however adapted for signals consisting of a discrete and finite spectrum. Consider the electric field $\tilde{E}(\omega) \equiv |\varepsilon\rangle$, to be well defined within the frequency domain consisting of l equally spaced frequency points. Expanding the signal into a set of N complex valued Gaussians such that $N\text{x}N = l$ will result in N complex valued von Neumann coefficients Q_{ω_n,t_m} utilizing N von Neumann basis elements. The von Neumann basis elements are expressed as [68, 46, 69],

$$\tilde{\alpha}_{\omega_n,t_m}(\omega) = \left(\frac{2\alpha}{\pi}\right)^{1/4} exp\left[-\alpha(\omega-\omega_n)^2 - it_m(\omega-\omega_n)\right], \tag{3.4}$$

which are all centered around the points (ω_n, t_m) for $n = 1...N$ and $m = 1...N$. These points are redistributed equidistant over the complete time (T) and frequency (Ω) range. All these Gaussians have the same full width at half maximum σ_ω, that is related to α by,

$$\sigma_\omega = \sqrt{\frac{4\ln 2}{\alpha}}. \tag{3.5}$$

Similarly can be found for the time domain,

$$\sigma_t = \sqrt{\alpha 16\ln 2}, \tag{3.6}$$

such that the Fourier relation $\sigma_t\sigma_\omega = 8\ln 2$ holds. The identity operator can now be expressed in the new basis as,

$$1 = \sum_{(n,m),(i,j)} |\alpha_{\omega_n,t_m}\rangle S^{-1}_{(n,m)(i,j)} \langle\alpha_{\omega_i,t_j}|, \tag{3.7}$$

such that $S_{(n,m)(i,j)} = \langle\tilde{\alpha}_{\omega_n,t_m}|\tilde{\alpha}_{\omega_i,t_j}\rangle$. S is known as the overlap matrix which also takes into account the non-orthogonality of the von Neumann basis. The electric field $|\varepsilon\rangle$ can now be written as

$$|\varepsilon(f)\rangle = \sum_{n,m} \tilde{Q}_{\omega_n,t_m} |\alpha_{\omega_n,t_m}\rangle, \tag{3.8}$$

connecting the electric field in the spectral domain to the von Neumann domain. The values

of $\tilde{Q}_{\omega_n,t_m}$ are determined by,

$$\begin{aligned} \tilde{Q}_{\omega_n,t_m} &= \sum_{i,j} S^{-1}_{(n,m)(i,j)} \left\langle \tilde{\alpha}_{\omega_i,t_j} \left| \varepsilon \right. \right\rangle \\ &= \sum_{i,j} S^{-1}_{(n,m)(i,j)} \int \tilde{\alpha}^{*}_{\omega_i,t_j}(\omega)\, \tilde{\varepsilon}(\omega)\, d\omega. \end{aligned} \tag{3.9}$$

The coefficients are complex and can therefore be described by amplitude and phase components which relates to the amplitude and phase in the frequency representation [68]. A noticeable difference between the two bases is that the Fourier domain is confined to one dimension (in time or frequency), while the von Neumann basis is a two dimensional lattice space confined in time and frequency. It was recently shown that the transformation between the Fourier and von Neumann representations conserve the total information [68]. Figure 3.2 serves as an example to illustrate how information is represented in the von Neumann basis in comparison to it represented within the Fourier domain. The von Neumann lattice shows frequency attributes on the horizontal axis while temporal attributes can be seen on the vertical axis. In the figure the information represented on the two dimensional von Neumann lattice is equivalent to 3 pulses in frequency (bottom) as well as in time (left).

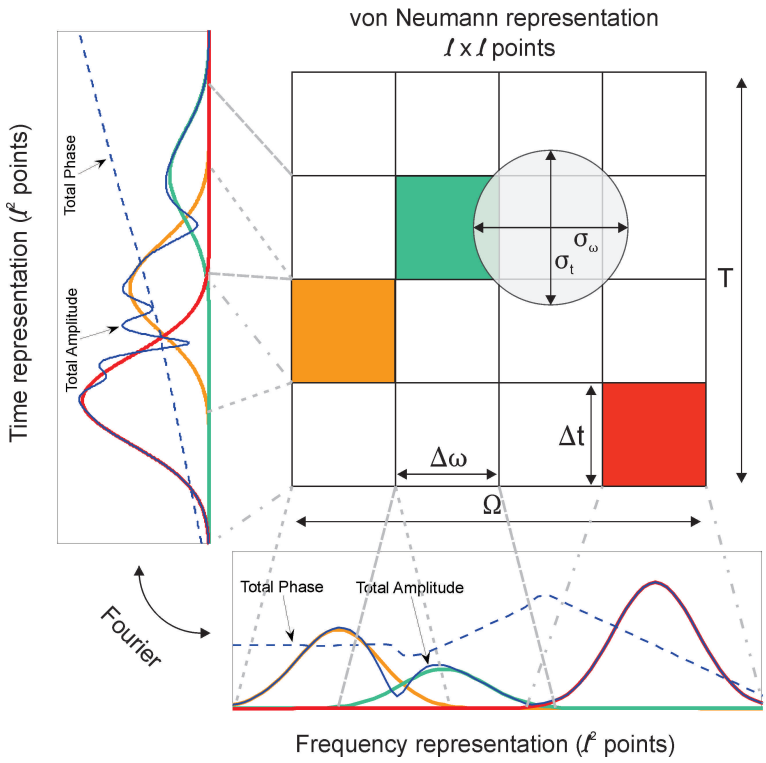

Figure 3.2: A representation of the von Neumann lattice with 3 pixels containing information which represents 3 Gaussian pulses separated in time as well as frequency. (Bottom) The solid blue line shows the resultant amplitude and the dashed blue line the resultant phase within the frequency domain. (Left) The solid blue line shows the resultant amplitude and the dashed blue line the resultant phase within the time domain.

Up until now it was only mentioned that the fields should be discretised for one to use them in the learning algorithm. Nothing has been mentioned about how user defined parameters influence the field resolution nor how they effect the time it takes for the learning algorithm to converge to a solution. Lets consider the case where a phase mask is applied to a Gaussian input pulse to create a double pulse by shifting low wavelengths back in time and high wavelengths forward in time as illustrated in Figure 3.3 (b). Figure 3.3 (c) shows the Fourier domain and (d) the von Neumann representation of the mask which will lead to the output field in Figure 3.3 (b).

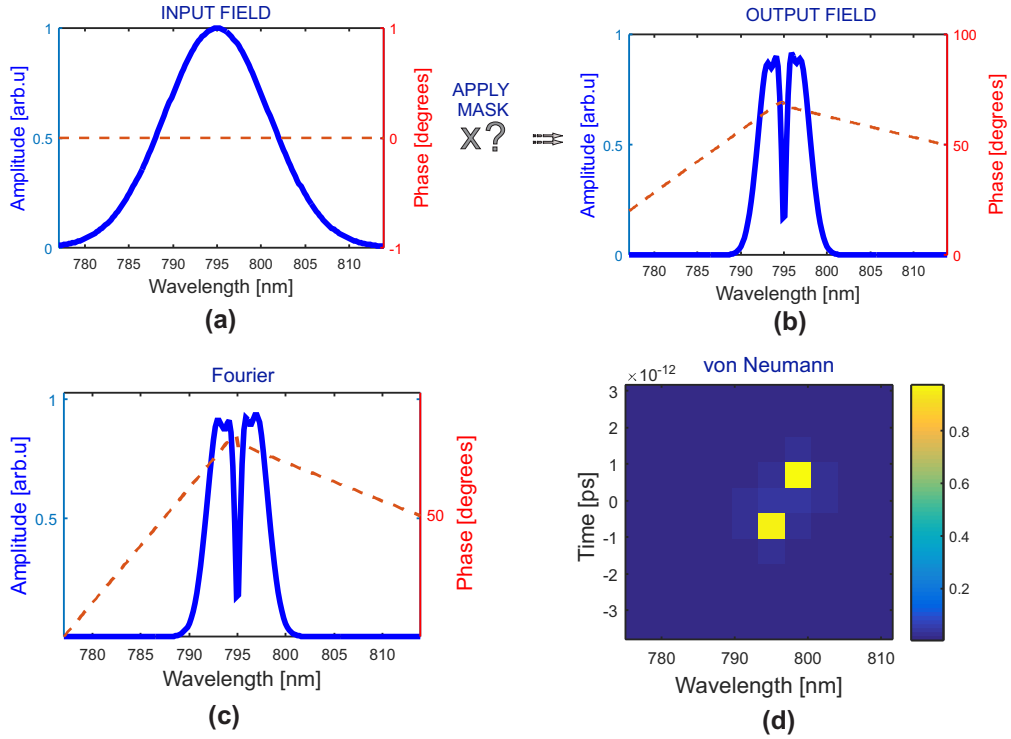

Figure 3.3: (a-b) A Gaussian input field is modified such that low input wavelengths are shifted back in time and high input wavelengths are shifted forward in time. (c) Is the frequency representation of the amplitude and phase mask which leads to the output field in (b). (d) Represents the von Neumann lattice equivalence of the frequency mask shown in (c).

In the Fourier domain representation (Figure 3.3 (c)) several wavelength bins has to be modified to shift the frequency components in time. However, within the von Neumann basis (Figure 3.3 (d)) most of the frequency components are shifted by shifting mainly 2 pixel locations. This example illustrates the ease with which a search in the von Neumann basis might find a solution consisting of multiple pulses by just shifting the information from one lattice point to another. When moved horizontally different frequencies will be addressed while a vertical change will move the Gaussian pulse forward or backward in time. During a shift on the von Neumann lattice several pixels on the SLM are addressed at the same time. However, in the spectral and temporal domain the search algorithm would have to find linear phase slopes which will be a tedious task as the information for a single bin is changed during every generation. Therefore many more iterations are required to change from one pulse train sequence to another in the Fourier domains as compared to the von Neumann basis.

There is always a trade-off between finding a high resolution pulse structure and the time it takes before the learning algorithm converges. It will become clear at a later stage that in most cases good field resolution unfortunately leads to longer convergence time. One should also carefully consider the precision or possible different values the amplitude and phase in each bin can have. Once again low precision limits the number of solutions while high precision increases the convergence time. In both the von Neumann basis as well as the Fourier basis both spectral

and temporal resolutions should be taken into consideration. Similar to the Fourier domains the temporal and spectral resolutions within the von Neumann basis are governed by the uncertainty principle,

$$\delta t \delta \omega = 2\pi \tag{3.10}$$

This implies that good resolution within the time domain, will result in poor resolution within the frequency domain and visa versa. Within the von Neumann domain a spectral resolution of 7 nm will lead to a temporal resolution of 300 fs while a spectral resolution of 1.75 nm will lead to a temporal resolution of 1202 fs for each pixel. One should therefore decide what type of resolution is required within the time and frequency domains beforehand. During section 3.4 where one tests how the different bases compete against each other the effects these parameters have on the learning algorithm searching for an optimal solution will also be investigated.

3.3.2 Learning Algorithm Operators

Different pulse shapes are molded by applying different amplitude and phase masks on the shaping devices. Based on empirical data the learning algorithm makes use of operators to modify previously used masks to improve a desired light-matter reaction outcome. Because information is represented as a one dimensional array of values in the Fourier domains compared to a two dimensional lattice space of values within the von Neumann basis it should be self evident that the same operators aren't used for both bases. All attempts were made to keep the primary idea similar for both bases.

For the learning algorithm the electric field represented in the Fourier domain is divided into N amplitude and N phase bins. The amplitude can be any value between 0 and 1 while the phase can be any value between 0 and 16π. The *Dazzler* used for pulse shaping does however not allow phase jumps between adjacent bins to exceed 4π. This should also be taken into consideration during experiments. Each of these DNA data points are now converted to binary strings of length M which we denote the precision of the value or the possible values allowed. Henceforth, all laser fields are numerically represented as a DNA string of 0 and 1 values of length 2xNxM. For the Fourier domain standard mutation and cross-over operators were used equivalent to what can be found within the matlab genetic algorithm toolbox [66]. Examples of how these operators work can be seen in Figure 3.4 and they are defined as follows:

- **Mutation Operator:** A parent is chosen to be mutated. The mutation operator randomly selects a location within the parent string and changes its bit value creating a new child. If it had a value of 1 it will become 0 and if it had a value of 0 it will become 1.

- **Cross-over Operators:** Two parents are chosen for breeding where the cross-over operator exchange information between two parent strings. Two string locations are randomly selected and the information between these two points are exchanged between parents creating two new children.

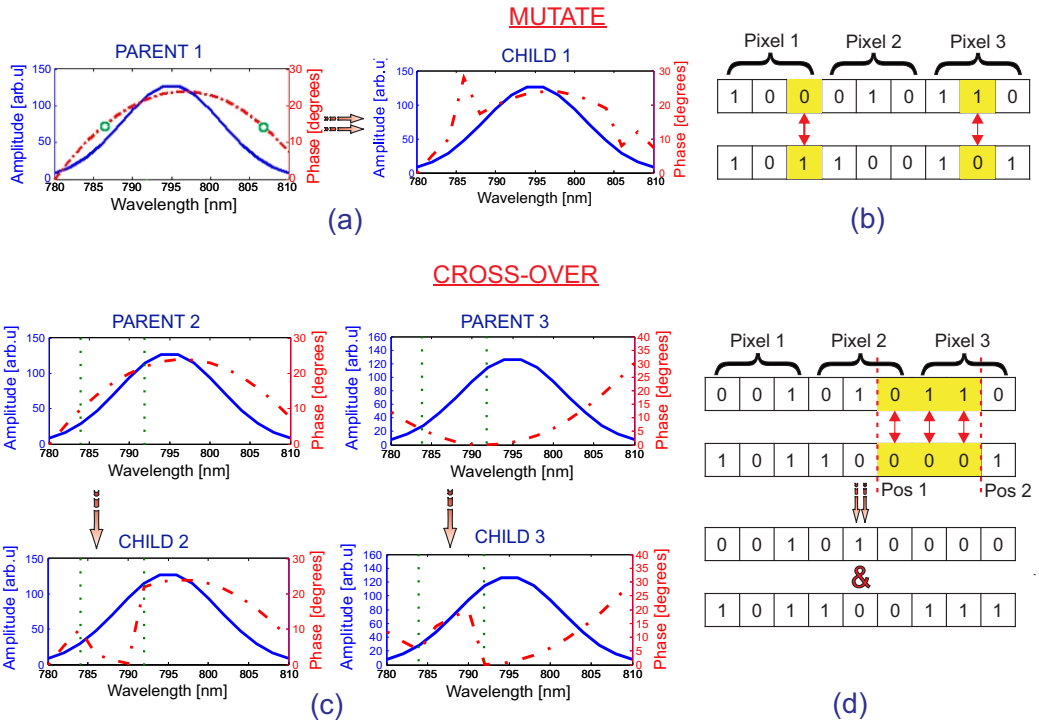

Figure 3.4: Frequency domain operators used within the learning algorithm. (a) Shows the mutation that took place on a parent. The two green dots indicate the location of the phase values mutated. (b) Illustrates the binary representation of a string mutated. Pixel 1 was changed from value 4 to 5 and pixel 3 was changed from value 6 to 4. (c) Shows cross-over between two parents. The area between the green dotted lines show the phase values exchanged between the parents. (d) Illustrate binary information being exchanged between parents. A binary exchange is not equivalent to a real value exchange as shown here. If one considers real values then parent 2 pixel 3 changed from 6 to 0 while parent 3 pixel 3 changed from 1 to 7.

Even though only two operators are used for the Fourier domain the operators can be combined to introduce more complex operations. As specified the fields represented in the frequency domain is converted into a string of binary values when used by the learning algorithm. These should be converted to real values before it can be used as input to the shaping devices.

The von Neumann basis represents information in the form of a two dimensional lattice where the one axis represents frequency and the other time. In general, learning algorithms operate on one dimensional vectors and not two dimensional lattices. This problem can be addressed in two ways. Firstly, it is possible to latch each row of the von Neumann lattice to the next creating a one dimensional vector and then use the operators defined for the Fourier basis. The information is thus presented as a vector where each element represents a wavelet in time and frequency where upon the vectors for the Fourier domains relate to plane waves. However, this approach does not take advantage of how elegantly the von Neumann basis represents information. Moving a pixel's information in the von Neumann basis to their vertical neighboring pixels represents a Gaussian wavelet temporally shifted forward or backward in time. To take full advantage of these aspects a learning algorithm has been developed including its operators which can function

on a two dimensional lattice. Each von Neumann lattice element can have an amplitude value between 0 and 1 while the phase can be any value between -2π and 2π. Examples of the von Neumann operators are shown in Figure 3.5 and they are defined as follows:

- **Mutation Operators:** A parent is chosen for mutation. The mutation operator randomly selects a location on the von Neumann lattice. A random complex value of magnitude between 0 and 1 and phase between -2π and 2π is added or subtracted at this location creating a new child. In the Fourier domain this is equivalent to a Gaussian pulse added or subtracted to the parent.

- **Migrate Operators:** A parent is selected. A random location on the parent von Neumann lattice with a non-zero magnitude is selected. The information on this location is now moved to any randomly selected adjacent lattice points. This can lead to several things happening in the Fourier domain. If it was moved horizontally the Gaussian pulse changed its central wavelength. If it was moved vertically the Gaussian pulse moved forward or backward in time.

- **Expand Operators:** A parent is selected. A random location on the von Neumann lattice is selected where the information on this location exhibit at least 50 % of the total energy of the complete pulse structure. Randomly selected adjacent lattice elements are increased or decreased relative to each other.

- **Cross-over Operators:** Two parents are chosen to exchange information. A small grid consisting of 1x1 up to 3x3 pixels is randomly selected on the von Neumann lattice. The information on this selected grid for the parents are now interchanged creating two new children.

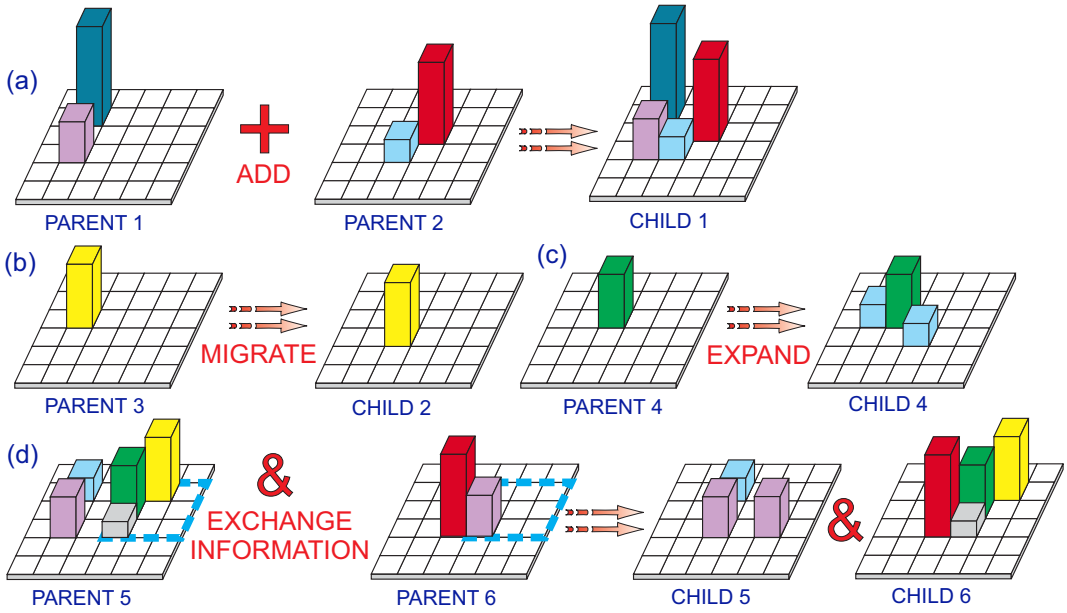

Figure 3.5: von Neumann domain operators used within the learning algorithm. (a) Shows the mutation that took place on a parent. Two Gaussian wavelets are added to a parent pulse. (b) Migration takes place where information is shifted from one lattice point to another. This can lead to a Gaussian pulse shifting its central wavelength or it can a temporal shift forward or backward in time. (c) A lattice location is selected and information is added all around this point. (d) Two parent fields exchange information.

Similar to that of the Fourier domain the von Neumann lattice representation is only used within the learning algorithm to create new children. The information should be converted to real values within the spectral domain when used as input to the shaping devices. When using the von Neumann operators care was taken to ensure the amplitude within the spectral domain is between 0 and 1 while the phase is between 0 and 16π using a suitable normalization.

In figure 3.1 the section denoted GA Procedure were omitted from the graph. This is because different operators were used and therefore different procedures followed when using the Fourier domain vs. the von Neumann domain. It would be ideal to compare the different bases on equal ground. A learning algorithm which operates on a one dimensional vector space is completely different from one operating on a two dimensional lattice thus making them incomparable on a completely equal footing. Additionally, the Fourier domain has fewer operators than the von Neumann domain. Deciding which basis to use still requires some form of comparison. Several different solution space parameters were selected for both bases and the output compared to investigate how a learning algorithm traverse the solution landscape when operating on the various bases. The schematic outline of the learning algorithm procedures used in this work for the various bases can be seen in Figure 3.6 and 3.7 for the Fourier and von Neumann bases, respectively. Several possible cross-over and mutation combinations could be used. The ones showed are the ones found which produced the best results for the given target function. For each generation the 10 members with the highest fitness are retained and also used as parents to

create the next generation consisting of 60 members in total. For the Fourier basis the parents are used to create 50 children; 20 using cross-over and 30 using mutation. In every generation cross-over operators are used to ensure some form of information is retained from generation to generation. For mutation there is distinction between strong, medium and weak mutation. Over 4 generational intervals the level of mutation decreases with an increase in the generations. For the first few generations members of the population will be far from optimal solutions. Strong mutation or rather a few mutations at the same time will aid the learning algorithm in drastically changing the population. At later generations when the learning algorithm is close to an optimal solution only small changes should be made to the members. The learning algorithm is allowed 160 generations to find the optimal solution before termination is initiated. Each member consists of $2N$ number of parameters which can be changed. Higher parameter numbers result in better resolution, but at the cost of increasing the parameter space and in the process increasing the time required for the learning algorithm to converge.

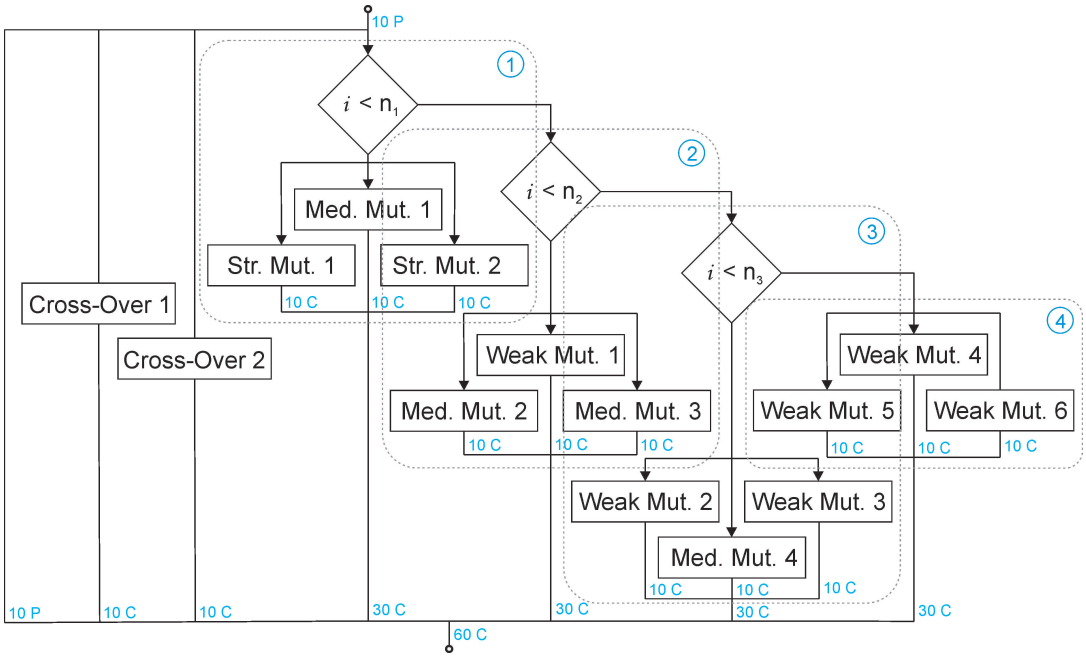

Figure 3.6: GA outline for Fourier space.

For the von Neumann basis the parents were used to create 10 children from mutation, 10 from cross-over and 10 from expand operators for each generation. The other 20 children where created using a combination of different operators which changed as the number of generations increased. In the final few generations the solution should be close to optimal. At this stage the share-stress operator applies 2d smoothing over the lattice grid connecting any pixels in close proximity. The share-stress operator averages over neighboring pixels connecting neighboring Gaussian wavelets.

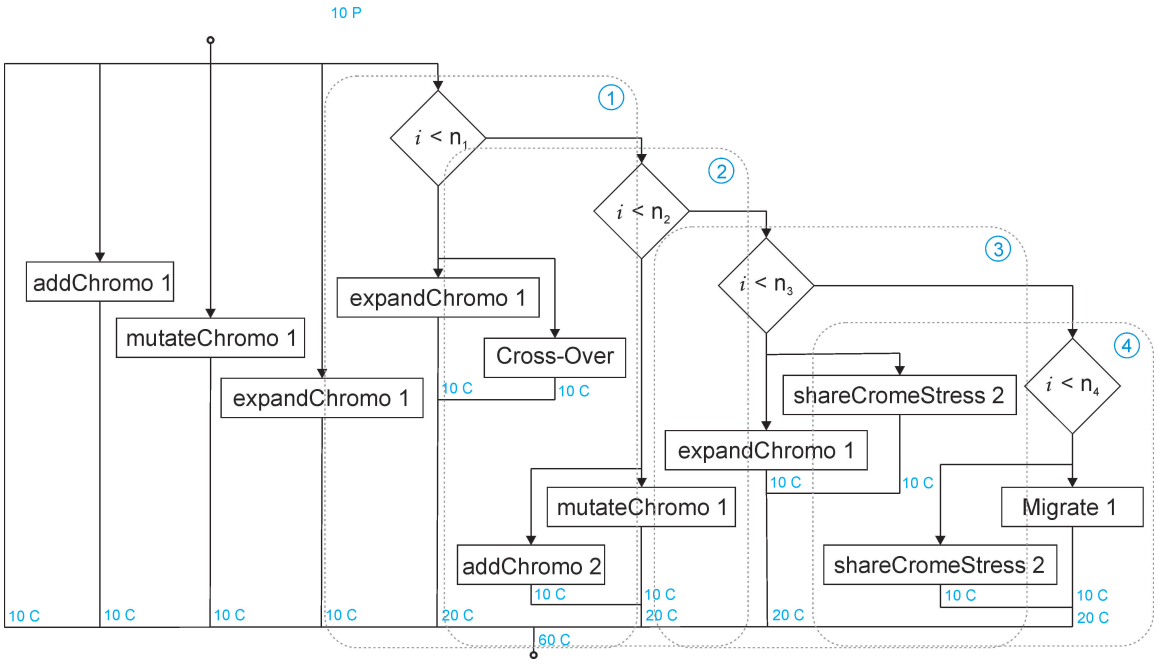

Figure 3.7: GA outline for von Neumann space.

The learning algorithm, it's operators, as well as the bases they operate on have now been defined. The learning algorithm however functions on empirical data reflecting the success of the created pulse to achieve some objective. Measurements seldom directly reflect a particular desired outcome and require some processing where one can assign a fitness value to the data related to a target function.

3.4 von Neumann vs. Fourier Domain Optimization

3.4.1 Problem Statement

Having developed a learning algorithm poses the question whether the learning algorithm will find the best possible solution or will it end up in some local minimum of the optimization space. One would also like to compare how numerical simulations and the physical experiment compare to each other when maximizing the value of a target function. In order to verify that the learning algorithm finds the best solution one has to test how it operates on a well known problem. Furthermore, one would like to know how the von Neumann basis compares against the spectral basis within a learning algorithm.

It is known that SHG within a BBO crystal is non-linearly dependent on the input pulse field strength [49]. Therefore, for a fixed pulse energy it is reasonable to expect that compressed pulses will lead to a stronger second harmonic output. To test the learning algorithm a temporally stretched input field is considered and the learning algorithm is required to find a mask which will compress the field. This will allow one to characterize the learning algorithm qualitatively. The SHG signal intensity within a non-linear crystal (in this case a BBO crystal) is expressed

by [49],

$$I(2\omega, L) = \frac{2^7 \pi^3 \omega^2 \chi_{eff}^2 L^2 I^2(\omega)}{n_{2\omega} n_\omega^2 c^3} \left[sinc(\triangle k L/2)\right]^2 . \tag{3.11}$$

Here $I(\omega)$ is the intensity of the incident field at frequency ω, χ_{eff} is the effective nonlinear susceptibility of the process, $n_{\omega/2\omega}$ is the index of refraction for the pump or the generated signal, ϵ_0 is the permitivity, c is the speed of light, L is the crystal length while $\triangle k$ is the phase matching mismatch. If the phase matching mismatch approaches 0, the sinc function disappears and the SHG signal becomes directly proportional to the square of the pump field intensity.

However, not only solutions where the learning algorithm corrects the spectral phase components of the input field are considered, but also how the amplitude of the spectral components play a role. In literature, amplitude shaping is often considered to exhibit contributions with reduced importance towards the solutions compared to the contributions made by phase shaping [73]. Therefore amplitude shaping is often at times discarded. Contrary to this assumption a more general approach was adopted, whereby the amplitude shaping in the learning algorithm was included.

Consider the input field numerically as a temporally stretched field created when a linear chirp of 25000 fs^{-2} is applied to a transform limited (TL) field. This chirp stretched the pulse from 120 fs to roughly 1.1 ps. The spectral domain representation of the numerically represented input field can be seen in Figure 3.8(a) while (b) shows the temporal domain representation.

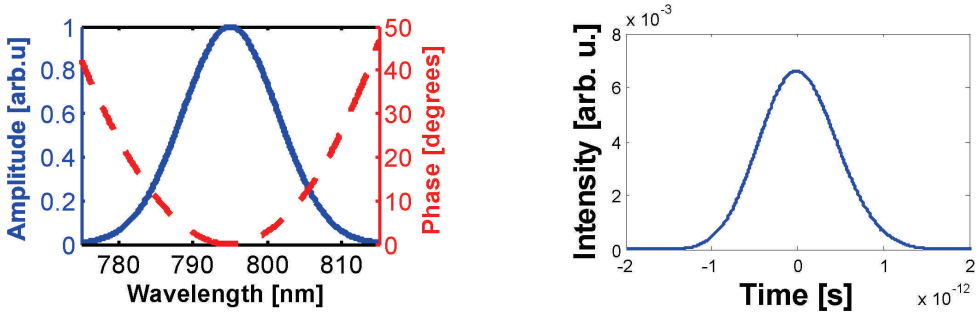

(a) (b)

Figure 3.8: Fourier domain representation of the input field used during simulations. (a) The blue solid line represents the amplitude while the red dashed line represents the phase of the input field in the spectral domain. (b) The time domain representation of the pulse shown in (a) obtained using the Fourier transform on (a). The field was stretched from 120 fs to roughly 1.1 ps.

If only phase shaping is allowed then a TL-pulse will result in the shortest time duration and highest SHG peak intensity. The transmission function applied to the input pulse should therefore counter the phase of the input field leading to a flat phase while keeping the amplitude fixed. The mask for optimal phase only optimization can be seen in Figure 3.9(a) which will lead to the output field shown in Figure 3.9(b). (b left) Shows the resultant spectral domain

representation of the output field, while (b right) shows the time domain representation of the output field exhibiting a time duration of 120 fs and relative peak intensity of roughly 0.02.

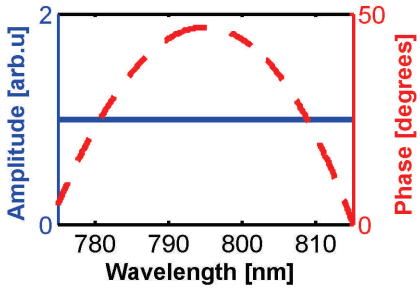

(a)

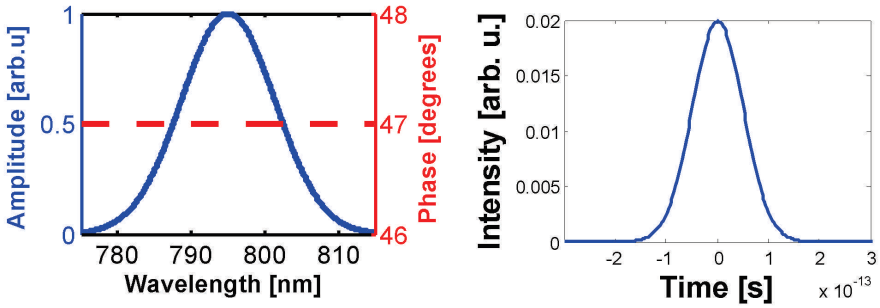

(b)

Figure 3.9: The anticipated transmission function which will compress the stretched input field when phase only shaping leading to a TL-pulse is taken into consideration. (a) Spectral domain representation of the transmission function which will lead to optimal compression of the input field and consequently a TL-pulse. The blue line is constant at 1 indicating no amplitude shaping took place while the red dashed line is the phase which cancels the chirp of the input field. The amplitude was chosen to keep the energy normalised to 1 mW. Field output when the transmission function shown in (a) is applied to the input field shown in Figure 3.8. (Left) In the spectral domain the phase of the output field is a constant while the amplitude is the same as the amplitude of the input field. (Right) Shows the time domain representation of the TL output field (in a) when taking its' Fourier transform.

If, however, amplitude and phase shaping are taken into consideration, it is found that the Gaussian TL-pulse is not the shortest pulse. A square amplitude pulse with a flat phase in frequency is a sync function in time. The time duration of the main feature of the sync function is shorter and intensity higher than that obtained for a TL-pulse. The transmission function which will convert the amplitude of the input field to a square amplitude and counter the phase of the input field can be seen in Figure 3.10(a). The transmission function can apply arbitrary amplitude values between 0 and 1 to an input field. Where 0 implies no light transmitted and 1 implies all light transmitted. The phase mask shown in (a) tends to remove light intensity in the centre of the field while trying to increase the skirts of the field. However, the applied amplitude cannot supersede 1 as this would imply amplification of the field in that region. In

the region where the amplitude of the transmission function is 1 the structure of the input field will carry on with no change. This implies that the side skirts of the input field will remain as part of the output field amplitude. The Fourier domain representation of the field after the transmission function in (a) is shown in (b). ((b) left) Shows the output field in the spectral domain while ((b) right) shows the time domain representation of the output field which was obtained using a Fourier transform. The main feature of the output field in time is approximately 108 fs exhibiting a relative peak intensity of 0.0225. Once again this transmission function was obtained considering a normalised energy of 1 mW per pulse.

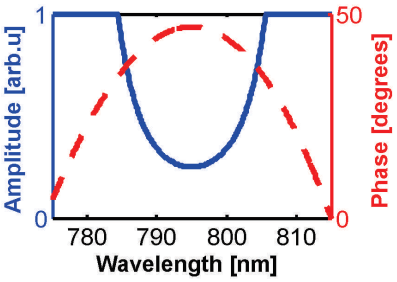

(a)

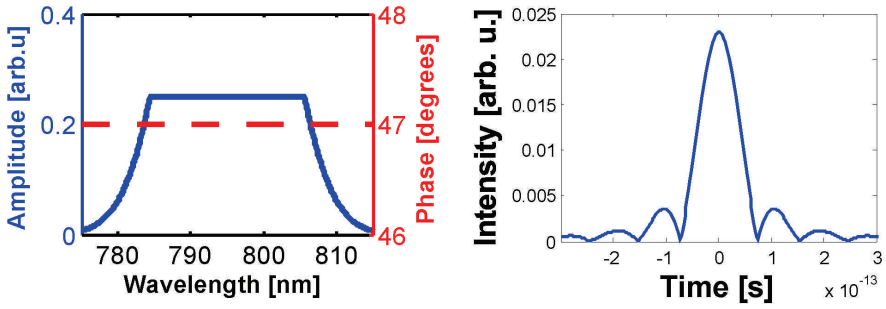

(b)

Figure 3.10: The anticipated transmission function when both amplitude and phase shaping is considered. Spectral domain representation of the transmission function which will lead to a square spectral shape and flat phase. (Blue line) The amplitude of the applied transmission function diminish energy in the centre of the input field while trying to increase the skirts of the Gaussian input field. The red dashed line is the phase which cancels the chirp on the input field. The amplitude were chosen to keep the energy normalised to 1 mW. Field output when the transmission function shown in (a) is applied to the input field shown in Figure 3.8. (Left) In the spectral domain the phase of the output field is a constant while the amplitude is shaped in the form of a flat-top profile. (Right) Shows the time domain representation of the output field which is a sinc function distributed in time. The sinc function does have pre- and post-pulse structures while the main future still has a shorter pulse duration and an intensity higher than that obtained for the TL-pulse when only phase shaping was considered.

The initial postulate was that the shortest pulse duration will lead to the highest intensity, henceforth the largest second harmonic signal. The mask in Figure 3.10 (a) is therefore a more probable solution than that of Figure 3.9(a) and is considered a viable solution the learning

algorithm might find. These are however only intuitive guesses and in this work there is no mathematical proof that the learning algorithm will find these masks as the optimal solutions. These transmission functions are a good starting point which should be tested and verified.

3.4.2 Simulating Learning Algorithm Optimization of SHG

Simulating SHG was done using equation 3.11 where perfect phase matching was considered such that $\Delta k = 0$. According to equation 3.11 $I_{SHG}(2\omega) \propto I_{in}^2(\omega)$ and therefore $I_{SHG}(2\omega) \propto A_{in}^4(\omega)$. The target function and consequently the fitness assigned to a field is expressed as,

$$F_{target} = \sum_n \frac{\left(\mathcal{F}\left\{T(\omega_n)\,\tilde{E}_{in}(\omega_n)\right\}\right)^4}{\left(\mathcal{F}\left\{\tilde{E}_{TL-Pulse}(\omega_n)\right\}\right)^4} \tag{3.12}$$

which is the Fourier transform of the spectral domain output taken to the 4^{th} order and summed over all the spectral components. In equation 3.12 the fitness value assigned to the output fields are also normalised relative to the case where the output field is a transform limited pulse. If only phase shaping is considered the numerically extracted mask which lead to the highest target value is shown in Figure 3.11 (a). The output of the field within the temporal domain is shown in Figure 3.11(b) when compared to a TL-pulse.

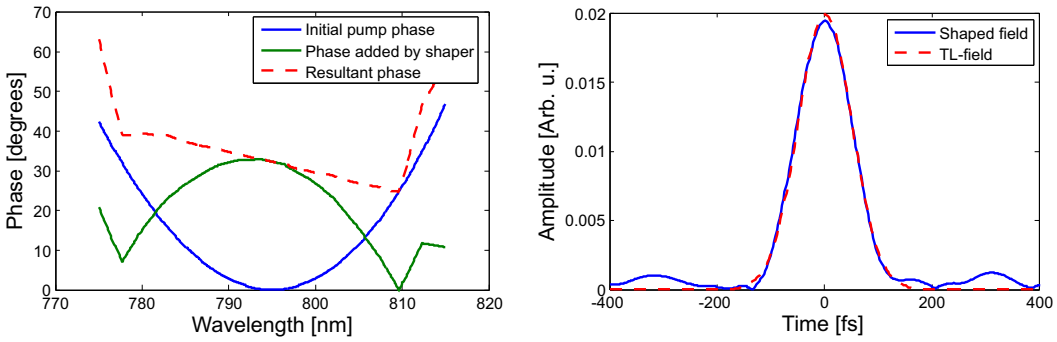

(a) (b)

Figure 3.11: Phase only shaping used to compress a stretched input field. (a) Shows the spectral domain representation of the numerically extracted phase mask which will compress a chirped input field during SHG. (b) Shows the output field in the time domain when using the mask shown in (a) compared to a TL-pulse. showing good agreement.

As anticipated, if phase only shaping takes place the phase mask removes the pulse chirp leading to a transform limited pulse afterwards. Figure 3.11(b) show excellent qualitative agreement between the extracted field and a TL-pulse with a fitness value close to 96 %. In section 3.4.1 a pulse consisting of a flat-top spectral profile and flat phase exhibiting higher intensities than a TL-pulse is shown. Therefore, if the pulse energy is kept fixed, fitness values larger than 1 should be attainable if amplitude shaping is also considered. As mentioned in section

3.3.1 several parameters define the size of the solution space and how long it takes the learning algorithm to converge to a solution. The effects these parameters exhibit on how the learning algorithm traverse the solution landscape should be tested and commented on. Several different bin sizes as well as precision values were used for the spectral as well as the von Neumann basis as shown in tables 3.1a and 3.1b for the various bases, respectively. In table 3.1a for a fixed spectral bandwidth the column wavelength bins determine the wavelength resolution considered while the amplitude and phase columns represents the number of possible values each parameter may have. These altogether provide the number of possible solutions within the bases (shown in the fourth column) for the wavelength bins as well as amplitude and phase precision parameters used. These parameters are the same for table 3.1b with the exception that temporal bins also exist which determines the temporal resolution.

For the Fourier domain it was only possible to obtain feasible results for small parameter spaces. When using a large parameter space the learning algorithm did not converge in the specified number of generations. The learning algorithm was used 5 consecutive times for each of the cases mentioned in table 3.1a and 3.1b. Out of these 5 cases the best fitness for each generation is plotted in figure 3.12 for the case which leads to the highest fitness after the 160 generations. In figure 3.12 the dashed lines were obtained using the Fourier and the solid lines using the von Neumann domains. Even though convergence occurred using either basis, a significant difference can be observed between the way they operated.

Wavelength bins	Amplitude	Phase	Number of possible solutions
11	10	10	1100
16	11	11	1936
24	10	10	2400

(a) Fourier domain parameter space considered

Wavelength bins	Time bins	Amplitude	Phase	Number of possible solutions
7	3	12	8	2016
7	3	14	8	2352
8	6	12	8	4608
9	7	12	9	6804
16	10	12	8	15360
12	8	12	8	9216
12	8	12	10	11520
12	8	16	10	15360
12	8	40	20	76800
12	8	>50	>50	>240000
16	10	>50	>50	>400000

(b) von Neumann parameter space considered

Table 3.1: Learning algorithm parameter space for the various bases.

When using the Fourier domain basis the largest parameter space obtainable while still converging to good solutions pertaining to fitness values higher than 0.80 were 48. The best results obtained when using the Fourier domain were for a parameter space of 22 which corresponds

to 11 amplitude and 11 phase bins. This parameter space is quite small and results in poor spectral resolution. If the solution sought were more complex, e.g. a mask to create a double pulse, a parameter space size such as this would not be able to resolve the structure adequately. However, the von Neumann domain shows more promising results. The von Neumann basis operated much better on larger parameter spaces and fitness values higher than 1 were obtained even in some cases for parameter spaces up to 160. When the parameter space was small as in the case for 7 wavelength bins and 3 temporal bins the learning algorithm operating on the von Neumann basis had difficulty converging to high fitness values. When the parameter space was large good results were obtained. For a maximum of 160 generations using a parameter space as large as 160 led to fitness values higher than that obtained for a parameter space of 32 for the Fourier domain.

From figure 3.12 it is clear that all the parameter space sizes are similar for about the first 40 generations. From this point onward the von Neumann basis outperforms the Fourier basis almost every time, except in the cases where the parameter space is drastically reduced when using the von Neumann basis. As explained earlier not having to reduce the parameter space is a big advantage for coherent control experiments as a larger parameter space allows more complex solutions.

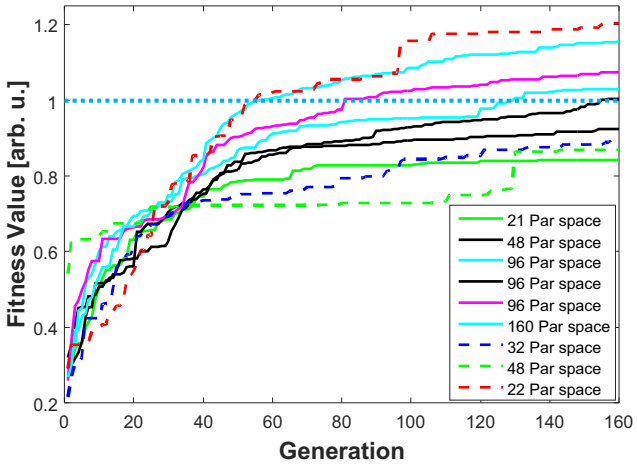

Figure 3.12: Shown here is the best fitness value obtained after each generation when the learning algorithm is set to find a mask which will optimise the fitness value determined using equation 3.12. The dashed lines are the numerical results when using the Fourier domain while the solid lines are the ones when using the von Neumann domain. Each line represents a different parameter space size according to the data shown in table 3.1. The horizontal dotted line is the maximum SHG achievable if only phase matching is considered.

Examples of masks extracted during numerical simulations which led to high peak intensities can be seen in Figure 3.13 (a) when using the spectral domain considering 11 amplitude and 11 phase bins and 3.13 (b) when using the von Neumann domain with 12 frequency bins and 8 temporal bins.

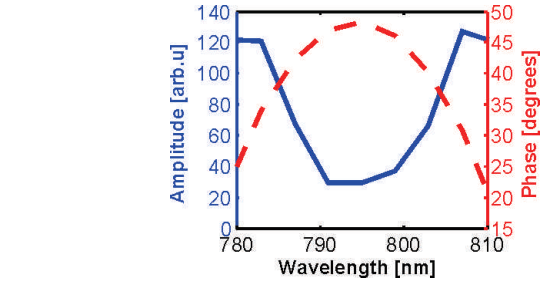

(a)

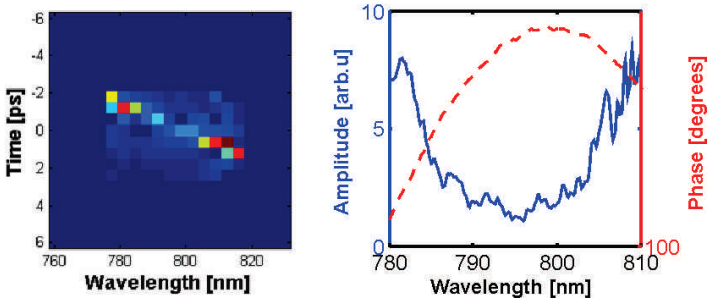

(b)

Figure 3.13: Examples of masks extracted by the learning algorithm during simulations which lead to high second harmonic signals. Mask extracted by the learning algorithm during simulations when operating on the spectral domain. (1) Is the mask extracted by the learning algorithm during simulations when operating on the von Neumann domain while (2) show its spectral domain equivalence obtained using equation 3.8.

For both bases the masks extracted represents those shown in Figure 3.10 representing a flat-top in frequency space and not that of Figure 3.9 for a transform limited field. This emphasizes the importance of amplitude and phase modulation rather than just phase modulation. During the simulations it became clear that the von Neumann basis is able to efficiently represent pulse information, but the 2-d learning algorithm developed also converged faster that the learning algorithm operating on the spectral domain even though the parameter space size was larger within the von Neumann domain.

3.4.3 Learning Algorithm Optimizing SHG Experimentally

A time and frequency shaping device (Dazzler) was placed after an oscillator (Coherent, Mira) and before an amplifier (Coherent, Legend) such that the pulses from the oscillator were shaped and in turn amplified. During the amplification stage an almost transform-limited pulse (close to 120 fs) was stretched and amplified, but only partially compressed afterwards leading to a pulse duration roughly 1.1 ps. Adding phase masks onto the Dazzler while aided by SHG measurements, the genetic algorithm was now required to find a mask which will correct the poor compression. The experimental setup used for SHG can be seen in fig 3.14. The pulse after the amplifier is used to pump a non-linear BBO crystal generating a second harmonic

field. Using an uncoated prism the fundamental was separated from the first harmonic allowing the second harmonic signal to be measured with a fast photo diode.

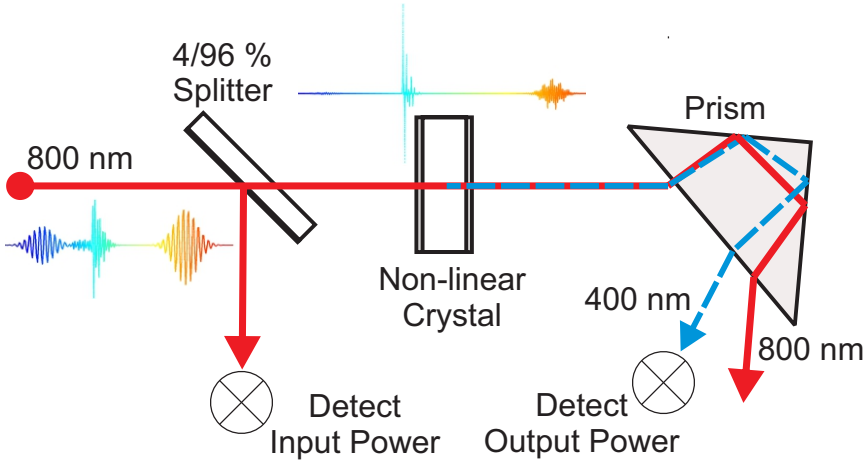

Figure 3.14: Experimental setup used for SHG and power stabilization. 4 % of the input field is tapped from the shaped pulse and used as reference to change the output power to normalise it to some predefined value. The rest of the field passes through the non-linear crystal and generate SH. Using a prism the SH is split from the fundamental and measured with a fast photo diode.

To be able to compare different pulse structures one requires the energy for each pulse to be the same. Because the Dazzler was placed between the oscillator and the amplifier the output energy of the pulses will vary. This predicament was avoided or the effect minimised by adjusting the Dazzler output power such that all the pulses after the amplifier would have the same energy or would be within 3 % of the set value. However, the Dazzler power setting does not correlate linearly to the pulse power after the amplifier since the amplifier response is nonlinear with regards to the seed input. For each pulse amplified several Dazzler power settings were applied and power after the amplifier measured. This was achieved by tapping off a fraction of the energy with a glass plate, as shown in the setup. Non-linear data fitting applied to these measurements allowed one to extrapolate which Dazzler power setting will lead to the normalization of the amplified pulses.

Frequency bins	Amplitude	Phase	Number of possible solutions
11	10	10	12100
16	10	10	25600

(a) Fourier domain parameter space considered.

Frequency bins	Time	Amplitude	Phase	Number of possible solutions
8	6	10	10	4800
12	8	10	10	9600

(b) von Neumann parameter space considered.

Table 3.2: Learning algorithm parameter space for the various bases during experiments.

Figure 3.15 shows the experimental results obtained are similar to the results obtained numerically. Once again the von Neumann basis outperforms the results obtained for the Fourier domain at a very early stage. After about 8 generations the von Neumann basis exceeds that of the Fourier domain. After approximately 80 generations the Fourier domain fitness results are equivalent to those of the von Neumann basis where upon only small changes can be observed. It took the Fourier domain (with a parameter space of 32) roughly 70 generations to become comparable with the von Neumann basis (with a parameter space of 96). One can also see the solutions for the different bases do however converge to similar results if the experiment is allowed to run over enough populations.

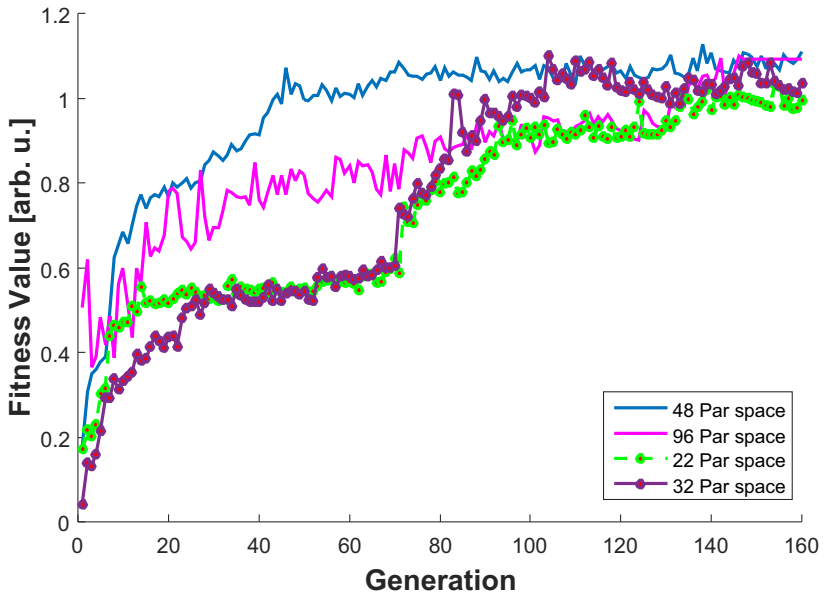

Figure 3.15: Shows experimentally obtained results for both the Fourier and von Neumann bases used as indicated in table 3.2.

After about 140 populations only small improvements can be seen for the fitness value. Even though the learning algorithm converged, higher fitness values were expected according to the simulations and the anticipated optimal solution. For experiments however power stabilization had to be done to ensure pulse energies are the same. The power stabilization had a 3 % tolerance between pulses. At this stage of the experiment the learning algorithm optimized the second harmonic signal to the extent where the stabilization tolerance lead to the noise exceeding the changes in fitness due to better solutions. Therefore the learning algorithm cannot distinguish if a high fitness is due to a better signal or due to noise. It was not feasible to use the same parameter space for the different bases as once again the von Neumann basis prefers a large parameter space while the Fourier prefers a small parameter space. The learning algorithm does not converge when using a large parameter space in the Fourier domain.

Examples of masks extracted which led to high experimental SHG signals can be seen in Figure 3.16 (a) and 3.16 (b) for the Fourier and von Neumann bases, respectively. From Fig.

3.10 it is expected that the mask which leads to the strongest pulse compression is the mask which cancels out the phase profile to produce a flat phase, as well as do amplitude correction leading to a flat spectral profile.

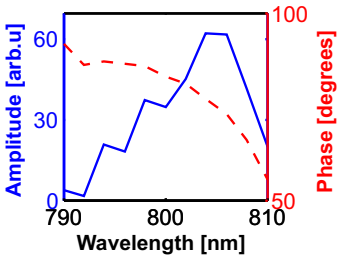

(a)

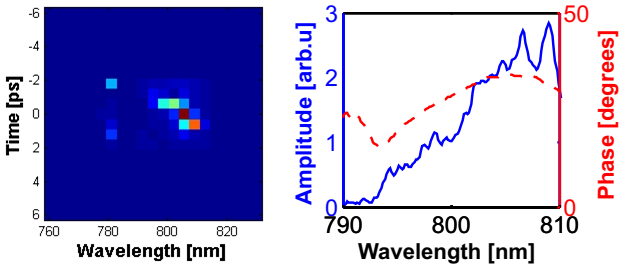

(b)

Figure 3.16: Here we show the best experimentally extracted mask. In (a) the expected optimal solution can be seen. In (b) and (c) the numerically and experimentally extracted masks are shown. (1) Mask extracted by the learning algorithm using representing information in the spectral domain. The output field in frequency (2.1) and time (2.2) after applying the mask shown in (1). (1.1) von Neumann lattice extracted with the learning algorithm while (1.2) show the frequency domain equivalent of that shown in (1.1)

For the experimentally extracted masks shown in Figure 3.16 second harmonic generation frequency-resolved optical gating (SHG-FROG) measurements were taken and can be seen in Figure 3.17. Analyzing the SHG-FROG traces for the spectral and von Neumann representation show the pulse wavelength centered around 805 nm and not 795 nm. The bandwidth extracted is also shorter than that anticipated which leads to longer pulse durations. Figure 3.17 show wavelengths below 790 nm have no noticeable impact on the SHG signal.

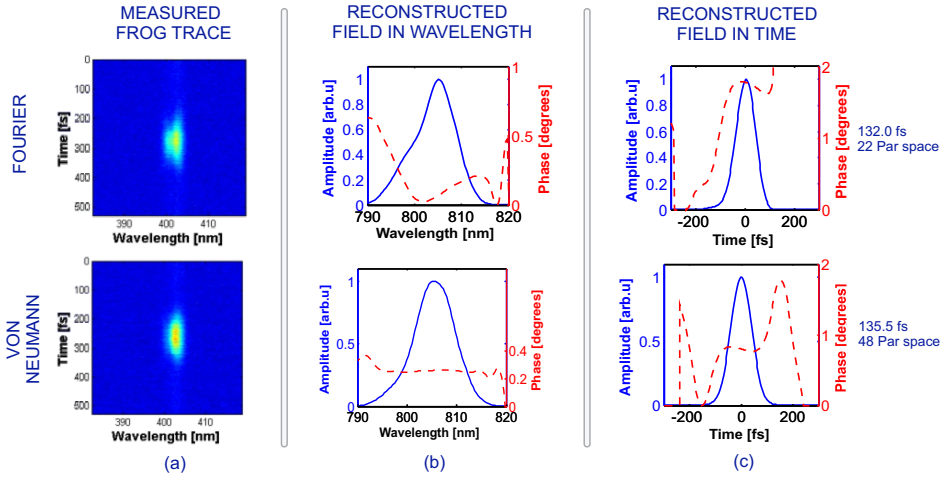

Figure 3.17: Measurements of the SHG-FROG traces for the highest fitness obtained for experiments. The SHG-FROG traces in (a) were used to extract the wavelength and temporal representations of the pulses.

This is contradictory to theoretical numerical initial expectations. What is shown is a pulse duration which is longer than a transform limited pulse by 30%, and centered at a different wavelength, but which leads to a stronger SH signal. This is likely the consequence of improved phase matching for frequency doubling at 805 nm, than at 795 nm for the particular crystal cut-angle used in this experiment, but this hypothesis remains to be tested.

3.5 Summary and Comparison

The work presented within this chapter showed the von Neumann basis is a viable alternative to the Fourier (spectral) domain when it comes to representing pulse information. When used within a learning algorithm the von Neumann basis outperformed the spectral domain with regards to convergence time during both simulations and experiments. Given enough time though the solutions obtained using the spectral domain and von Neumann domain do start to converge to the same fitness. However, when using the Fourier domain good results were only obtained when using small parameter spaces contrary to the von Neumann basis requiring large parameter spaces for good results.

A large parameter space is advantageous as it leads to a higher resolution and consequently allowing more solutions in comparison to a small parameter space. However, a large parameter space drastically increases the time it takes for a learning algorithm to convergence in the case of the Fourier domain. This, however, is not the case when using the von Neumann basis.

During simulations this study showed the shortest pulse originate from a flat-top amplitude distribution within the spectral domain. The experimental results highlighted the fact that the crystal was designed for frequency doubling of 800 nm and not 795nm. Hence, the experimentally extracted phase mask shifted the central position of the spectrum to a higher spectral region. In the past phases information has been considered as the main contributing factor

during processes. In the work which has been shown here, amplitude effects cannot simply be ignored. It is also evident that amplitude shaping cannot be neglected as has been done in the past as itself might change some of the dynamics influencing the parameters we would like to characterise. Energy conservation, henceforth, phase matching, proved to be quite significant. During experimental optimization as well as simulating optimizing the SHG phase matching proved to outweigh the effects of pulse duration.

Chapter 4

Theory: Molecular Vibrational Modes and CARS

4.1 Introduction

In this chapter theory is derived related to light-matter interactions limiting our analysis to vibrational excitations as described in the book of nonlinear optics written by Boyd [74]. Vibrational excitation can be realized in several ways. Direct excitation (for infrared active modes) where the frequency of the applied pump field is on resonance with the mode [75, 76], spontaneous Raman scattering, as well as stimulated Raman Scattering (SRS) where the beat frequency between a pump and Stokes field is on resonant with an excitation [77, 78]. On-resonant excitations require light sources exhibiting low optical frequencies not always available due to the low energy associated with direct vibrational excitations. For the work presented here stimulated Raman processes were considered as means of excitation.

This chapter presents an overview of Coherent Anti-Stokes Raman Scattering (CARS) [79] in section 4.2, what the Raman effect is and how it works [80]. Information is provided on the history of CARS as well as which CARS methods are currently in use. The CARS setup that was used in this study which leads to minimization of the background caused by four wave mixing as well as background due to the various fields interchanging their functionality is illustrated. This is followed by section 4.3 providing general information about the CO_2 molecule investigated in this study, as well as considerations when working with gas ensembles and chemical reactions. A quantum mechanical description developed in section 4.4 will allow us to describe the light matter interaction in detail. Theory is first derived in section 4.4.1 for the process of Stimulated Raman Scattering (SRS) based on perturbation theory applied to the time-dependent Schrödinger equation. SRS allows one to vibrationally excite molecules, but to observe these excitations one also requires some spectroscopic diagnostic tool to analyse the ensemble's current state. This is accomplished making use of anti-Stokes scattering which forms the second part of Coherent Anti-Stokes Raman Scattering (CARS). CARS is a coherent process which follows when a stimulated Raman excitation is probed with a probe field generating an

anti-Stokes signal. If the probe field is a narrowband source the anti-Stokes signal gives a direct representation of the modes populated during the SRS process. Section 4.4.2 builds on the theory derived for SRS to derive a quantum mechanical description for CARS. This enables one to simulate CARS and bring one to the heart of the work presented here, which is to control the way the molecules are vibrationally excited and probe the ensemble afterwards. Different pump fields will lead to different vibrational excitations and different correlations between the various modes. The question is not if we can vibrationally excite molecules, but rather which field structure will populate which mode and what mechanism is responsible for this. The ultimate aim is to develop arbitrary control over the vibrational dynamics with this technique. After this thorough quantum mechanical derivation (in section 4.4.3) the background noise which might obscure the measured CARS signal will receive attention.

4.2 Overview on CARS

4.2.1 The Raman Effect and CARS

Raman scattering is based on inelastic scattering of light from material and was first observed by C.V. Raman and independently by Grigory Landsberg in 1928 [81]. When light is scattered by particles some of the photons are Raleigh scattered and do not change their frequency. During Raman scattering a fraction of the photons do change their frequencies and consequently convey information regarding the properties of the scattering media. Mainly two types of scattering can be distinguished which relates to the Raman effect. The occurrence where the signal is shifted towards longer wavelengths (red shifted) is also known as Stokes scattering and the occurrence where the signal is shifted towards shorter wavelengths (blue shifted) is also known as anti-Stokes scattering. In both cases the shift is by the energy difference between the initial and final states. The change in state of the molecule can be either in its electronic, vibrational or rotational degrees of freedom. For the purposes of this study, only vibrational Raman processes will be considered. The difference between Stokes and anti-Stokes scattering is that Stokes scattering usually is a consequence of the excitation of molecules, while anti-Stokes scattering is associated with depopulating (de-exciting) an excited state to a state with lower energy. Spontaneous Raman scattering occurs in all directions with a polarization that has no fixed relation to the polarization of the input fields. This implies that spontaneous Raman scattering is incoherent and any phase information that there might have been is lost during measurements due to this incoherency. Figure 4.1 shows the energy scheme for Raleigh and the two Raman scattering processes.

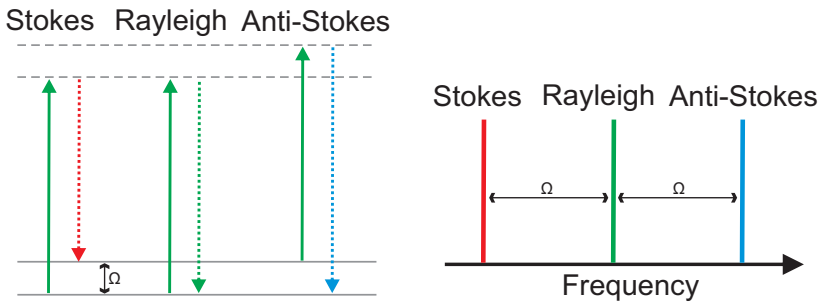

Figure 4.1: In this figure the Stokes, Anti-Stokes and Raleigh scattering effects are shown.

The spontaneous Raman scattering signal is directly proportional to the average number of molecules found in each of the modes of the molecule. By using very narrow band pump fields high precision measurements of the Raman spectrum can be made because the energy associated with a vibrational excitation is the absolute value of the energy difference between a narrowband pump and the Raman scattered light. Even though this spectroscopic technique effectively maps molecular energy structures, it has a poor signal-to-noise ratio due to the incoherent spontaneous generation of the signal in comparison to a coherent signal generated by stimulated Raman scattering.

Light scattering phenomena involving two or more photons interacting were not discovered until the 1960's when laser sources became available, even though they were predicted as early as the 1930's. Maker and Terhune were the first to observe CARS during their investigation of the third order polarization, $\chi^{(3)}$, response of benzene [82]. During their investigation they found that when illuminating benzene with two fields they observed a blue-shifted signal. They also noticed the signal strength increased when the energy difference of the fields matched the vibrational modes of the sample. Only in 1965 were the process of coherent Anti-Stokes Raman scattering christened as CARS by Begley et. al [83]. Because CARS stems from SRS it is found that in the ideal case both CARS and Raman scattering yield spectra which resembles the vibrational resonance structures of the molecules.

To Illustrate CARS, the experimental situation of two overlapping coherent monochromatic light sources of frequency ω_1 and ω_2 (such that $\omega_1 > \omega_2$) are considered. Propagating through material exhibiting non-linearity several frequencies can be generated from various combinations of the two light sources. Several non-linear processes, not to mention several different Raman scattering processes can occur. For the purposes of this study, only the combination $\omega_3 = 2\omega_1 - \omega_2$ shown in Figure 4.2 leading to CARS is of interest. In this depiction ω_1 gives the frequency of both the pump and probe fields whilst ω_2 gives the frequency of the Stokes field.

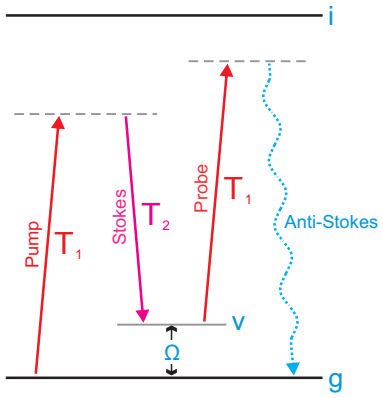

Figure 4.2: Illustrating CARS for a 3-level molecule.

If ω_1 is on-resonant with an electronic excited state while $\omega_1 - \omega_2$ gives the energy of a molecular vibrational transition it is referred to as an on-resonant stimulated Raman transition. In this work only the case where $\omega_1 - \omega_2$ gives the energy of a molecular vibrational transition while ω_1 is far off-resonant from any electronic state (also known as off-resonant stimulated Raman scattering) is considered. Following stimulated Raman scattering, a probe field interacts with the molecules leading to an anti-Stokes signal and completing the CARS process. Classically CARS is categorised as a coherent non-linear process which closely similar to four-wave mixing because $\omega_3 = 2\omega_1 - \omega_2$. In contrast to Spontaneous Raman Scattering, CARS is coherent and directional with small directional deviations. This directionality is a consequence of the spatial and temporal coherence between the molecules. The Spontaneous Raman Scattering intensity is linearly proportional to the concentration of the sample and the incident field intensity. While for CARS one finds its signal intensity is proportional to the square of the concentration of the number of scattering molecules and the product of the pump, Stokes and probe field intensities [79],

$$E_{as}(t) \quad \propto \quad \chi^{(3)} E_p(t) E_s^*(t) E_{pr}(t). \tag{4.1}$$

The subscript as denotes the generated anti-Stokes signal while p, s, and pr represents the pump, Stokes and probe fields, respectively. There is however a major downside when using CARS. Unfortunately, the anti-Stokes signal has the drawback of being modified according to the shape of the probe spectrum. For instance a broadband probe broadens the anti-Stokes signal lineshape such that it will not resemble the actual vibrational lineshape. This spectral modification can however be minimized by using a field with a narrowband frequency spectrum as the probe.

Since the first observation of CARS its use has spread to multidisciplinary fields of research and today is typically found in biological imaging, chemical diagnosis and for measuring the temperature during combustion, just to name a few [84, 85, 86]. It also has proven to be a useful in inline remote chemical detection method, which cannot be measured using Spontaneous

Raman Scattering due to weak signals [87]. What makes this technique so attractive is that for low field intensities it allows one to probe and acquire information about a sample without destroying it. This was experimentally shown by X.S. Xie and coworkers which also lead to noninvasive chemical-specific imaging in brain matter [85].

4.2.2 CARS as a Coherent Spectroscopic Technique

A vibrational wave packet arises when a coherent superposition of several vibrational eigenstates are populated at the same time. The wave-packet propagates back and forth in the bound state potential with a periodicity dependent on the energy difference between the vibrational modes. Development in the research area of wave-packet dynamics only gained momentum after the invention of ultrashort laser pulses. The femtosecond time scale is short enough that the nuclear configuration does not change during the interaction with a laser pulse. For longer pulses one may find the wave-packet starts to propagate during the excitation. Longer pulses also have shorter frequency bandwidths which might not be broad enough to cover several modes. More details about wave packets can be reviewed in [88].

Coherent spectroscopy is based either on the coherent excitation of atoms and molecules or the superposition of coherent light scattered by molecules [89]. Coherent molecular excitation by coherent laser sources establishes a well defined phase relation between the molecular wave functions and the laser field oscillations. SRS and therefore CARS are typical coherent processes, even though spontaneous Raman scattering is an incoherent process. During the excitation step of SRS, two or more vibrational modes can be coherently excited simultaneously due to coherence of the sources and the broad bandwidth of the pump field allowing several modes to be occupied at the same time. As just mentioned, this establishes a fixed phase relation between the amplitudes of the wave-functions of the excited vibrational modes which ultimately leads to a wave-packet that propagates in time. In addition to this, an ensemble of the molecules will simultaneously be excited to the same vibrational modes and evidently result in a spatial distribution of coherent excited molecules. This spatial coherence between molecules leads to a directional emission of the anti-Stokes light simplifying detection of CARS, while by contrast the signal generated from spontaneous Raman scattering is distributed over 4π steradians solid angle.

The wave-packet, created during SRS, in turn determines the total amplitudes of the emitted, scattered or absorbed radiation when the material is irradiated with another light field. This implies that if SRS is coherent then so is CARS. For CARS we find that both spectral and temporal coherent attributes are transferred from the molecules to the generated anti-Stokes signal. Not only is the CARS signal coherent, but it shows time dependent behaviour which cannot be observed during spontaneous Raman scattering. The molecular wave-packet propagates in time which implies the CARS signal created is also dependent on the temporal attributes and delay between the excitation pulses. This can lead to temporal control of when and how the wave-packet was created. The time dependence of the CARS signal now enables one to do time-resolved (TR) spectroscopy on the propagating wave-packet. SRS differs from TR-CARS as SRS de-excites in all directions at any given time such that the signal detection coherence is

lost. However, the TR-CARS anti-Stokes signal is generated by a coherent probe field retaining the vibrational coherence and phase information between the molecules [88, 79].

4.2.3 Overview on Current CARS Methods

Several CARS techniques have been developed over the years. Understanding the strengths and weaknesses of each CARS method can provide guidance in deciding which one suits a particular problem the best. For convenience, CARS can mainly be categorized into two types: spectral domain and temporal domain methods [79, 86]. CW Single frequency lasers has been implemented for spectral CARS spectroscopy as early as the 70's. Keeping one laser frequency fixed while spectrally scanning the other has lead to high resolution imaging of the rotational excitation of the molecules due to the narrow bandwidth of the CW laser sources used [90]. No temporal information of the modes could however be ascertained.

Only after the development of pulsed laser sources (in the ps regime) could time resolved CARS measurements be made [91], with the exception that a pulsed source consists of a bandwidth of frequencies which inevitable broadens the spectral image in comparison to CW CARS [91]. For long decoherence lifetimes these pico-second fields were also used to measure the decoherence lifetime of the several excited modes. Even though time-resolved methods slows down the signal collection speed, they allow one to investigate the dynamics of the excited vibrational modes previously not possible with CW CARS [92]. Furthermore, a Fourier transform on the collected time-resolved CARS signals provide information on the mode spacing and lifetimes [93]. Since the arrival of femto-second laser pulses several new CARS schemes have been implemented. A broadband source now allows several modes to be occupied and measured simultaneously. Polarization selective CARS furthermore aid in suppressing unavoidable background noise. Also making use of box-CARS can lead to the suppression of the background noise due to the fields propagating non-collinearly . More information with regards to the different methods will now be provided.

Narrowband CARS

Even though the first CARS experiment was conducted in 1965 it was only during the 70s that substantial development in CARS became visible due to the availability of new tunable laser sources [79]. Typically, narrowband CARS is based on keeping the frequency of the narrowband pump source fixed while frequency scanning the narrowband Stokes source to populate the various modes followed by probing the molecular ensemble with a narrowband probe field [94].

The main advantage with respect to narrowband CARS is found when resolving the resonance structures of molecules and its related linewidths. When using broadband pump and Stokes fields different frequency combinations within the pump and Stokes bands can be on resonant with the vibrational mode excitations. For such broadband excitation one cannot distinguish between the various pump-Stokes combinations that excite the mode. Comparing the anti-Stokes signal strength while frequency scanning one of the sources provides information on the linewidths and line strength of the modes. Therefore, narrowband pump and Stokes fields lowers the number

of pump-Stokes wavelength combinations that can simultaneously be on resonant with a mode and in doing so increase the spectral resolution at the cost of signal strength. This method is particularly useful in cases were normal Raman gives low signals or in the presence of high background noise, as in the case when measuring the temperature in fuel combustion where high temperature is to be expected [84]. In this particular case the CARS measurement relates to rotational line intensities where the temperature can be extracted using Boltzmann's rotation state partition function.

Narrowband CARS has two main disadvantages. Narrow spectral bandwidth laser fields have long pulse durations and therefore consists of low field intensities which according to equation 4.1 implies low intensities for the generated CARS signals. Typically a spectrometer with a photo-multiplier tube have to be used for these type of experiments. Also scanning the frequency of one of the sources is fairly time consuming and is not an attractive method when working under circumstances where fast measurements are required. This is why multiplex CARS is rather used.

Single-beam and Multiplex CARS

Measuring the spectra of turbulent gases in combustion requires faster measuring speeds. The time consuming frequency scanning method can be avoided using a broadband source for either the pump or Stokes field while keeping the second source for SRS spectrally narrow. This will excite several modes simultaneously and is known as multiplex CARS [2, 87]. The first experiment of Anti-Stokes Raman scattering conducted with multiplexing was not coherent because one of the excitation sources was a modeless dye lasers emitting incoherent radiation. Today however the broadband sources used to conduct these experiments are mode-locked lasers leading to coherent excitation.

Multiplex CARS is a frequency domain method where one would like the probe field to be spectrally narrow to obtain good spectral resolution at the anti-Stokes radiation. For most CARS experiments the pump itself is also used as the probe field. The pump is therefore chosen spectrally narrow while a broadband source is used as the Stokes field. The narrowband probe ensures the measured anti-Stokes radiation provides good resolution of the excited vibrational modes. Thus multiple modes are measured without having to scan over the frequency.

Since its first appearance multiplex CARS has improved drastically and today incorporates concepts like pulse shaping as well as mode selectivity during SRS. Coherent broadband sources maintain a fixed phase relation between its different spectral components. This phase relation opens up new possibilities of exploiting quantum mechanical interference effects by manipulating the spectral phase of a field before interacting with material. One of the main applications of pulse shaping is in ultra broadband single pulse multiplex CARS which were first demonstrated by Y. Silberberg and coworkers [37, 2]. In this technique a narrowband spectral component is selected form the blue edge of a broad spectrum and temporally delayed with respect to the spectral components responsible for vibrational excitation. This narrowband spectral component serves as the probe field. Single pulse CARS simplifies the experimental setup significantly. Temporal and spatial overlap is a direct consequence when using a single unchirped coherent

field as pump, Stokes and probe. Figure 4.3 illustrates the concept of ultra broadband single pulse phase shaping for multiplex CARS.

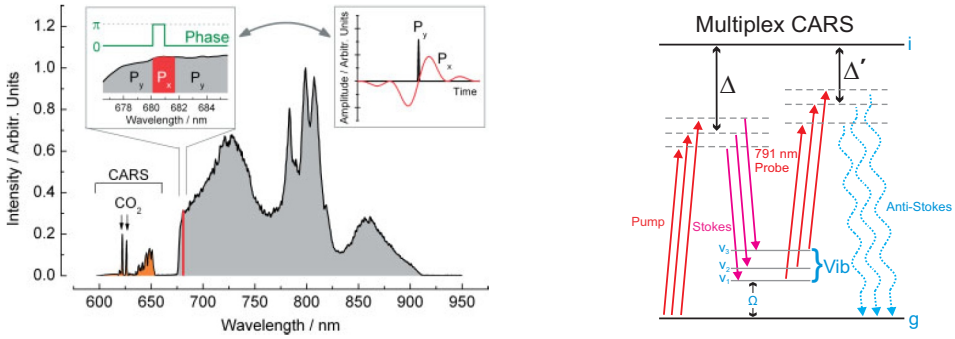

(a) (b)

Figure 4.3: Single pulse CARS. (a) A single pulse is used to excite vibrational modes, as well as probe the ensemble afterwards. A part of the spectrum on the blue edge of the field is used as the probe (courtesy of J.R. Gord and co-workers [2]). (b) A broadband field is used to excite several vibrational modes at the same time while a section of the field is used to probe the modes populated.

Another well known use of pulse shaping is mode selectivity. Proof of principle for mode selective CARS was achieved by the group of Lozovoy et. al. to detect several different chemicals from a distance away [87]. Using a learning algorithm to achieve mode selectivity has also been shown by the group of Z. Wang and co-workers [95]. However, till thus far no control over the relative phase of the oscillation between the different vibrational modes been shown. Neither was the effect of the laser sources on the relative oscillation amplitude investigated. The work presented here will address this in more detail. In narrowband CARS mode selectivity is easily achieved because the pump and probe fields will not be on-resonant with two modes simultaneously. Scanning one of the frequencies lead to selecting a particular mode. This only allows one to select one mode at a time.

Today several pulse shaping approaches exist which allows mode selectivity. Most of these concentrate on the temporal overlap between the pump and Stokes fields where the excitation probability is proportional to the temporal overlap. The first of its kind was achieved by chirping a broadband Stokes field while keeping the pump field fixed. This implies temporal overlap between the pump and Stokes will only be achieved for the desired modes. This was first proposed by Zheltikov and coworkers which was later verified by Pestov et al. [96, 79].

Silberberg and coworkers explored shaping based on single pulse impulsive Raman scattering [97]. In their work the phase was modulated with a sinusoidal phase which creates a pulse train in the time domain. If the pulse train match the period of a vibrational mode, it can effectively excite the molecule to that mode. In the frequency domain, the self-correlation of such a sinusoidal modulated pulse shows maxima at certain frequency and minima at others. This means excitation for certain resonances and suppression for others. The effect of sinusoidal spectral phase modulation in the frequency domain generates modulation on the field correlation

of pump and Stokes pulses and achieves the selective excitation. After the excitation of coherent vibration and probing, the total CARS signal is recorded with respect to the sinusoidal modulation period and is used to generate CARS spectrum. Similarly to the case for narrowband CARS, multiplex CARS also suffers from low peak powers because the field considered is not a transform limited pulse, but depends on the shaping applied.

Separating the signal from background noise can be a problem. This is why polarization techniques for frequency domain CARS are sometimes incorporated to suppress the background [98].

Polarization CARS

Till this far no mention has been made about how the CARS spectra relates to the polarization of the pump, probe and Stokes fields. Classically CARS is considered similar to a four-wave mixing process which depends on the 3^{rd} order nonlinear susceptibility $\chi^{(3)}$. Generally $\chi^{(3)}$ is a fourth rank tensor with 81 elements. The symmetry of the medium, however, greatly reduces the number of independent elements. For gaseous CO_2 which is isotropic only the elements $\chi^{(3)}_{xxxx}$, $\chi^{(3)}_{xxyy}$, $\chi^{(3)}_{xyxy}$, $\chi^{(3)}_{xxyy}$ are non-zero with [74],

$$\chi^{(3)}_{xxxx} = \chi^{(3)}_{xxyy} + \chi^{(3)}_{xyxy} + \chi^{(3)}_{xyyx}. \tag{4.2}$$

The subscript x represents horizontally or vertically polarised light while y assumes polarization perpendicular to the polarization of x. Depending on the incoming polarization of the various fields different elements of the tensor will be addressed. If all the fields are horizontally polarised then only $\chi^{(3)}_{xxxx}$ will contribute. $\chi^{(3)}_{xxxx}$ shows no partiality to any particular interaction order of the various fields which implies this term will contribute towards the desired CARS signal, but also towards background noise. For instance background noise will be a result of the pump acting as the probe and the probe acting as the pump. As $\chi^{(3)}_{xxxx}$ outweighs the other elements 3 to 1 the background contribution due to this element is quite problematic. If however the pump and Stokes fields are horizontally polarised while the probe is vertically polarised then only $\chi^{(3)}_{yyxx}$, $\chi^{(3)}_{yxyx}$ and $\chi^{(3)}_{yxxy}$ should be considered when conducting vertically polarised CARS signal measurements. This reduces the background noise, but does not completely remove it. The order of the pump and Stokes fields can still interchange as in the case for $\chi^{(3)}_{yxxy}$. Once again leading to undesirable non-resonant background [99, 100]. Though all the horizontally polarised non-resonant background is discarded.

It is clear that a small polarization orientation difference of roughly $5° - 10°$ exist between the resonant CARS and the non-resonant background [101]. When a polarizer is orientated in such a manner to minimise the background transmitted a small CARS signal will still be allowed through. This approach suppress the non-resonant signal, but also reduce the resonant CARS signal drastically. For strong CARS signals this should not be a problem though.

Time-resolved CARS

Frequency based CARS cannot provide any phase information and is therefore insufficient when one would like to resolve temporal aspects. To resolve temporal aspects one can make use of time-resolved CARS. Time-resolved coherent Anti-Stokes Raman scattering (TR-CARS) was only possible after the 1980's when laser pulse durations were shortened into the sub-picosecond range [79]. This was followed by Zewail et. al. who paved the way forward pioneering the field of photo-chemistry with their work on molecular dynamics [102, 103]. For the first time ever it was possible to observe the temporal domain molecular coherence. It also became clear that the temporal domain vibrational wave-packet can reflect the vibrational spacing through a Fourier transform [104].

Nowadays pump-probe experiments are some of the most widely used schemes in femto-chemistry. A coherent pump field excites several modes of the molecular ensemble creating a wave-packet. A probe field incident on the ensemble is now temporally delayed relative to the pump field causing the ensemble to de-excite releasing the energy in the form of light. The emitted radiation carry temporal information about the ensemble before de-excitation. Time-resolved CARS can be generalized as a pump-probe experiment if SRS is regarded as the pump in the pump-dump scheme.

During multiplex CARS, SRS prepares a Raman wave-packet. The molecules are now allowed to evolve over time. This is followed by a probe field which forces the molecules to dump the energy in the form of an anti-Stokes signal which reflects the temporal evolution of the prepared vibrational wave packet [105, 48]. If the probe field was temporally delayed by a variable time delay the CARS signal will supply information regarding the molecular evolution during the delay time.

Initially, TR-CARS was used to investigate the dephasing of vibrational modes by observing the anti-Stokes signal which decreases due to dephasing [106]. Even though the dephasing can be inferred from the measured lineshape using frequency domain CARS, the direct time domain measurement can provide more accurately data related to temporal dephasing [92]. A remarkable trait of TR-CARS spectrographs is that it beats (also known as quantum beats or polarization beating) at the frequencies resembling the energy difference between Raman modes, which is a purely quantum mechanical phenomena [48]. Therefore, a Fourier transform of the time evolution of a TR-CARS spectrograph can determine the beat frequencies between a molecules' modes and consequently the frequency of the modes occupied.

TR-CARS signal strengths are usually strong in comparison to frequency domain CARS. This is due to the short pulse durations from broadband sources which implies high peak powers. This however comes at a price. The temporal delays required lead to a slower trace collection time for TR-CARS. Examples of TR-CARS and polarization mode beating will be shown in section 4.4.4 for the CO_2 molecule after deriving the necessary theory to simulate the process.

CARS Used in the Work Presented

Taking the advantages and disadvantages of each CARS method into consideration it was decided to combine the polarization CARS with that of a temporally delayed probe field which will allow

to also perform TR-CARS measurements. For polarization CARS it was mentioned how other four-wave-mixing processes will contribute to the non-resonant background. One requirement for SRS is that the pump and Stokes fields have to temporally overlap, but for CARS it is only required that the probe follows some time later. A temporal delay for the probe which is longer than the overlap between the Stokes and probe field duration ensures no temporal overlap between the probe and the Stokes field as illustrated in Figure 4.4. This ensures the probe field will not act as the pump field.

The pump can however still generate a CARS signal by acting as a probe itself. A 90° rotation of the probe field polarization and measuring the anti-Stokes signal generated in the same polarization as the probe field ensures the pump field will not be confused with any signal generated by the pump field acting as probe [2]. Polarization dependent measurements were done making use of a polarizing beam splitter to separate the background from the signal.

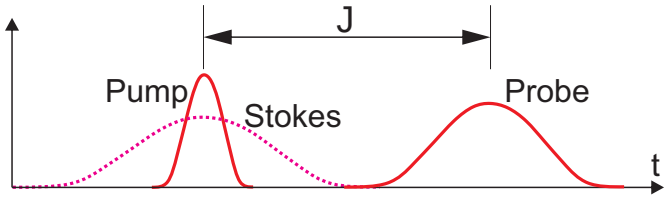

Figure 4.4: Illustration of the probe field temporally delayed relative to the pump and Stokes fields.

The measured CARS signal will therefore be free from four-wave-mixing background noise. The CARS signal generated will also predominantly be vertically polarised, while CARS caused by the pump field acting as the probe will be horizontally polarised. Our experimental setup will be discussed in detail in section 5.3. Tight focusing relaxes the phase matching conditions allowing one to collinearly propagate the various fields up to the ensemble.

Care should however be taken when considering the probe field used to generate the anti-Stokes signal. As will be shown in this study temporal and spectral attributes of the probe field inadvertently effect the anti-Stokes signal. Using a spectral narrowband probe field leads to good spectral, but poor temporal resolution. This is due to the long pulse duration of the probe field associated with narrowband sources. On the other hand using a probe field with a broadband frequency spectrum will result in good temporal, but poor spectral resolution. This is because transform limited broadband fields have short pulse durations. In practice, probe fields which are assumed monochromatic are used for spectral CARS while broadband sources are used for time-resolved CARS. In this study both spectral and temporal attributes will be investigated. A probe field is considered which reconcile these two domains, providing sufficient resolution in both time and frequency. The following sections briefly describe the various CARS methods developed in a chronological order.

4.3 Molecular Information and General Considerations

For the theory which will be derived in section 4.4 information with regards to the molecules studied is required. This is mainly to ensure assumptions and approximations made during the course of theoretical derivations are reasonable and resemble what is observed in practice. For instance, the theoretical derivations require fields far off-resonance from all electronic states. If this is not true on-resonant electronic excitations should be considered which falls outside the scope of the work presented here.

In this work studies were conducted on CO_2 gas molecules since literature on CO_2 is readily available and due to its significance and relevance in the scientific community. As a greenhouse gas CO_2 has been studied profusely over the last decade, where the studies conducted ranged from bond breaking to bond forming [107, 108, 109], all in the effort to convert CO_2 into some inert carbon compound or perhaps even form part of higher order carbonyls as fuel [110, 109]. Due to the symmetric nature of the CO_2 molecule it can also help establishing the building blocks for symmetric top molecules in general. For these reasons the scientific community shows a lot of interest in CO_2 and its symmetric structure even today.

In the section which follows background information on the CO_2 molecular orbital structure is provided [111, 112]. The electronic, vibrational and rotational modes possible are a direct consequence of this structure. For the vibrational modes under investigation the energy requirements as well as the selection rules which should be satisfied to populate these modes are illustrated. Spontaneous decay which can result from the molecule internally redistributing energy or by the molecule emitting energy in the form of light is also closely examined. Exchange and redistribution of energy during a collision with other molecules can also lead to spontaneous decay. Considering decay during collisions; information is also provided about the mode linewidths which can be correlated to their spontaneous decay rates. In this section the decay rates which are a result of collisions are compared to the time it takes for a collision to occur. As chemical reactions require collisions this type of information can proof vital in future studies if one wants to manipulate chemical reactions that may depend on vibrational dynamics. The collisional time should be shorter than the spontaneous decay of a mode in order to control a chemical reaction in this way. This section is concluded by quantifying some of the fundamental constants required for simulations.

Relevant CO_2 Line Structures and Features

At room temperature molecules will be confined to their electronic ground state, as well as in their lower vibrational states. CO_2 consists of a fixed core electronic structure as well as a valence-shell of electrons which is allowed to rearrange. The electron arrangement for a CO_2 molecule when in the electronic ground state is [113],

$$\underbrace{(1\sigma_g)^2\,(1\sigma_u)^2\,(2\sigma_g)^2}_{CORE}\underbrace{(3\sigma_g)^2\,(2\sigma_u)^2\,(4\sigma_g)^2\,(3\sigma_u)^2\,(1\pi_u)^4\,(1\pi_g)^4\,(1\pi_u^*)^0\,\left(3\sigma_g^*\right)^0\,(3\sigma)^0}_{VALENCE}. \tag{4.3}$$

Equation 4.3 consists of a sequence of molecular orbitals. Lets consider $(1\sigma_g)^2$ as illustration. $(1\sigma_g)^2$ represent the sigma orbital in the first shell which is filled with two electrons. Here u indicates the orbital is unsymmetric while g indicates the orbital is symmetric under a rotation operation. For CO_2 both sigma and pi orbitals are present. The molecular orbital diagram of CO_2 illustrating equation 4.3 is also shown in Figure 4.5.

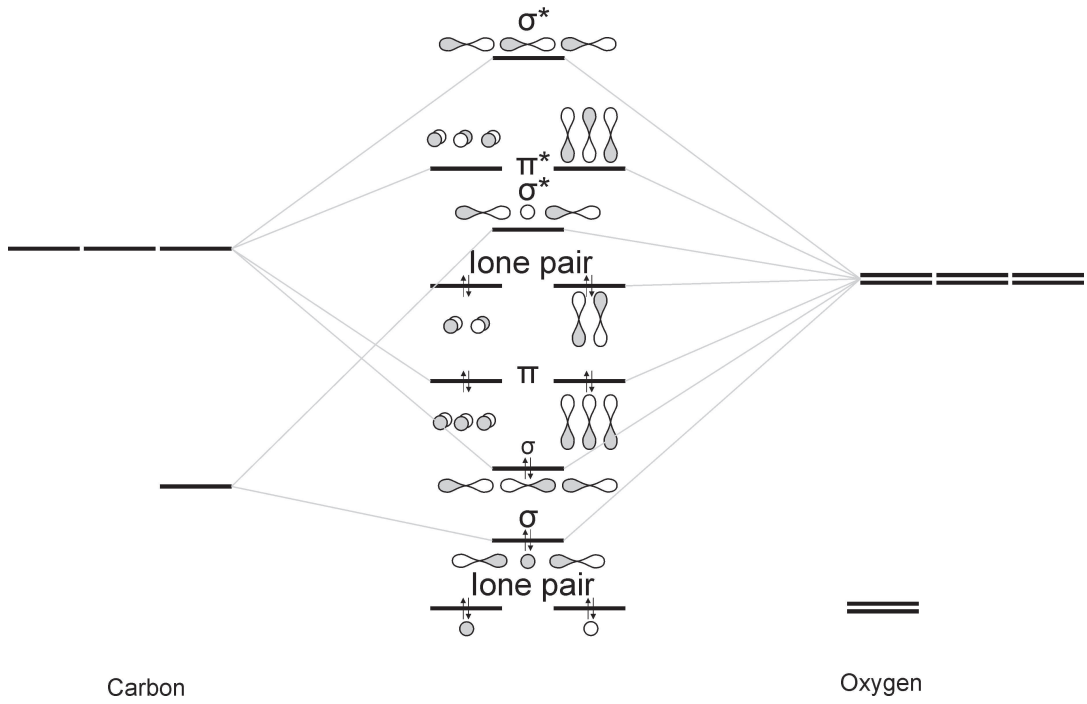

Figure 4.5: The carbon dioxide molecular orbital diagram illustrating the electron configuration of the molecule. Retrieved from [3].

If light far detuned from electronic excitations is used one may for the time being assume no light-matter interaction will lead to electronic excitation which necessitates to include these in simulations. Depending on the molecule under investigation one typically finds wavelengths in the range smaller than 2500 nm is associated with electronic excitations, 2500-25000 nm with rotational-vibrational excitations and 25000-100000 nm with purely rotational excitations. From equation 4.3 one can see the orbital $1\pi_g$ is considered as the highest occupied molecular orbital abbreviated as HOMO. In practice, several spectroscopic techniques are used to determine the lowest unoccupied orbitals which can be populated, also referred to as LUMO. The first few observable electronic excitations of CO_2 which relate to the lowest photon energies required for electronic excitation can be seen in table 4.1 [114]. From table 4.1 π^* is considered as the LUMO of CO_2.

Initial State[1]	Final State	Orbital transition	Associated photon wavelength [nm]
${}^1\sum_g^+$	${}^1\triangle_u$	$1\pi_g \rightarrow \pi^*$	148.5
${}^1\sum_g^+$	${}^1\Pi_g$	$1\pi_g \rightarrow 3s\sigma_g$	131.9
${}^1\sum_g^+$	${}^1\sum_u^+$	$1\pi_g \rightarrow 3p\pi_u$	112.2
${}^1\sum_g^+$	${}^1\Pi_u$	$1\pi_g \rightarrow 3p\sigma_u$	108.8

Table 4.1: Lowest observed electronic excitations from the ground state is shown. In the last row in the table one can see deeper laying valence electrons excited to a higher mode.

The light source energies used within this work is however of such a nature that multiple photons are required to instigate electronic transitions. For all intents and purposes it is safe to assume no electronic excitation takes place. We therefore ignore the effect of on-resonant electronic excitation.

Several studies have been focused towards establishing the polarizability of CO_2 and its related dipole moments [115]. In chemistry selection rules govern whether a transition is allowed or not. In this study transitions are separated mainly into Raman active modes and infrared active modes. For a mode to be infrared active the gross selection rule states that displacement of a normal mode should cause a change in the amplitude of the dipole moment induced by the incident radiation. The dipole moment change between two modes can be expressed as

$$I_{Raman} \propto \int \Psi_n P \Psi_m^* d\tau \tag{4.4}$$

where P is the polarizability, Ψ_n in the wave-function of the initial state and Ψ_m is the wave function of the final state. In essence it is not necessary to physically calculate the integral, but one only has to consider the symmetry of $\Psi_n P \Psi_m$. If $\Psi_n P \Psi_m$ is anti-symmetric for all possible values of P then the transition is forbidden. The transition probability between modes are therefore the product of the parity of the three components. A Raman transition from mode Ψ_n to Ψ_m is allowed if the product $\Psi_n \Psi_m$ has the same parity as one of the six components of the polarization tensor.

[1] u = unsymmetric under rotation operation, g = symmetric under rotation operation.

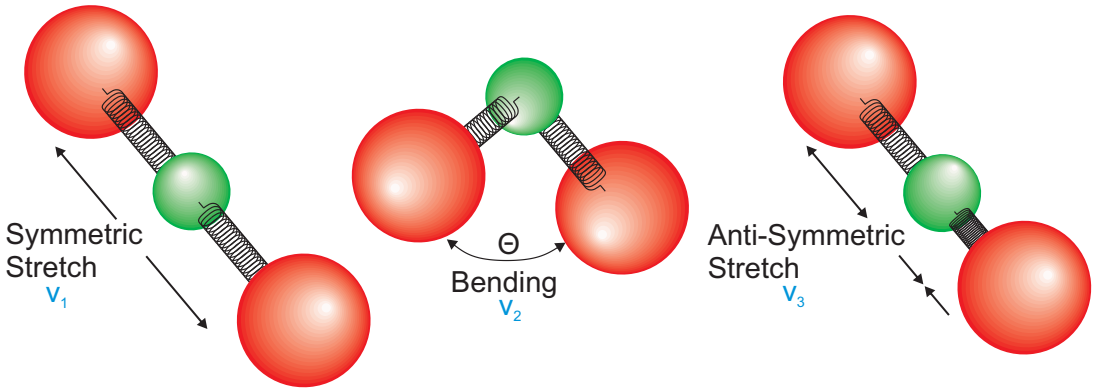

Figure 4.6: Pictorial representation of the normal vibrational modes CO_2. ν_1 is the Raman active symmetric stretch mode and ν_2 is the Raman active bend mode while ν_3 is the infrared active anti-symmetric stretch mode. The bend mode consist of an in-plane and out-of-plane bend direction. However, for the work presented here we will consider this as the same vibrational mode.

CO_2 is a $D_{\infty h}$ symmetry molecule consisting of 3 normal vibrational modes: a symmetric stretch, v_1, a bend v_2 and an anti-symmetric stretch v_3 mode, which are pictorially represented in Figure 4.6. Considering these modes one needs to establish if they are Infrared active or Raman active. Even though the dipole moment changes for each $C-O$ bond, for the symmetric stretch they are equal and opposite causing the total dipole moment to be zero. For CO_2 this implies the normal mode $v_1 = 1$ will be Raman active and the modes $v_2 = 1^1$ and $v_3 = 1$ will be infrared active. CO_2 has a center of symmetry located at the carbon atom, the exclusion rule states a centrosymmetric molecule cannot be Raman active and infrared active at the same time. Combination and overtone modes should also satisfy these conditions and care should be taken when considering if a mode is Raman or infrared active. The pulses considered for the pump and Stokes field in this work only allow certain vibrational modes to be occupied. Table 4.2 shows the CO_2 Raman active modes as well as direct infrared excitations possible for CO_2 with the sources we used [116].

$v_{\text{vacuum}}[\text{cm}^{-1}]$	$\lambda_{\text{vacuum}}[nm]$	Band type[2]	Lower state		Upper state	
			$v_1 v_2^l v_3$	Species	$v_1 v_2^l v_3$	Species
1388.3	7203	R. pol. v.s	$0, 0^0, 0$	$\sum_g^+$	$1, 0^0, 0$	$\sum_g^+$
1285	7782.1	R. pol. v.s	$0, 0^0, 0$	$\sum_g^+$	$0, 2^0, 0$	$\sum_g^+$
1305.1	7662.2	R. w.	$0, 2^0, 0$	$\sum_g^+$	$0, 4^2, 0$	$\triangle_g$
1369.4	7302.5	R.v.w	$0, 2^0, 0$	$\sum_g^+$	$1, 2^2, 0$	$\triangle_g$
11496.5	869.83	P.I || v.w.	$0, 0^0, 0$	$\sum_g^+$	$0, 0^0, 5$	$\sum_u^+$
12672.4	789.11	P.I || v.w.	$0, 0^0, 0$	$\sum_g^+$	$0, 2^0, 5$	$\sum_u^+$
12774.7	782.80	P.I || v.w.	$0, 0^0, 0$	$\sum_g^+$	$1, 2^0, 5$	$\sum_u^+$

Table 4.2: Raman and direct excitations considered for gaseous CO_2 attainable with the light sources at our disposal. The modes observed during this study is the 7203 nm stretch mode and 7782 nm bend mode.

One can not only see the normal modes, but also higher order excitations of the normal modes (overtone excitations) as well as combination bands occupied. The mode transitions $(0,0^0,0) \rightarrow (1,2^0,5)$,$(0,0^0,0) \rightarrow (0,2^0,5)$ and $(0,0^0,0) \rightarrow (0,0^0,5)$ are infrared active and can be excited directly with the pump and Stokes fields used in this study [116]. All the other modes shown are Raman active and can be excited using SRS. Several groups have measured the CARS spectra for CO_2 using different CARS setups [117]. The modes investigated in this study are the $1,0^0,0$ normal mode and the $0,2^0,0$ first overtone mode.

Inter- and Intra-molecular Vibrational Relaxation

There are two major relaxation processes for vibrational excitation. Intermolecular relaxation caused by collisions between molecules and intramolecular relaxation where no collision takes place, but relaxation and/or energy redistribution takes place due to the coupling between modes. In most cases internal energy redistribution is caused by vibration-to-rotation or vibration-to-vibration coupling [118].

The long term aim of the type of work presented in this thesis is focused on chemical reactions induced by collisions of vibrationally excited molecules. For a chemical reaction to take place one needs the assurance that the molecule stays in an prepared state until a collision takes place. Several time scales need to be taken into consideration when dealing with chemical reactions. The mean free collision time should be shorter than or of the same order of magnitude as the spontaneous decay rate caused by intramolecular energy re-distribution. If the molecules do not collide within a short time span the excited molecules will relax and distribute its vibrational energy to other degrees of freedom within the molecule itself.

Also, collisions do not necessarily imply that a chemical reaction will take place. Consider the overtone vibrational mode $0,2^0,0$. During collisions this mode might undergo a rapid vibration-vibration transition where energy is transferred to unpopulated molecules of the same species,

$$CO_2\left(0,2^0,0\right) + CO_2\left(0,0^0,0\right) \quad = \quad CO_2\left(0,1^1,0\right) + CO_2\left(0,1^1,0\right). \tag{4.5}$$

This transition will most likely lead to the $0,2^0,0$ mode decaying faster than the $1,0^0,0$ mode. Collision with larger molecules might reduce the collision time and resolve some of the issues related to this vibration-vibration energy re-distribution.

Collisional Active Reactions

Collisions play a crucial part in quantum mechanical phenomena related to chemical reactions. From a classical perspective molecules have a finite size and as a gas under normal conditions collide quite frequently. Estimating the molecular collision rate using simulations require to make some basic assumptions. To obtain an order of magnitude estimate for reasonable parameters assume molecules can be modeled as elastic spheres with some fixed radius, r. If one considers

[2] R. = Raman line, P.I. = photographic infrared band, pol. = polarised, || = parallel band (species $\sum_u^+$), $\perp$ = perpendicular band (Π_u), v.s. = very strong, v.w = very weak

one molecule to be stationary and allow the other to move then no collisions will occur unless the molecules' centers come within a distance of $2r$ from each other spanning a collisional area of $\pi (2r)^2$. The average distance traveled before a collision (or Mean Free Path) is the volume spanned divided by the number of molecules within the interactive area which can be expressed as [119],

$$\lambda = \frac{V}{\sqrt{2}N\pi (2r)^2}. \tag{4.6}$$

N is the total number of molecules measured within the interaction volume, V. From the ideal gas law we find the number of molecules within a gas sample to be $N/V = N_A P/RT$. The mean free path may now be rewritten as,

$$\lambda = \frac{RT}{\sqrt{2}\pi (2r)^2 N_A P}, \tag{4.7}$$

where $R = 8.3144$ is the gas constant, T is the ensemble temperature, $N_A = 6.022\text{x}10^{23}$ is Avogadro's number and P is the ensemble pressure. It can also be shown that the mean speed of the molecules can be obtained by,

$$\bar{v} = \sqrt{\frac{8RT}{\pi m}}, \tag{4.8}$$

where m is the reduced mass between the colliding molecules. As was mentioned, this is the case where one molecule moves and the other is stationary. If one considers the case where both are moving the average relative velocity, $\sqrt{\bar{v}_1^2 + \bar{v}_2^2} = \sqrt{2}\bar{v}$, should be used. Knowing the distance traveled by a molecule as well as its average relative velocity the mean free time between collisions can be established as [119],

$$t_{col} = \frac{\sqrt{RTm}}{32\sqrt{\pi}r^2 N_A P}. \tag{4.9}$$

Considering collisions between CO_2 molecules in a container at 21°C with a pressure of 2 atmospheric one finds a collision time of roughly 111.4 ps. It was not possible to obtain the vibrational coherent lifetimes of CO_2 in literature with which to compare the collisional time calculated. From our experimental results it is estimated that the first harmonic bend overtone lifetime as 150 ps and the symmetric stretch lifetime as 1.5 ns. One find the CO_2-CO_2 collisional time longer than the bend overtone lifetime, but shorter than the symmetric stretch lifetime. One should also take into consideration the reaction cell used during experiments. The different light fields propagate through the reaction cell, but not all the particles within the cell will be irradiated. The pump and Stokes fields also need to overlap spatially and temporally within the cell to stand a chance to undergo SRS. Furthermore, SRS is a non-linear process requiring

high pump and Stokes field energies (close to 10^{14} Watt/cm^2) to generate a strong signal. The field energy per area was increased by focusing the light into the reaction cell. This limits the number of molecules which can be excited, but nonetheless increased the CARS signal strength due to an increased field strength per unit area for the pump and Stokes fields. The molecules are also moving during SRS excitation. This however should not present any complications as a decay rate of 100 ps relate to a CO_2 molecule displaced by roughly 4 pm. In relation to the temporal width of the various fields the molecules are considered stationary.

4.4 Theoretical Description of Light-Matter Interaction

In general the theoretical treatment of light scattering from material is approached in two ways. From a purely classical point of view or by a semi-classical hybrid approach adopting a quantum mechanical treatment for the material system while keeping the classical treatment of radiation. In the quantum mechanical treatment we assume that the incident electromagnetic radiation will induce a dipole moment within the molecular ensemble which can be treated as a perturbation on the system. To describe the dynamics of molecular ensembles one starts by considering their temporal evolution during as well as after light-matter interaction. To describe the molecular system it is assumed all its properties can be described in terms of the molecular wave function $\Psi(r,t)$ which is the solution to the time-dependent Schrödinger equation [74, 120, 88],

$$i\hbar\frac{d}{dt}\left|\Psi(r,t)\right\rangle = \hat{H}\left|\Psi(r,t)\right\rangle. \tag{4.10}$$

Here $\hat{H}(t) = \hat{H}_0 - \hat{V}(t)$ is the full Hamiltonian operator consisting of the time independent unperturbed system Hamiltonian $\hat{H}_0$ and a time dependent interaction term $\hat{V}(t)$. In the absence of interactions we can describe the state of the system in terms of a complete set of eigenvectors $\psi_n(r)$ of the unperturbed Hamiltonian,

$$\left|\Psi(r,t)\right\rangle = \sum_n C_n(t)\left|\psi_n(r)\right\rangle. \tag{4.11}$$

In general this wave function include all the electronic, vibrational and rotational degrees of freedom. Only the vibrational degrees of freedom are relevant for this study and throughout this work it is assumed that the vibrational degree of freedom is decoupled from the rotational and electronic degrees of freedom. Work will be done in the so-called Schrödinger picture in which the basis functions $\psi_n(r)$ are considered time-independent (also known as stationary states). The temporal aspect of these basis functions are contained within the coefficients C_n which is seen as a probability amplitude describing the chance of a molecule to be in a particular state n at time t. Temporal evolution of the molecules can be described by the evolution of these coefficients and any final system solution can be presented as a linear combination of these functions because the basis set is complete. This includes solutions obtained when the interaction term $\hat{V}(t)$ is also

taken into consideration. Experimental systems however do not consist of single molecules but rather of molecular ensembles making it difficult if not impossible to track individual molecules experimentally. Furthermore, collisions can also occur between molecules modifying individual molecular states. For these reasons it is convenient to rather make use of the density matrix formalism to describe the ensemble of molecules in a statistical manner where the density matrix is defined as [74],

$$\rho(t) \quad = |\Psi(r,t)\rangle \langle \Psi(r,t)| = \quad \sum_{n,m} \overline{C_n^*(t) C_m(t)}. \tag{4.12}$$

This formalism considers all possible outcomes with regards to single molecules in a statistical manner and therefore provides information of the entire molecular ensemble. The subscripts n and m represent the energy levels n and m while $C_n^*(t)$ is the complex conjugate of $C_n(t)$. The diagonal elements of the density matrix ρ_{nn} represents the population of molecules in a particular state n, while the off-diagonal elements ρ_{nm} represents the coherence between the states n and m. When the system is in thermal equilibrium the off-diagonal terms are zero, while non-zero when the system is in some arbitrary superposition of energy states. Superposition can be achieved by coherent laser radiation, but not by population redistribution caused by temperature changes. These rather result in mixed states. The expectation value of any observable A is obtained by the trace of the product between the density matrix and the observable's operator $\hat{A}$,

$$\overline{\langle A \rangle} \quad = \quad tr\left(\hat{\rho}\hat{A}\right) = \sum_{nm} \rho_{nm} A_{nm}. \tag{4.13}$$

All significant information is therefore contained within the density matrix. Combining equations 4.10 and 4.12 the time evolution of the density matrix, also known as the Liouville-von Neumann equation follows [74],

$$\begin{aligned} i\hbar \frac{d}{dt}\rho(t) \quad &= \quad \left[\hat{H}, \hat{\rho}\right] \\ &= \quad \underbrace{\left[\hat{H}_0, \hat{\rho}\right]}_{stationary} + \underbrace{\left[\hat{V}, \hat{\rho}\right]}_{perturbation}. \end{aligned} \tag{4.14}$$

Each molecular state considered is treated as a stationary state of the system represented as a superposition of the basis functions which also relates to a well defined energy. This is represented by the commutator denoted *stationary* in equation 4.14. The *perturbation* commutator describes any interaction between the molecules and its surroundings. In this case it was considered that light directly interacts with matter. The interaction is considered to be that of an induced electric dipole moment caused by an external time-dependent electric field, $\hat{V}(t) = -\hat{\mu}.\tilde{E}(t)$. $\hat{\mu} = -e\hat{r}(t)$ is the electric dipole operator indicating the transition strength between levels and $E(t)$ is the applied electric field which one assumes consist of a continuous

but well defined spectrum of frequencies. Certain reactions (such as those which results from collisions or spontaneous emission) which leads to a change in the state populated cannot conveniently be added to the Hamiltonian. These are included as effective damping terms to the equation of motion 4.14 such that [74],

$$\frac{d}{dt}\rho(t) = -\frac{i}{\hbar}\left[\hat{H}_0, \hat{\rho}\right] - \frac{i}{\hbar}\left[\hat{V}, \hat{\rho}\right] - \gamma\left(\rho - \rho^{eq}\right). \tag{4.15}$$

The damping term indicates that ρ will relax to its equilibrium state ρ^{eq} at a rate γ. The effect of an applied electric field changes the way the density matrix evolves over time. To establish the new density matrix describing the ensemble, which includes light-matter interaction, one assumes that the interaction is small in strength compared to H_0 and can be treated as a perturbation. It is therefore appropriate to expand the density matrix in terms of some parameter λ which characterizes the strength of the interaction as follows: $\hat{\rho} = \hat{\rho}^{(0)} + \lambda\hat{\rho}^{(1)} + \lambda^2\hat{\rho}^{(2)} + ... + \lambda^l\hat{\rho}^{(l)}$. Following the perturbation method applied to equation 4.14 and equating terms with like powers leads to a series of equations:

$$\frac{d}{dt}\rho^{(0)} = -\frac{i}{\hbar}[\hat{H}_0, \rho^{(0)}] - \gamma\left(\rho^{(0)} - \rho^{eq}\right), \tag{4.16}$$

$$\frac{d}{dt}\rho^{(1)} = -\frac{i}{\hbar}[\hat{H}_0, \rho^{(1)}] - \frac{i}{\hbar}[\hat{V}, \rho^{(0)}] - \gamma\rho^{(1)}, \tag{4.17}$$

$$\frac{d}{dt}\rho^{(2)} = -\frac{i}{\hbar}[\hat{H}_0, \rho^{(2)}] - \frac{i}{\hbar}[\hat{V}, \rho^{(1)}] - \gamma\rho^{(2)}, \tag{4.18}$$

$$\frac{d}{dt}\rho^{(3)} = -\frac{i}{\hbar}[\hat{H}_0, \rho^{(3)}] - \frac{i}{\hbar}[\hat{V}, \rho^{(2)}] - \gamma\rho^{(3)}, \tag{4.19}$$

with the l^{th} order perturbation expressed as

$$\frac{d}{dt}\rho^{(l)} = -\frac{i}{\hbar}[\hat{H}_0, \rho^{(l)}] - \frac{i}{\hbar}[\hat{V}, \rho^{(l-1)}] - \gamma\rho^{(l)}. \tag{4.20}$$

What one observes is that each perturbation order depends on the previous applied perturbation. Starting with the unperturbed system it is possible to systematically correct the density matrix up to the desired order. During light-matter interactions several processes can occur, this study is only interested in SRS and CARS. Therefore it limits the quantum mechanical system to four known levels since it only considers laser frequencies which might interact resonantly with these. An energy diagram for the levels can be seen in Figure 4.7 showing the ground state Ψ_g, an intermediate electronic excited state Ψ_i and two vibrational states Ψ_{v_1} and Ψ_{v_2}, respectively.

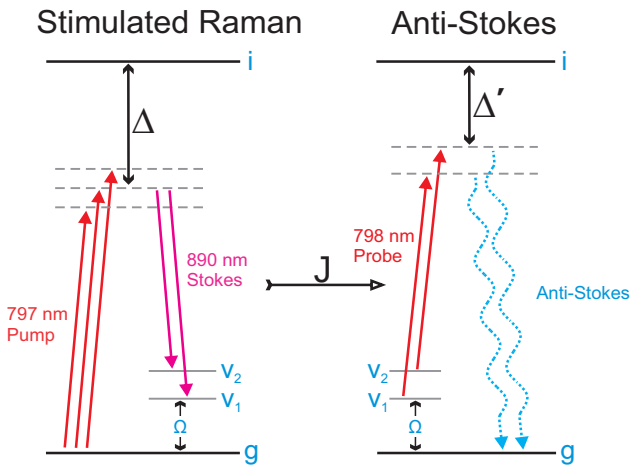

Figure 4.7: The energy diagram for SRS and CARS are shown. g, i, v_1 and v_2 are the four energy levels considered. The intermediate level i is such that incident light is far detuned from electronic resonances with $\triangle$ and $\triangle'$ the respective detunings.

The density matrix for the l^{th} order perturbation for these four-level molecules is,

$$\rho^{(l)} = \begin{bmatrix} \rho_{gg}^{(l)} & \rho_{gi}^{(l)} & \rho_{gv_1}^{(l)} & \rho_{gv_2}^{(l)} \\ \rho_{ig}^{(l)} & \rho_{ii}^{(l)} & \rho_{iv_1}^{(l)} & \rho_{iv_2}^{(l)} \\ \rho_{v_1g}^{(l)} & \rho_{v_1i}^{(l)} & \rho_{v_1v_1}^{(l)} & \rho_{v_1v_2}^{(l)} \\ \rho_{v_2g}^{(l)} & \rho_{v_2i}^{(l)} & \rho_{v_2v_1}^{(l)} & \rho_{v_2v_2}^{(l)} \end{bmatrix}. \tag{4.21}$$

The unperturbed Hamiltonian represents the energy of each of the modes considered,

$$H_0 = \begin{bmatrix} \hbar\omega_g & 0 & 0 & 0 \\ 0 & \hbar\omega_i & 0 & 0 \\ 0 & 0 & \hbar\omega_{v_1} & 0 \\ 0 & 0 & 0 & \hbar\omega_{v_2} \end{bmatrix}, \tag{4.22}$$

while the interaction Hamiltonian is expressed as

$$\hat{V}(t) = -\begin{bmatrix} 0 & \mu_{gi}E(t) & \mu_{gv_1}E(t) & \mu_{gv_2}E(t) \\ \mu_{ig}E(t) & 0 & \mu_{iv_1}E(t) & \mu_{iv_2}E(t) \\ \mu_{v_1g}E(t) & \mu_{v_1i}E(t) & 0 & 0 \\ \mu_{v_2g}E(t) & \mu_{v_2i}E(t) & 0 & 0 \end{bmatrix}. \tag{4.23}$$

μ_{ig} Is the electric dipole moment between states i and g which is the conjugate of the dipole moment μ_{gi}. The electric field $E(t)$ considered is the total electric field consisting of the pump, Stokes and probe fields combined and described as indicated by equation 2.2 and

2.3. Transitions between modes are under scrutiny of selection rules and not all transitions between modes are allowed. One of the requirements allowing a transition between vibrational modes is that momentum should be transferred from the nuclear motion to electronic motion while conserving the total momentum of the molecule. For a symmetric molecule one finds that a direct transition between two normal vibrational modes will in most cases not conserve the the total molecular momentum. A direct transition between the normal vibrational modes of CO_2 is therefore considered as a forbidden transition such that $\mu_{v_2v_1} = \mu_{v_2v_1} = 0$. Exciting a molecule from its ground electronic and vibrational mode to higher vibrational modes while still in the electronic ground state sometimes lead to the conservation of momentum as in the case for infrared active modes of CO_2. For the time being it allows infrared active modes which will be eliminated at some later stage. There is also no electric dipole moment between a mode and itself such that $\mu_{gg} = \mu_{ii} = \mu_{v_1v_1} = \mu_{v_2v_2} = 0$. The *stationary* commutator, $[\hat{H}_0, \rho^{(l)}]$, can now be generalized into the form

$$[\hat{H}_0, \rho^{(l)}]_{nm} = (E_n - E_m)\,\rho_{nm} \tag{4.24}$$

for each of the matrix elements. To simplify things one also substitutes $(E_n - E_m)/\hbar$ with ω_{nm}. Unfortunately the *perturbation* commutators,$[\hat{V}, \rho^{(l-1)}]$ do not simplify so elegantly and is explicitly represented by

$$\left[\hat{V}(t), \hat{\rho}^{(l)}\right]_{nm} = \sum_r \left(\mu_{nr}\rho^{(l)}_{rm} - \rho^{(l)}_{nr}\mu_{rm}\right)\tilde{E}(t)\,. \tag{4.25}$$

For the 4-level system one assumes r can either be g, i, v_1 or v_2 . Using the relations in Appendix A.1.2 for solving first order differential equations, the equation of motion can be expressed as

$$\rho^{(l)}_{nm}(t) = \frac{-i}{\hbar}e^{-t(i\omega_{nm}+\gamma_{nm})}\int_{-\infty}^{t} e^{t'(i\omega_{nm}+\gamma_{nm})}[\hat{V}, \rho^{(l-1)}]_{nm}dt'. \tag{4.26}$$

If one expresses the applied fields in the form of equation 2.2 and substitute equation 4.25 for the *perturbation* commutator then the density matrix elements can be represented as

$$\rho^{(l)}_{nm} = \frac{-i}{\hbar}e^{-t(i\omega_{nm}+\gamma_{nm})}\int_{-\infty}^{\infty}\int_{-\infty}^{t} E(\omega)\,e^{-t'(i\omega-i\omega_{nm}-\gamma_{nm})}\sum_r\left(\mu_{nr}\rho^{(l-1)}_{rm} - \rho^{(l-1)}_{nr}\mu_{rm}\right)dt'd\omega. \tag{4.27}$$

This form of the density matrix elements allow linear light-matter interactions for the pump, Stokes and probe fields as the frequency integration is considered over the complete domain. One should also take into consideration that the damping terms are not the same for on and off-

diagonal elements as was explained previously. Initially the ensemble is in thermal equilibrium such that the density matrix for the unperturbed system is

$$\rho^{(0)} = \begin{bmatrix} \rho_{gg}^{(0)} & 0 & 0 & 0 \\ 0 & \rho_{ii}^{(0)} & 0 & 0 \\ 0 & 0 & \rho_{v_1v_1}^{(0)} & 0 \\ 0 & 0 & 0 & \rho_{v_2v_2}^{(0)} \end{bmatrix}. \tag{4.28}$$

Furthermore, one considers room temperatures such than $k_bT \ll E_v$, for Boltzmann's constant k_b, which results in $\rho_{v_1v_1}^{(0)} \ll \rho_{gg}^{(0)}$ and $\rho_{v_2v_2}^{(0)} \ll \rho_{gg}^{(0)}$. It is also assumed the relative applied fields are far detuned from electronic excitations making $\rho_{ii}^{(0)} \approx 0$ a fairly good approximation for all times. Henceforth, it is assumed most molecules are initially in the ground electronic and vibrational state.

CARS generates signals which are directional as well as coherent. According to Maxwell's equations [79],

$$-\nabla^2\tilde{E} + \frac{1}{c^2}\frac{\partial^2\tilde{E}}{\partial t^2} = -\frac{4\pi}{c^2}\frac{\partial^2\tilde{P}}{\partial t^2}. \tag{4.29}$$

Light can be absorbed by the material leading to a change in its macroscopic polarization, $\tilde{P}$, which in turn can emit light restoring the materials polarization to its original state. For a molecular ensemble the polarization can be expressed as $\tilde{P} = N\langle\mu\rangle$ where N indicate the number of molecules considered while the dipole operator, $\langle\mu\rangle$, is obtained using equation 4.13. For strong fields higher order polarization terms emerge such that one can express the polarization as a series of terms, $P(t) = P^0(t) + P^1(t) + P^2(t) + ... + P^l(t)$ which is treated as polarization perturbations. Each and every term represents some phenomenological effect observed during light matter interaction. During CARS $P^0(t)$ is considered as the natural polarization state of the molecules, $P^1(t)$ relates to the spontaneous Raman scattering, $P^2(t)$ relates to SRS while $P^3(t)$ leads to CARS. Intermolecular interactions can complicate the quantum mechanical analysis significantly. The theory derived here are based on a microscopic approach in which the scattering from a individual molecule is considered. The main limitation of this approach is that spatial coherence between molecules is neglected, and consequently directional stimulated CARS will not be considered. Nonetheless the restricted model is very successful in describing the time-resolved dynamics of the vibrational excitation processes and it predicts the Anti-Stokes signals to what is observed in the laboratory. The perturbed higher order density matrix will now be determined for SRS.

4.4.1 Stimulated Raman Scattering

Light-matter interaction which leads to coherent vibrational excitation can occur via direct infrared (IR) excitation or through Stimulated Raman Scattering (SRS). The fields used in this work are too far detuned for IR excitations to occur which leads one to only consider SRS. The

probability that SRS will occur is the highest when manipulating the motion of the molecule on a timescale similar to its natural vibrational timescales. SRS require two fields with the difference in energy corresponding to a vibrational excitation. Perturbation to the 1^{st} order will allow one to observe Spontaneous Raman Scattering while perturbation up to the 2^{nd} order will allow Stimulated Raman Scattering (SRS). During SRS temporal overlap between the fields lead to SRS occurring instantaneously without occupation of any intermediate states and consequently interaction time shorter than the vibrational response time of the molecules. Energy is therefore coherently deposited into the molecules. For 1^{st} order perturbation $l = 1$ in equation 4.27 which is analytically solved as

$$\rho_{nm}^{(1)} = \frac{\mu_{nm}}{\hbar}\left(\rho_{mm}^{(0)} - \rho_{nn}^{(0)}\right)\int_{-\infty}^{\infty}\frac{E(\omega)\,e^{-i\omega t}}{(\omega_{nm}-\omega)-i\gamma_{nm}}d\omega \tag{4.30}$$

for each of the density matrix elements. When taking a closer look at equation 4.30 one can immediately conclude that $\rho_{gg}^{(1)}(t) = \rho_{ii}^{(1)}(t) = \rho_{v_1v_1}^{(1)}(t) = \rho_{v_2v_2}^{(1)}(t) = 0$ since $\rho_{mm}^{(0)} - \rho_{mm}^{(0)} = 0$ for all values of m. There is no coupling between the two vibrational levels such that $\mu_{v_2v_1} = \mu_{v_1v_2} = 0$. Direct transition from ground vibrational states to the vibrational states are forbidden due to a change in momentum such that $\mu_{gv_1} = \mu_{gv_2} = 0$. Furthermore, if one assumes the initial population of higher order modes is zero, $\rho_{ii}^{(1)}(t) = \rho_{v_1v_1}^{(1)}(t) = \rho_{v_2v_2}^{(1)}(t) = 0$, it follows from equation 4.30 that $\rho_{iv_1}^{(1)}(t) = \rho_{iv_2}^{(1)}(t) = 0$. The first order density matrix consists of non-zero values according to

$$\rho^{(1)} = \begin{bmatrix} 0 & \rho_{gi}^{(1)}(t) & 0 & 0 \\ \rho_{ig}^{(1)}(t) & 0 & 0 & 0 \\ 0 & 0 & 0 & 0 \\ 0 & 0 & 0 & 0 \end{bmatrix}. \tag{4.31}$$

The non-zero relation for the off-diagonal elements suggest coherence between the states which indicates the possibility of populating the energy levels associated with state transfer. 2^{nd} Order perturbation will now populate the molecular vibrational modes. For 2^{nd} order perturbation $l = 2$ in equation 4.27 which gives

$$\rho_{nm}^{(2)} = \frac{-i}{\hbar}e^{-t(i\omega_{nm}+\gamma_{nm})}\int_{-\infty}^{\infty}\int_{-\infty}^{t}E(\omega')\,e^{-t'\left(i\omega'-i\omega_{nm}-\gamma_{nm}\right)}\sum_{r}\left(\mu_{nr}\rho_{rm}^{(1)} - \rho_{nr}^{(1)}\mu_{rm}\right)dt'd\omega'. \tag{4.32}$$

The expressions obtained for the first order density matrix, equation 4.30, is now inserted into equation 4.32 and the integration over time is performed to obtain

$$\rho_{nm}^{(2)} = \sum_r \frac{\mu_{nr}\mu_{rm}\left(\rho_{mm}^{(0)}-\rho_{rr}^{(0)}\right)}{\hbar^2}\int_{-\infty}^{\infty}\int_{-\infty}^{\infty}\frac{E(\omega)E(\omega')e^{-it(\omega+\omega')}}{(\omega_{nm}-\omega-\omega'-i\gamma_{nm})(\omega_{rm}-\omega-i\gamma_{rm})}d\omega d\omega' - \sum_r \frac{\mu_{nr}\mu_{rm}\left(\rho_{rr}^{(0)}-\rho_{nn}^{(0)}\right)}{\hbar^2}\int_{-\infty}^{\infty}\int_{-\infty}^{\infty}\frac{E(\omega)E(\omega')e^{-it(\omega+\omega')}}{(\omega_{nm}-\omega-\omega'-i\gamma_{nm})(\omega_{nr}-\omega-i\gamma_{nr})}d\omega d\omega', \tag{4.33}$$

For the time being focus is on the stretch vibrational mode. If $n = v_1$ and $m = g$ then the density matrix element, $\rho_{nm}^{(2)}$, corresponds to coherence between the ground and first vibrational mode. In equation 4.33 r can be any energy level of the molecule. Fortunately most of these terms do not contribute (or are negligible relative to on resonant transitions) to the coherence between the ground and first vibrational mode. From what was discussed previously $\mu_{v_1v_2} = \mu_{v_1v_1} = \mu_{gg} = 0$, while $\rho_{v_1v_2}^{(1)} = \rho_{v_1v_1}^{(1)} = \rho_{gg}^{(1)} = 0$ were calculated, such that

$$\rho_{v_1g}^{(2)} = \frac{\left(\rho_{gg}^{(0)}-\rho_{ii}^{(0)}\right)\mu_{v_1i}\mu_{ig}}{\hbar^2}\int_{-\infty}^{\infty}\int_{-\infty}^{\infty}\frac{E(\omega)E(\omega')e^{-it(\omega+\omega')}}{(\omega_{v_1g}-\omega-\omega'-i\gamma_{v_1g})(\omega_{ig}-\omega-i\gamma_{ig})}d\omega d\omega' - \frac{\left(\rho_{ii}^{(0)}-\rho_{v_1v_1}^{(0)}\right)\mu_{v_1i}\mu_{ig}}{\hbar^2}\int_{-\infty}^{\infty}\int_{-\infty}^{\infty}\frac{E(\omega)E(\omega')e^{-it(\omega+\omega')}}{(\omega_{v_1g}-\omega-\omega'-i\gamma_{v_1g})(\omega_{v_1i}-\omega-i\gamma_{v_1i})}d\omega d\omega' \tag{4.34}$$

Equation 4.34 is quite a complex expressions obtained for the coherence, but which can be simplified using the initial state populations. If $\rho_{ii}^{(0)}$ is considered zero in the initial population and from Boltzmann we have once again $\rho_{v_1v_1}^{(0)} \ll \rho_{gg}^{(0)}$ and $\rho_{v_2v_2}^{(0)} \ll \rho_{gg}^{(0)}$ such that the initial vibrational populations can be neglected. The terms contributing the most are those whose denominator will approach a minimum. For the coherence $\rho_{v_1g}^{(2)}$ to be a maximum one requires $\omega_{v_1g} = \omega - \omega'$. This is the condition for SRS which is also the first step towards generating a CARS signal. Separating the positive and negative frequency domains the main resonant term which contribute to SRS is found as

$$\rho_{v_1g}^{(2)} = \frac{\mu_{v_1i}\mu_{ig}\rho_{gg}^{(0)}}{\hbar^2}\int_{0}^{\infty}\int_{0}^{\infty}\frac{E_p(\omega)E_s^*(\omega')e^{-it(\omega-\omega')}}{(\omega_{v_1g}-\omega+\omega'-i\gamma_{v_1g})(\omega_{ig}-\omega-i\gamma_{ig})}d\omega d\omega'. \tag{4.35}$$

Even though the other terms do contribute to coherence they are negligible relative to the effects of on-resonant SRS. Note that the interaction is suppressed by a factor dependent on the detuning from the intermediate energy level, namely $\Delta_{ig} = \omega_{ig} - \omega$. Fortunately, the light sources used in this study exhibit qualities such that $\omega \ll \omega_{ig}$ and therefore one considers $\Delta_{ig} \sim \omega_{ig}$. The off-resonant scattering rate γ_{ig} is neglected since it depends inverse quadratically on this

detuning and is therefore far off-resonance. To elucidate the underlying physics, let's substitute ω' with $\omega - \Omega$ and simplify to obtain,

$$\rho^{(2)}_{v_1 g}(t) = \frac{\mu_{v_1 i}\mu_{ig}}{\hbar^2}\frac{\rho^{(0)}_{gg}}{\triangle_{ig}}\int_0^\infty \frac{e^{-it\Omega}}{(\omega_{v_1 g} - \Omega - i\gamma_{v_1 g})}\int_0^\infty E_p(\omega)E_s^*(\omega - \Omega)d\omega d\Omega. \tag{4.36}$$

Equation 4.36 is now expressed in a more compressed form as

$$\rho^{(2)}_{v_1 g}(t) = \int_0^\infty \left(\frac{C_{v_1 g}A(\Omega)}{\omega_{v_1 g} - \Omega - i\gamma_{v_1 g}}\right) e^{-it\Omega}d\Omega \tag{4.37}$$

with $C_{v_1 g} = \frac{\mu_{v_1 i}\mu_{ig}}{\hbar^2}\left(\frac{\rho^{(0)}_{gg}}{\triangle_{ig}}\right)$ the off-resonant coupling strength while

$$A(\Omega) = \int_0^\infty E_p(\omega)E_s^*(\omega - \Omega)d\omega. \tag{4.38}$$

Equation 4.38 is the convolution between the spectral representation of the pump and Stokes fields which by the convolution theorem is equal to the Fourier transform of the product of the pump and Stokes fields in time,

$$A(\Omega) = \mathcal{F}\left[E_p(t).E_s^*(t)\right]. \tag{4.39}$$

Matlab is more efficient in determining fast Fourier transforms than convolutions. To reduce computational time during simulations the inverse Fourier transform of the time domain is rather used than the convolution when determining $A(\Omega)$. Note that equation 4.37 is simply the frequency domain representation of the density matrix element, i.e.

$$\rho^{(2)}_{v_1 g}(\Omega) = \frac{C_{v_1 g}A(\Omega)}{(\omega_{v_1 g} - \Omega - i\gamma_{v_1 g})}. \tag{4.40}$$

The following shows all density matrix elements having non-zero contributions to second order in our perturbation expansion:

$$\rho^{(2)} = \begin{bmatrix} \rho^{(2)}_{gg}(t) & \rho^{(2)}_{gi}(t) & \rho^{(2)}_{gv_1}(t) & \rho^{(2)}_{gv_2}(t) \\ \rho^{(2)}_{ig}(t) & 0 & \rho^{(2)}_{iv_1}(t) & \rho^{(2)}_{iv_2}(t) \\ \rho^{(2)}_{v_1 g}(t) & \rho^{(2)}_{v_1 i}(t) & \rho^{(2)}_{v_1 v_1}(t) & 0 \\ \rho^{(2)}_{v_2 g}(t) & \rho^{(2)}_{v_2 i}(t) & 0 & \rho^{(2)}_{v_2 v_2}(t) \end{bmatrix}. \tag{4.41}$$

It is clear in this case that the diagonal elements representing mode population are not zero

anymore.

4.4.2 Coherent Anti-Stokes Raman Scattering (CARS)

The CARS signal is generated spontaneously and is a consequence of the 3^{rd} order polarization between the intermediate energy level and ground energy level generated by the probe field. For the scenario stipulated for CARS one would only be interested in the polarization terms caused by the probe field which is signified by 3^{rd} order perturbation on the density matrix. Neglecting terms not meeting this requirement lead to [120],

$$\langle \mu \rangle = \mu_{gi}\rho_{ig}^{(3)} + \mu_{ig}\rho_{gi}^{(3)}. \tag{4.42}$$

Since the diagonal elements of the dipole operator are zero ($\mu_{nn} = 0$), the polarization is independent of ρ_{nn} and depend only on the off-diagonal elements of the density matrix, $\hat{\rho}$. The density matrix element for $l = 3$ from the ground state to the 1^{st} vibrational state are given by

$$\rho_{ig}^{(3)}(t) = \frac{-i}{\hbar} e^{-t(i\omega_{ig}+\gamma_{ig})} \int_{-\infty}^{\infty}\int_{-\infty}^{t} E(\omega'') e^{-it'(\omega''-\omega_{ig})} \sum_{r} \left(\mu_{ir}\rho_{rg}^{(2)} - \rho_{ir}^{(2)}\mu_{rg}\right) dt' d\omega''. \tag{4.43}$$

The *perturbation* commutator between the vibrational state and ground state is expressed as

$$\begin{aligned}\sum_{r} \left(\mu_{ir}\rho_{rg}^{(2)} - \rho_{ir}^{(2)}\mu_{rg}\right) = {} & \mu_{ig}\rho_{gg}^{(2)} - \rho_{ig}^{(2)}\mu_{gg} \\ & + \mu_{ii}\rho_{ig}^{(2)} - \rho_{ii}^{(2)}\mu_{ig} \\ & + \mu_{iv_1}\rho_{v_1g}^{(2)} - \rho_{iv_1}^{(2)}\mu_{v_1g} \\ & + \mu_{iv_2}\rho_{v_2g}^{(2)} - \rho_{iv_2}^{(2)}\mu_{v_2g}.\end{aligned} \tag{4.44}$$

Similar as before $\mu_{gg} = \mu_{ii} = 0$. Infrared active modes are far-detuned from the light fields one use such that $\mu_{v_1g} = \mu_{v_2g} = 0$ while $\rho_{ii}^{(2)} = 0$ was calculated in the previous section. All these terms are therefore omitted from equation 4.44 to express $\rho_{ig}^{(3)}$ as

$$\rho_{ig}^{(3)}(t) = \frac{-i}{\hbar} e^{-t(i\omega_{ig}+\gamma_{ig})} \int_{-\infty}^{\infty}\int_{-\infty}^{t} E(\omega'') e^{-it'(\omega''-\omega_{ig})} \left(\mu_{iv_1}\rho_{v_1g}^{(2)} + \mu_{iv_2}\rho_{v_2g}^{(2)}\right) dt' d\omega''. \tag{4.45}$$

When substituting equation 4.40 for $\rho_{v_1g}^{(2)}$ and a similar expression for $\rho_{v_2g}^{(2)}$ while integrating

over time one finds,

$$\begin{aligned}\rho_{ig}^{(3)}(t) &= \int_{-\infty}^{\infty}\int_{0}^{\infty}\frac{C'_{v_1g}A(\Omega)E(\omega'')e^{-i(\omega''+\Omega)t}}{(\omega_{v_1g}-\Omega-i\gamma_{v_1g})(\omega_{ig}-\Omega-\omega''-i\gamma_{ig})}d\Omega d\omega'' \\ &+\int_{-\infty}^{\infty}\int_{0}^{\infty}\frac{C'_{v_2g}A(\Omega)E(\omega'')e^{-i(\omega''+\Omega)t}}{(\omega_{v_2g}-\Omega-i\gamma_{v_2g})(\omega_{ig}-\Omega-\omega''-i\gamma_{ig})}d\Omega d\omega'' \qquad (4.46)\end{aligned}$$

where $C'_{v_1g}=\mu_{iv_1}C_{v_1g}/\hbar$ and $C'_{v_2g}=\mu_{iv_2}C_{v_2g}/\hbar$. With the broadband laser sources used in this work both vibrational modes will be occupied. A probe field will however not favor one mode over the other and both modes will be measured simultaneously. Based on equation 4.46 one now defines a CARS response function,

$$R(\Omega) = A(\Omega)\underbrace{\sum_{j=1,2}\frac{C'_{v_jg}}{(\omega_{v_jg}-\Omega-i\gamma_{v_jg})}}_{Line-profile}. \qquad (4.47)$$

The probe field is chosen far off-resonance with any electronic intermediate state such that $\omega_{v_jg}+\omega''\ll\omega_{ig}$. Furthermore, the detuning $\omega_{ig}-\Omega-\omega''$ is much larger than the damping term $i\gamma_{ig}$ so the damping is neglected. The electric field in equation 4.46 is considered as the probe field which will be discussed in section 4.4.3. In equation 4.46 over the complete frequency domain, ω'', is integrated. The negative frequencies are however far off resonant from any electronic state and will only result in small contributes towards the integration. Therefore, term $\omega_{ig}-\Omega-\omega''-'i\gamma_{ig}$ is also treated as a non-resonant excitation and replaced by the factor $\triangle'$. The density matrix element $\rho_{ig}^{(3)}$ can then be written into an explicit form (in the time domain) as,

$$\begin{aligned}\rho_{ig}^{(3)}(t) &= \frac{1}{\triangle'}\int_{0}^{\infty}\int_{0}^{\infty}R(\Omega)E(\omega'')e^{-i(\omega''+\Omega)t'}d\omega''d\Omega \\ &= \frac{1}{\triangle'}\int_{0}^{\infty}R(\Omega)e^{-i\Omega t'}d\Omega\int_{0}^{\infty}E(\omega'')e^{-i\omega''t'}d\omega'' \qquad (4.48)\end{aligned}$$

Alternatively, one can express the right-hand-side of equation 4.48 in the time domain as

$$\rho_{ig}^{(3)}(t) = \frac{1}{\triangle'}R(t)E(t) \qquad (4.49)$$

where $R(t)=F^{-1}(R(\Omega))$. As mentioned earlier the CARS signal is proportional to the induced polarization. Therefore the anti-Stokes electric field has the form

$$E_{as}(t) \quad \propto \quad \frac{1}{\triangle'} R(t) E_{pr}(t), \tag{4.50}$$

Making use of the convolution theorem the anti-Stokes field can also be expressed in the frequency domain as the convolution between the response function,$R(\Omega)$, and the probe field, $E_{pr}(\omega)$ such that,

$$E_{as}(\omega) \quad \propto \quad \int_0^\infty E_{pr}(\omega - \Omega) R(\Omega) \, d\Omega. \tag{4.51}$$

Spectrometers measure the field intensity and cannot provide any phase information. The CARS signal intensity which will be measured during experiments is therefore

$$I_{as}(\omega) \quad = \quad E_{as}(\omega) E_{as}^{*}(\omega) \tag{4.52}$$

The dependence of the CARS signal on the probe field will be dealt with in section 4.4.4.

4.4.3 Non-Resonant Background and CARS

For CARS to be a successful spectroscopic technique one requires background noise due to other processes to be a minimum. The two main contributing categories identified are: The vibrational coherence do not only consist of resonant terms and secondly other four-wave mixing processes also radiate light at the anti-Stokes signal frequencies. In Figure 4.8 the pathways for some of these processes are shown.

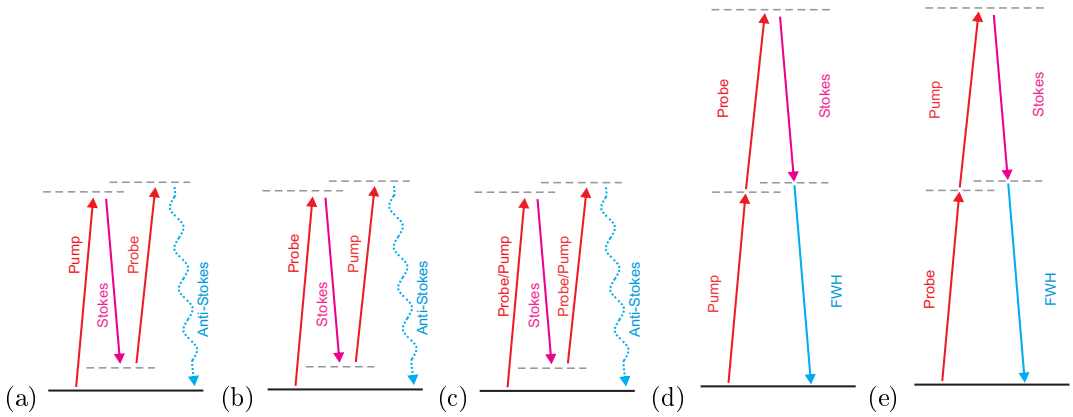

Figure 4.8: This Figure shows some of the processes which can occur with the fields used in this work. (a) Will generate the CARS signal one is looking for. The pathways in (b) and (c) prepare vibrational coherence which leads to CARS due to the similarities between the pump and Stokes fields. These are however not the CARS signal one is looking for and will be considered as background noise. Path (d) and (e) are four-wave mixing pathways which will not prepare vibrational coherence but still radiates at the anti-Stokes frequencies.

A requirement for these background processes to occur is that the pump, Stokes and probe fields should overlap in time to create transient coherence. The time domain response $C_{NR}(t)$ for the different non-resonant pathways are all governed by

$$C_{NR}(t) \quad \propto \quad E_p(t)\, E_s(t)\, E_{pr}(t)\,. \tag{4.53}$$

Because the optical fields are real it contains both positive and negative frequencies such that $C_{NR}(t)$ will consist of carrier frequencies like $\omega_{pr} + \omega_s - \omega_p$ which will generate a signal at the anti-Stokes frequencies. Several ways have been shown capable of resolving the CARS signal afterwards. However, in this work the background is rather suppressed using polarization techniques as well as considering temporal overlap between the fields where one delays the probe field with regards to the pump field to ensure the pump and probe fields do not interchange their functionalities. Equation 4.52 was obtained by neglecting non-resonant terms which do not reflect SRS.

4.4.4 Time-resolved CARS

TR-CARS can be used to monitor the evolution of a molecular wave-packet. Each peak within the anti-Stokes signal represents an excited mode. Therefore, important information about the temporal response for an excited mode can be extracted when delaying the probe pulse relative to the pump and Stokes pulses. Figure 4.9 illustrates the behaviour of the molecules considering their modes during a vibrational CARS process. During multiplex CARS, SRS prepares a Raman wave-packet from position 1 to position 2. The molecules are now allowed to evolve for some time. The anti-Stokes signal is generated when a probe field de-excites the molecules from

position 3 to position 4 in figure 4.9. A different molecular response will be observed depending on the the timing of the probe field.

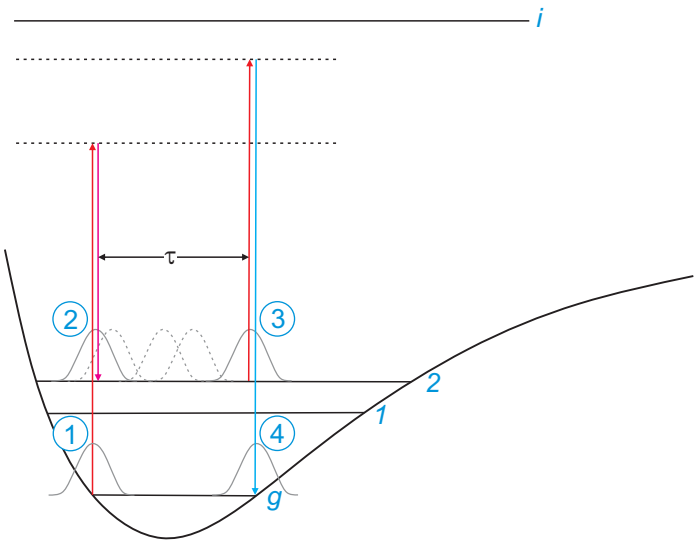

Figure 4.9: Illustration of TR-CARS. At 1 the molecules undergoes SRS exciting the molecules to higher vibrational excitations ending at 2. The molecules are now allowed to evolve over time. At 3 the probe field de-excite the molecules to 4 emitting an anti-Stokes photon.

The CARS spectra collected at different delay times oscillate at a frequency which corresponds to the energy difference between the vibrational modes. In literature this phenomenon is also referred to as polarization beating. During frequency CARS spectral measurements it might occur that the signals for some modes are too low to observe and disappears within the background noise. A Fourier transform on a TR-CARS spectrograph will highlight the frequencies involved and consequently also the modes currently occupied. This method provides an alternative approach to measuring signals too low to measure directly using frequency CARS.

If one would like to simulate the beating one might ask what mechanism leads to the beating. In order to answer this question one needs to go back to equation 4.37 and take a few things into consideration. Firstly, one should not substitute ω' with $\omega - \Omega$ while also assuming the pump and Stokes fields are narrowband sources approximated as delta functions. One now considers only two frequencies at ω_{p_1} and ω_{p_2} for the pump field which will match up with ω_s leading to on-resonant excitation due to energy conservation. Equation 4.37 now becomes

$$\rho^{(2)}_{v_1 g}(t) = \int_0^\infty \int_0^\infty \frac{C_{v_1 g} e^{-it(\omega-\omega')} E(\omega) \left(\delta(\omega-\omega_{p_1}) + \delta(\omega-\omega_{p_2})\right) E(\omega') \delta(\omega'-\omega_s)}{\omega_{v_1 g} + \omega' - \omega - i\gamma_{v_1 g}} d\omega d\omega'. \tag{4.54}$$

Written out and simplified, this reduces to

$$\rho^{(2)}_{v_1 g}(t) = \frac{C_{v_1 g} e^{-it(\omega_{p_1}-\omega_s)}}{\omega_{v_1 g} - (\omega_{p_1}-\omega_s) - i\gamma_{v_1 g}} + \frac{C_{v_1 g} e^{-it(\omega_{p_2}-\omega_s)}}{\omega_{v_1 g} - (\omega_{p_2}-\omega_s) - i\gamma_{v_1 g}}. \tag{4.55}$$

The main contributing part in equation 4.55 is the first term because one is on-resonant $\omega_{v_1 g} - (\omega_{p_1} - \omega_s) = 0$ with the stretch vibrational mode. Similarly can be obtained for the density matrix element related to the bend mode. One should also consider a phase shift of θ at the frequency ω_{p_2}. The response function equation 4.47 for the considerations above now simplifies to

$$R(t) = -\frac{C_{v_1 g} e^{-it(\omega_{p_1}-\omega_s)}}{i\gamma_{v_1 g}} - \frac{C_{v_2 g} e^{-it(\omega_{p_2}-\omega_s+\theta)}}{i\gamma_{v_2 g}}. \tag{4.56}$$

If one assumes $\gamma_{v_1 g} = \gamma_{v_2 g}$ and $C_{v_1 g} = C_{v_2 g}$ for the time being we find

$$R(t) = -\frac{C_{v_1}}{i\gamma_{v_1 g}} \quad e^{it\omega_s}\left(e^{-it\omega_{p_1}} + e^{-it\omega_{p_2}} e^{+i\theta}\right). \tag{4.57}$$

The intensity is however related to the coherence as

$$I \propto |R(t)|^2. \tag{4.58}$$

Using trigonometric identities it can be shown that

$$\begin{aligned} |R(t)|^2 &= -\frac{4C^2_{v_1}}{\gamma^2_{v_1 g}} e^{i2t\omega_s}\left(\cos\left(\frac{t\omega_{p_2} - t\omega_{p_1} + \theta}{2}\right) e^{-i\left(\frac{t\omega_{p_2}+t\omega_{p_1}-\theta}{2}\right)}\right)^2 \\ &\propto 1 - \cos\left(t\omega_{p_2} - t\omega_{p_1} + \theta\right) \end{aligned} \tag{4.59}$$

which reflects the beating observed. Furthermore the phase term,θ, related to frequency ω_{p_2} can be changed which will change the position in time the beating is created. According to table 4.2 several ground-vibrational coherences and beating frequencies between various vibrations can be induced forCO_2 with the sources used in this study as shown in table 4.3. In table 4.3 v_1 is the symmetric stretch mode, v_2 is the overtone bend mode, v_3 is the $(0, 4^2, 0)$ mode while v_4 is the $(1; 2^2; 0)$ mode which are all Raman active.

As example of TR-CARS Fig. 4.10 shows in (a) a simulated TR-CARS spectrograph and in (b) an experimentally obtained spectrograph for CO_2.

THz		v_1	v_2	v_3	v_4
		41.64	38.55	39.15	41.08
v_1	41.64	none	3.09	2.49	0.56
v_2	38.55	3.09	none	0.60	2.53
v_3	39.15	2.49	0.6	none	1.93
v_4	41.08	0.56	2.53	1.93	none

Table 4.3: Calculated beating frequency in THz between the vibrational levels as well as higher order excited levels making use of table 4.2.

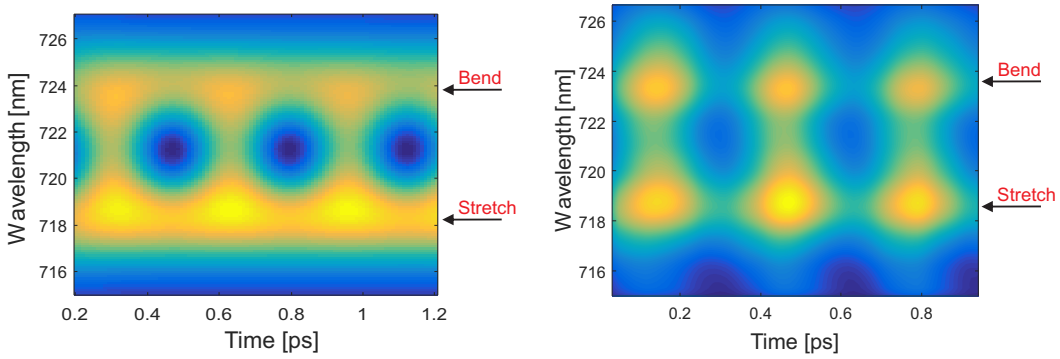

(a) (b)

Figure 4.10: (a) TR-CARS simulated and (b) experimental measurement taken of CO_2.

Even though beating was shown for two vibrational modes of CO_2 it is possible to get a beat from any two different modes, as was indicated by the research done by Roy et. al. [48]. All the frequencies present during the TR-CARS measurement can be determined using the Fourier transform on the time-related data. Therefore, not only can one infer the molecular vibrational decoherence time for a particular mode, but one can also establish the presence of other modes excited by only considering the TR-CARS traces.

In general the probe field should have sufficiently narrow bandwidth to allow different vibrational modes to be resolved in frequency CARS. On the other hand a narrow spectral bandwidth results in good resolution within the spectral domain, but poor resolution in the time domain. For time-resolved CARS one requires a broad bandwidth to obtain good temporal resolution. Careful consideration should be taken when choosing the spectral bandwidth which will allow both frequency and TR-CARS features to be resolved adequately. As example of the beating Fig. 4.11 shows a TR-CARS spectrograph simulated for 3 different probe bandwidths used. In (a), (b) and (c) the left figures represents a frequency resolved trace taken at a specific time, the middle represent the TR-CARS spectrographs while the figures on the right represent a temporal slice at the stretch and bend mode frequencies, respectively.

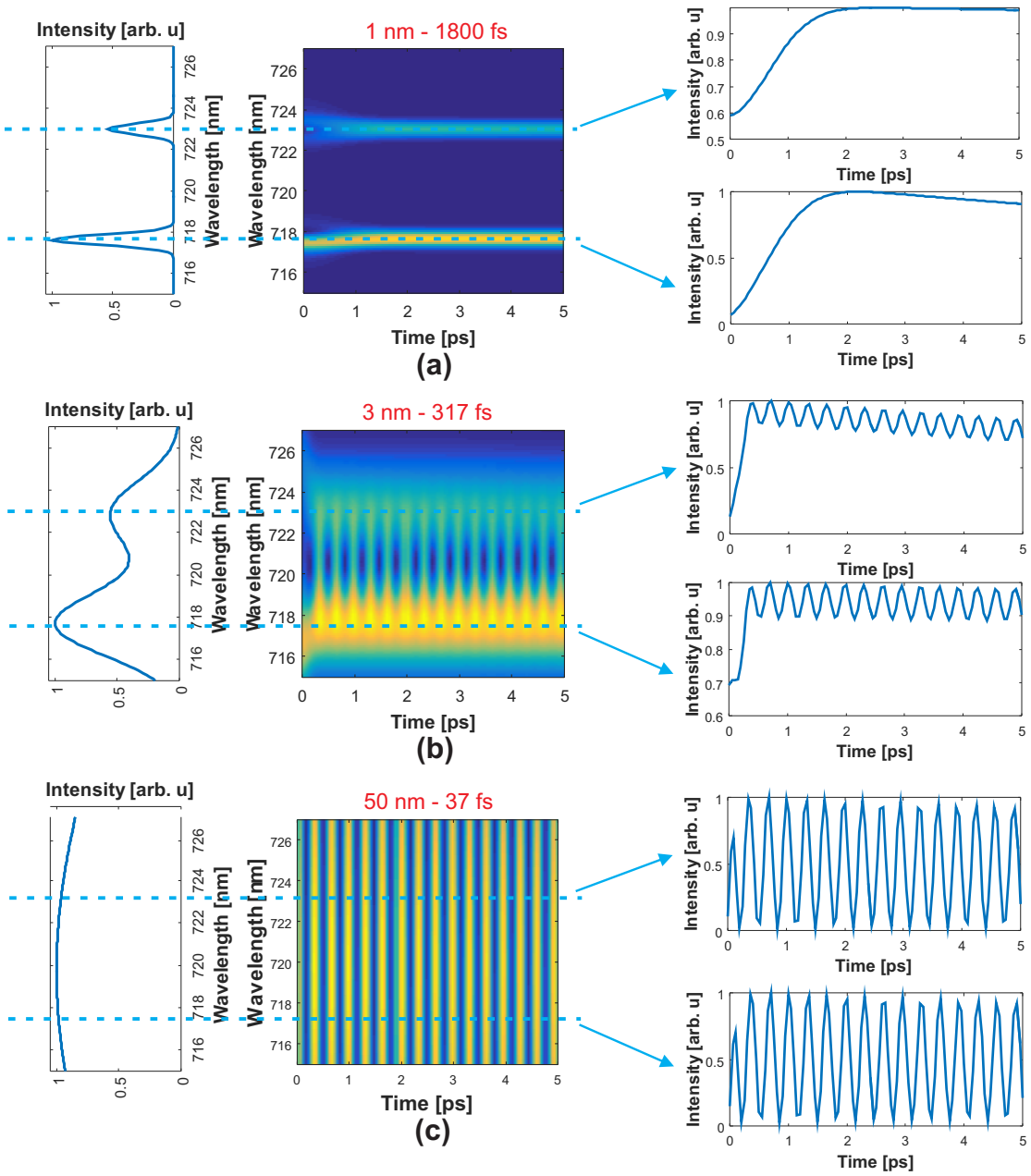

Figure 4.11: CARS signal dependence on the bandwidth of the probe is shown.

In Fig. (a) the frequency is completely resolved while temporal resolution were completely lost. In Fig. (b) neither frequency nor time is completely resolved, but both frequency and temporal attributes can be observed. Within Fig. (c) all temporal features were resolved, but none of the frequency features. This clearly indicates the importance of the probe field on the resolvability of the data. In the work presented here we chose to work with a 6 nm bandwidth probe pulse.

4.5 Summary and Conclusion

In this chapter the theory for CARS was developed. In summary CARS can only be achieved on molecules which have Raman active modes and an anti-Stokes signal will only be observed if the energy difference between the pump and Stokes field is the energy required to vibrationally excite the molecules. What makes the CARS process so attractive is that the anti-Stokes signal retrieved is unique for each and every molecule making it the ideal tool towards specific chemical identification. Furthermore, CARS is non-invasive making it ideal for measuring biological samples.

Beyond spectral CARS, TR-CARS can provide insight into the behavior of the molecule after excitation. In particular it can be used to monitor the excited life-time of the excited states and consequently the effects molecular collisions exhibit on the decay rates. Several other phenomena can also be observed in the TR-CARS traces. If more than one mode is excited a mode beating can be observed related to the energy difference between the excited states. The magnitude of the beats are dependent on the amplitude of the modes related to the beating. Even if a poor signal is observed the mode beating amplitude can infer to what extent the other modes are populated. This will be discussed in more detail in chapter 5.

Chapter 5

Control of Vibrational Dynamics

In this chapter the extent to which the vibrational dynamics of gaseous CO_2 can be controlled, is investigated. In section 5.2 numerical simulations of CARS are presented using the theoretical model derived in chapter 4 for an unshaped pump field. In section 5.3 the study shows the experimental results obtained for CARS for an unshaped pump field. In section 5.4 the study investigates vibrational control of gaseous CO_2 by changing the pump field structure responsible for SRS utilizing the learning algorithm discussed in chapter 3. The study shows and verifies that vibrational control is achieved and that the observed experimental behaviour is qualitatively closely mimicked by the numerical model developed in chapter 4. This section will once again emphasize the importance of the target function specified to the learning algorithm. By changing the target function we were able to selectively excite different vibrational modes of CO_2, increase the beat contrast between simultaneously excited modes, and control the relative phase of oscillation between different modes. We also discuss the mechanisms responsible for optimizing certain modes while suppressing others. The excellent qualitative agreement between simulations and experiments allows us to use insight gained during simulations directly in experiments. Chapter 5 is concluded with a summary of the key points learnt and achieved throughout this study.

5.1 Introduction

In the CARS process state preparation is achieved by SRS. Therefore, one only has to consider controlling the 2^{nd} order perturbation terms to achieve molecular vibrational control caused by SRS. The crux of this section is to investigate to what extent one can control the different terms in the density matrix presented by equation 4.41.

One would like to control the vibrational population as well as the coherence between the ground and vibrationally excited modes shown in Fig. 5.7. In order to achieve this, one requires control over both temporal and spectral aspects of the CARS schemes. Population changes can directly be observed in a narrowband probe CARS signal, but not the temporal coherence. The temporal coherence between different vibrational modes results in a vibrational wave-packet that

evolves in time and can only be observed using time delayed measurements i.e. time-resolved CARS.

Control now depends on how well one can change the vibrational population as well as modify the coherence between modes. In the work that follows control of these phenomena in both simulations and experiments are shown. The similarities and differences between the results of simulations and experiments are also analysed.

5.2 Numerical simulation of CARS for CO_2 with unshaped pumping

In this section the expressions derived in section 4.4 are used to computationally simulate the process of CARS for the bend and symmetric stretch vibrational modes of gaseous CO_2. Equation 4.51 showed how the anti-Stokes signal relates to the convolution between the response function $R(\Omega)$ and the probe field $E_{pr}(\omega - \Omega)$. In turn, the response function is dependent on the molecular lineshape $L(\Omega)$ as well as the convolution $A(\Omega)$ between the pump and Stokes fields. The lineshape for the two modes considered are represented using Lorentzian profiles of the form,

$$L(\Omega) = \frac{C'_{v_1 g}}{(\omega_{v_1 g} - \Omega - i\gamma_{v_1 g})} + \frac{C'_{v_2 g}}{(\omega_{v_2 g} - \Omega - i\gamma_{v_2 g})}, \tag{5.1}$$

derived from the response function equation 4.47. This work is only concerned with the relative intensities, rather than absolute intensities, of the CARS signals. As a result we normalized the maxima of detected or calculated signals to 1 in the figures. This preserves the good qualitative agreement between the model and measurements. To obtain agreement between the experimental observations and the numerical model one requires some input from experimental observations. During experiments with an unshaped pump field (Fig. 5.9) we observed that the stretch mode signal strength was almost twice as strong as the bend mode. For this reason numerical values for $C'_{v_1 g}$ and $C'_{v_2 g}$ were used such that the lineshape of the stretch mode will have a larger amplitude than that of the bend mode in the model. During experiments, the filters in the Stokes beam path can be tilted which shifts the central wavelength of the spectra passing through the filter while keeping the spectral bandwidth the same. This change the convolution between the pump and Stokes field for the various vibrational modes allowing one to change the signal strength of the various vibrational modes relative to each other. In simulations this is achieved by shifting the central spectral position of the Stokes field to slightly higher or lower wavelengths.

During measurements we observed that the bend mode completely decayed after roughly 150 ps while for the stretch mode a faint CARS signal persisted even up to 1.5 ns. Equation 5.1 is a complex function which if necessary can be separated into its real and imaginary parts. The real and imaginary parts of the molecular lineshape, $L(\Omega)$, for the stretch and bend modes of CO_2 obtained during simulations are shown in Fig. 5.1 (a) and (b) having used $\gamma_{v_1 g} = 1/(1.5\ ns)$ and

$\gamma_{v_2 g} = 1/(150\ ps)$ for the decay constants of the stretch and bend modes, respectively, based on the experimentally observed decay rates.

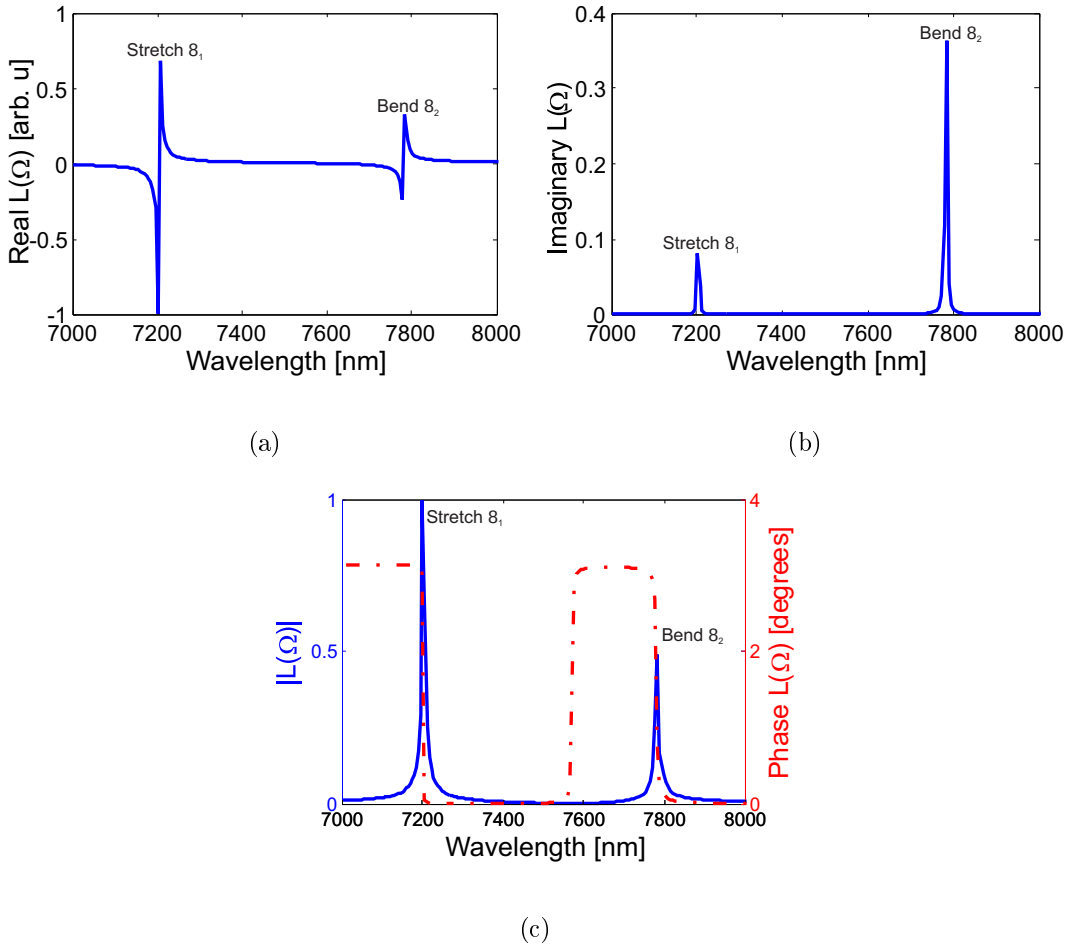

Figure 5.1: This plot represents the numerical simulation of the lineshape of the stretch and bend vibrational modes of CO_2. (a) Is the real part and (b) the imaginary part of the lineshape, $L(\Omega)$, normalised to 1. (c) Is the absolute value and phase of $L(\Omega)$. In (c) the phase is 0 in the wavelength region where $L(\Omega)$ is positive in (a) and π in the region where $L(\Omega)$ is negative in (a).

The applied fields are numerically represented by an array of amplitude and phase components within the spectral domain. To closely resemble the experimental data a 14 nm bandwidth unshaped pump field centered at 797 nm and a pulse duration of roughly 108 fs were used. The Stokes field is centered at 892 nm consisting of a 4 nm bandwidth and a pulse duration of roughly 1 ps. The Stokes field was chirped to closely represent that seen during experiments which were most likely induced during the non-linear interactions inside the TOPAS. As mentioned in section 4.4.2 a narrow bandwidth probe field leads to good frequency CARS resolution, while a broad bandwidth probe field leads to good TR-CARS resolution. To accommodate both frequency and time-resolved CARS a bandwidth of 6 nm at 798 nm were used as the probe field.

All the fields were assumed to have Gaussian amplitude distributions in frequency. The various fields are shown in Fig. 5.2 (a), (c) and (e) for the pump, Stokes and probe fields represented in the spectral domain while Fig. 5.2 (b), (d) and (f) shows the pump, Stokes and probe fields within the temporal domain, respectively.

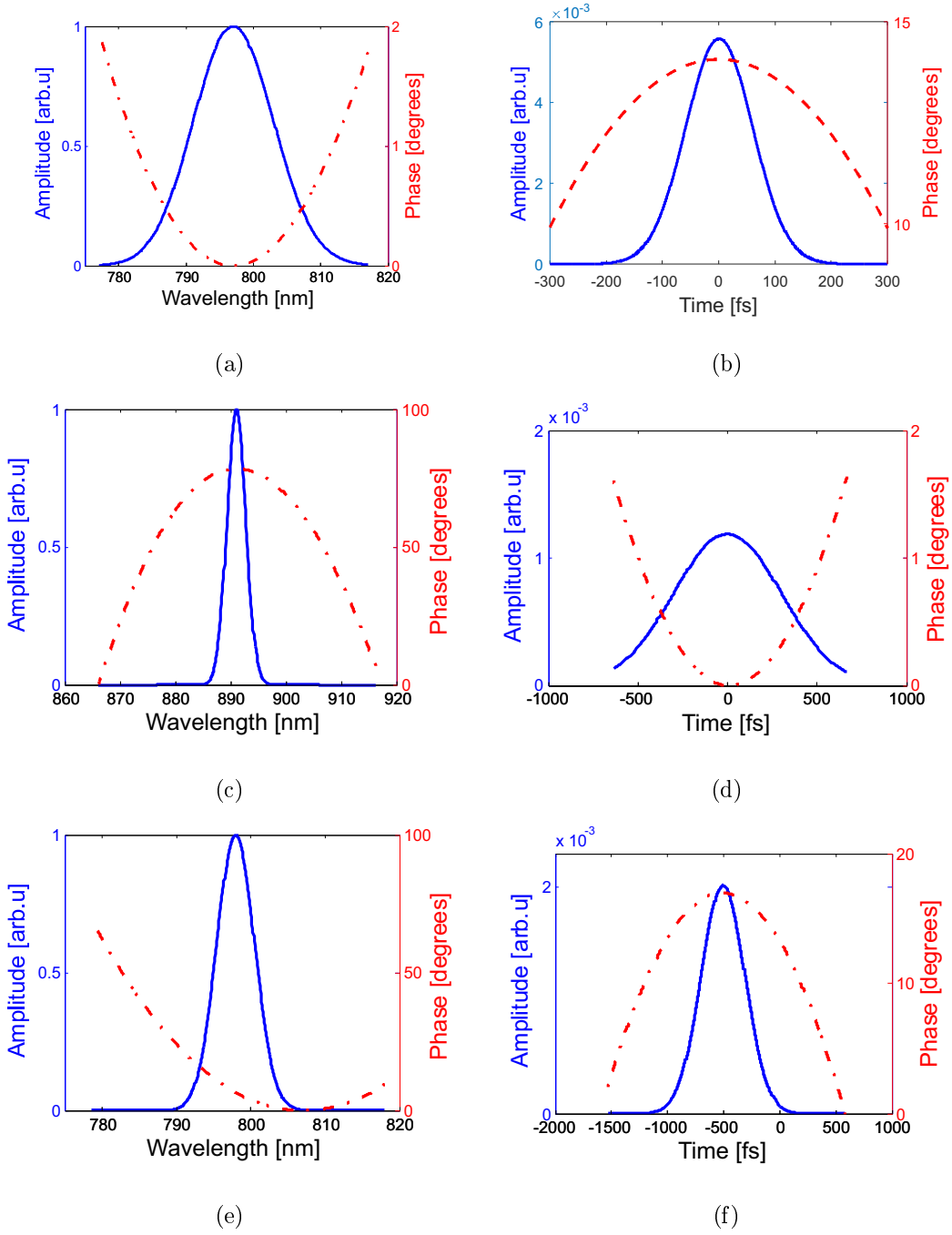

Figure 5.2: Unshaped pump, Stokes and probe fields used during simulations. (a), (c) and (e) represent the pump, Stokes and probe fields within the frequency domain while (b), (d) and (f) represents the pump, Stokes and probe fields within the temporal domain, respectively. For each field the solid line is the amplitude and the broken line the phase in the respective domains.

Lets now consider the convolution, $A(\Omega)$, between the pump and Stokes fields in the frequency domain, according to equation 4.38. To illustrate the effect on $A(\Omega)$ of having pump and Stokes fields with different spectral characters, 3 different pump spectral profiles are selected

from the unshaped spectrum via spectral shaping and then overlapped with the unshaped Stokes field. The cases where the pump-Stokes overlap is predominantly on resonant with the stretch mode, predominantly on resonant with the bend mode and where overlap is on resonant with both modes at the same time are presented. These pump fields are shown in Figure 5.3 (a). Experimentally these fields can be created either by filtering from a broad band input field or by SLM based amplitude shaping. The convolution with the Stokes field as a result of these pump fields are shown in Figure 5.3 (b). The response, $R(\Omega)$, which is given by $R(\Omega) = L(\Omega) A(\Omega)$ for the convolutions between what is shown in Figure 5.3 (b) and the lineshape from Figure 5.1 are shown in Figure. 5.3 (c). Figure 5.3 (c) shows overlap between the field convolution and the lineshape is achieved for the different pump fields considered.

For a narrowband probe equation 4.51 implies that the probe field will generate an anti-Stokes signal resembling $R(\Omega)$. If the response function, $R(\Omega)$, is zero in a spectral region related to a vibrational mode excitation then the mode cannot be populated by the pump-Stokes combination. From Figure 5.3 (c) one sees different modes can be suppressed or allowed purely by choosing the appropriate pump field. This can lead to mode selectivity. Finally, the CARS spectrum can now be obtained using equation 4.47 and is shown in Figure 5.3 (d) for the cases stipulated in Figure 5.3 (a).

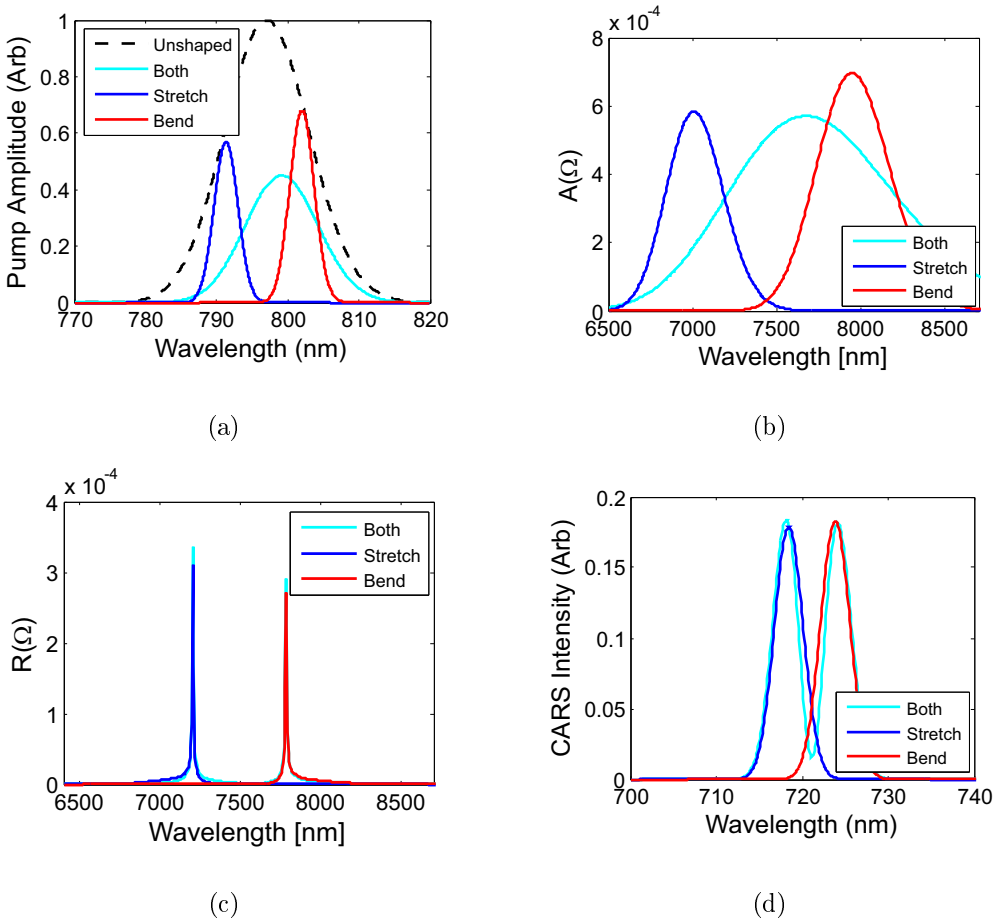

Figure 5.3: Vibrational response function, $R(\Omega)$ is shown. (a) Shows various pump fields starting with the unshaped pulse spectrum represented by the dashed line, spectral shaping is used to produce either the blue, red or cyan spectral profiles. The blue-lined field will favour the stretch mode, the red-lined field will favour the bend mode while the cyan-lined field will favour both modes equally. (b) Shows the convolution, $A(\Omega)$, between the pump and Stokes fields in the spectral domain. (c) Shows the vibrational coherence, $R(\Omega)$, response function in the spectral domain while (d) shows the simulated anti-Stokes signal for the frequency-CARS process considering the 3 pump fields in (a).

As was discussed in section 4.2.3 the frequency of the observed beating in time-resolved CARS traces depends on the energy difference between the vibrational modes, while the magnitude of the beating amplitude contrast depends on the coherence between the modes as well as the signal intensity of the modes relative to each other. To illustrate this point consider mode 1 of the CARS signal high while a low intensity is considered for mode 2 of the CARS signal. This will result in a small magnitude for the beating between the modes according to section 4.4.4.

Mode suppression can be verified by looking at the TR-CARS spectra. If a mode is suppressed then the beating caused by that mode with other modes will diminish significantly. Figure 5.4(a) shows a simulation of the TR-CARS spectrograph for a pump field populating

both modes while in (b) the pump field predominantly populates the stretch mode. In Figure 5.4 frequency slices are shown for the spectrographs at the maximum intensity of the stretch and bend modes. In (a) strong beating is observed for both modes. In (b) however the bend mode was suppressed. The frequency slice of the TR-CARS spectrograph at the bend mode shows a very small signal relative to the stretch mode. Furthermore, the beating observed in the modes significantly decreased in comparison to what was observed in (a). The low intensity (3 orders of magnitude smaller) for the frequency slice at the bend mode and the decline in the beat contrast observed for the modes strongly suggest the bend mode was effectively suppressed. In Fig. 5.4 (a) a strong signal for both modes leads to a large beat contrast of 0.081 for the stretch mode and 0.055 for the bend mode while a small beat contrast is observed of 0.00005 for the stretch mode and 0.0061 for the bend mode in Fig. 5.4 (b).

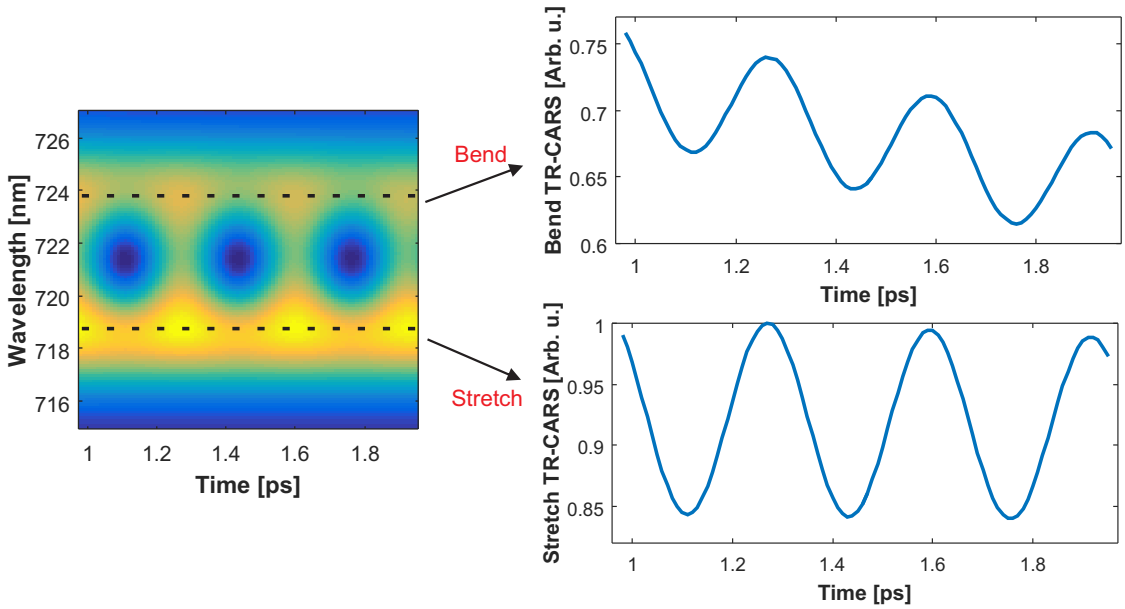

(a)

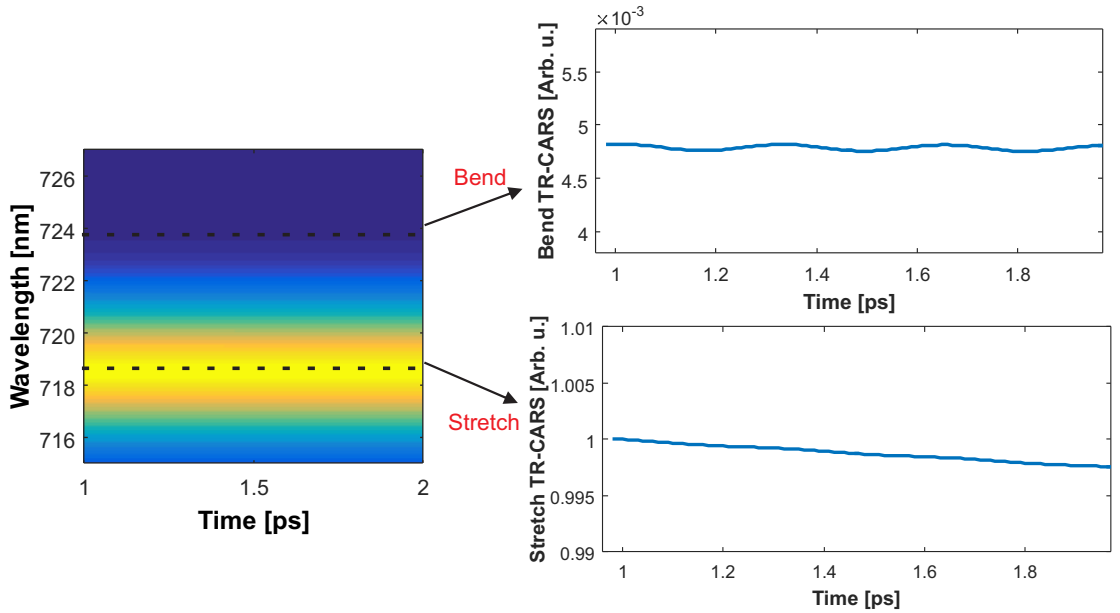

(b)

Figure 5.4: Simulated TR-CARS. (a) Simulated TR-CARS spectrograph when both modes are strongly populated. Frequency slices of the spectrograph is also shown to illustrate the amplitude beating of the modes. What can be seen is a beating in the temporal evolution of the signal. (b) Simulated TR-CARS for the pump case predominantly leading to the stretch mode occupied. The beat contrast drastically diminished because the bend mode was suppressed.

As indicated in Figure 5.4 (a) the 6 nm bandwidth for the probe field proved sufficient for both frequency and time resolved CARS leading to acceptable resolution in both domains. Both modes were resolved in the frequency CARS measurements and high contrast was obtained for the time domain beating in the TR-CARS spectra. A Fourier transform of TR-CARS spectra shows a beating with a period of 322 fs or 3.1 THz which corresponds to the energy difference between the vibrational levels once again illustrating the coherence between the two vibrational modes.

5.3 Unshaped Pump Experimental CARS for CO_2

Experimental Procedure

The CARS setup used for the work presented here combines aspects of frequency and time-resolved CARS as explained in section 4.2.3. A simplified schematic representation of the experimental setup can be seen in Figure 5.5. In this setup the pump, Stokes and probe fields are all generated from a single broadband source (Coherent Evolution). Conversion from one light source to the sources used in this work were thoroughly explained in sections 2.3 and 2.4. The source laser is split into 3 parts by beam-splitters, BS_1 and BS_2.

The pump arm passes under mirror M_3 and is steered towards a Bragg grating, BG_1 (consisting of 1200 lines/mm) spatially separating the different frequencies. Lens L_1 placed at a focal distance away from the grating collimates the dispersed light. The spatially spread coherent field now goes through a spatial light modulator, SLM, placed a focal distance away from the lens to facilitate pulse shaping. Mirror M_2 reflects the pump field back onto itself, through the SLM a second time. The pump field is now focused by lens L_1 back onto the grating. Effectively the pump field went through a 4f-optical configuration double passing the SLM. The first diffractive order from the grating is used as the shaped pump field while discarding all other orders. Mirrors M_3 and M_4 steers the shaped pump field towards a delay line consisting of a manually controlled translation stage T_1 as well as mirrors M_5 and M_6 used to temporally overlap the pump field with other fields required for CARS.

The Stokes arm goes through a frequency converting unit (TOPAS-C from Coherent described in section 2.3) converting 797 nm to 892 nm. The broad bandwidth from the TOPAS-C is now narrowed to 4 nm with low and high pass filters F_1 (Newport, 10LWF-900, 10SWF-900) and its polarization is controlled with a half-wave plate, $\lambda/2_1$. The Stokes field is then sent through a delay line consisting of mirrors M_8 and M_9 as well as another manually controlled translation stage T_2.

The probe field was filtered by low and high pass filters (Newport, 10LWF-800, 10SWF-800). to control the bandwidth and shape of the probe field. A half-wave plate, $\lambda/2_2$ allows control of the probe field polarization. The probe field now goes through a delay line consisting of mirrors M_1 and M_2 as well as an electronically controlled translation stage (Thorlabs, MTS25-Z8). This translation stage allows system automation with regards to temporal delays used when collecting data for TR-CARS.

The pump, Stokes and probe field are now collinearly combined with BC_1 and BC_2 and

all fields are steered towards the reaction cell by mirrors M_{13} and M_{14}. At this stage in the setup the pump, Stokes and probe field preparation as well as their spatial overlap are achieved. Furthermore, the pump and Stokes fields are also overlapped temporally while the probe field is temporally delayed.

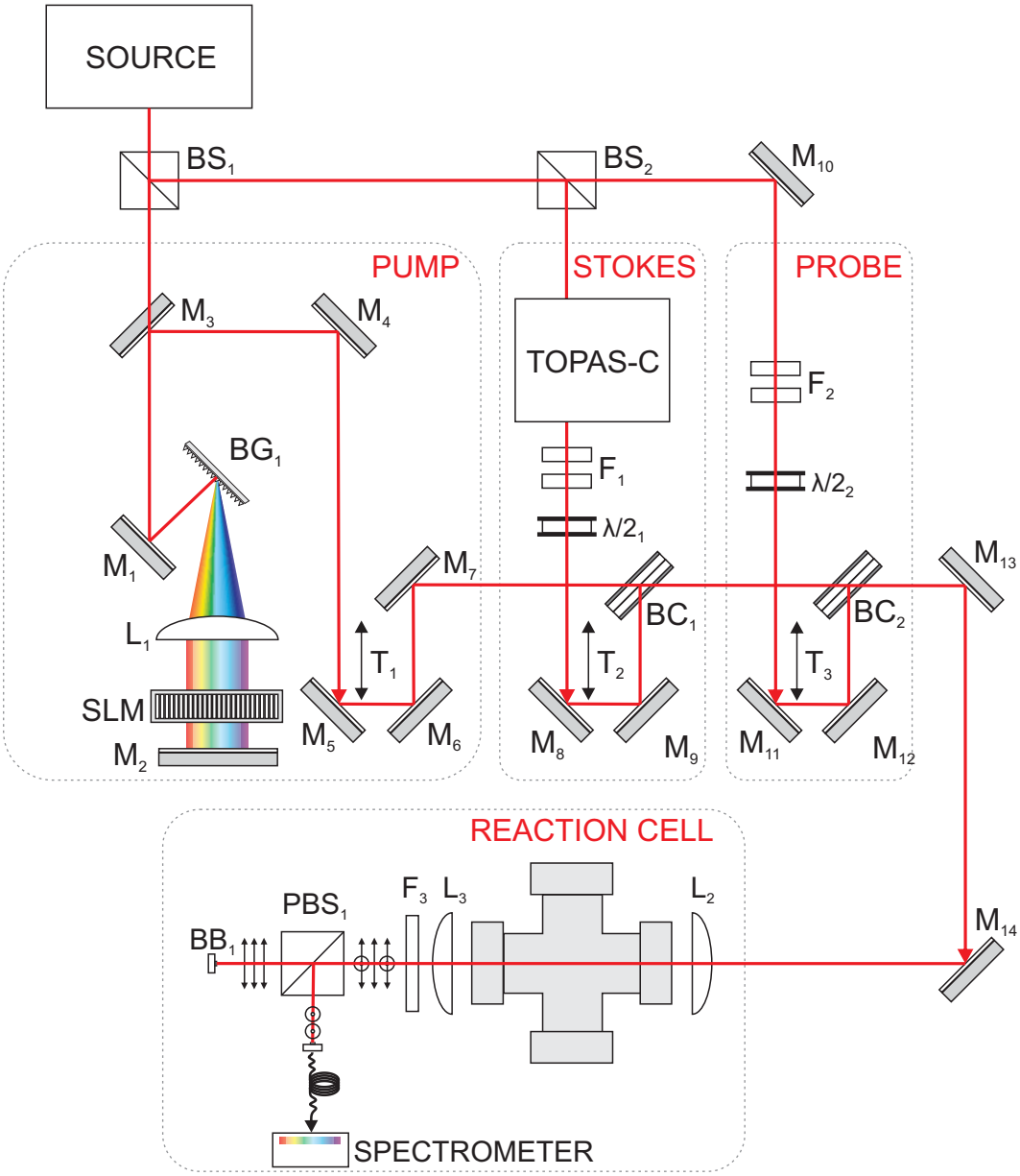

Figure 5.5: Schematic representation of the experimental setup used for CARS. In subsequent sections this setup was integrated with software enabling closed loop optimization consequently leading to mode selectivity.

The fields are now focused by lens L_2 inside the reaction cell where CARS can take place. The input fields and generated CARS signal pass through lens L_3 which focuses the beams

at a considerable distance away from the reaction cell. This distance allows one to filter out unwanted signals before collecting the CARS spectrum. Directly after L_3 the input fields are removed from the CARS signal using a low pass filter (Edmund optics, 750 nm low pass). As mentioned previously the desired CARS signal will have the same polarization as the probe field which was selected to be horizontally polarised. A polarizing beam splitter, PBS_1, separates the CARS signal created by the probe field from any CARS signal generated unintentionally by the pump field acting as a probe itself. The probe field is also temporally delayed with respect to the Stokes field to ensure it would not act as the pump field. Finally the horizontally polarised CARS signal is measured with a spectrometer (ocean optics, USB2000) while the vertically polarised CARS signal is discarded making use of a beam dump.

At this stage in the work no shaping took place. The structure of the fields used in generating the CARS signal play a crucial role. Spectrometers can measure the spectral attributes of pulsed fields, but cannot provide any information with regards to its phase. As explained previously there is also no direct measurement technique allowing measurement of the pulse structure in time. Therefore, the spectral and temporal attributes of the various fields were rather extracted from SHG-FROG trace spectrograph measurements using commercial software available [55]. Figure 5.6(a), (d) and (g) show the measured SHG-FROG traces for the pump, Stokes and probe fields, respectively. Figure 5.6 (b), (e) and (h) show the frequency domain and Figure 5.6 (c), (f) and (i) the temporal domain representations extracted of the pump, Stokes and probe fields, respectively.

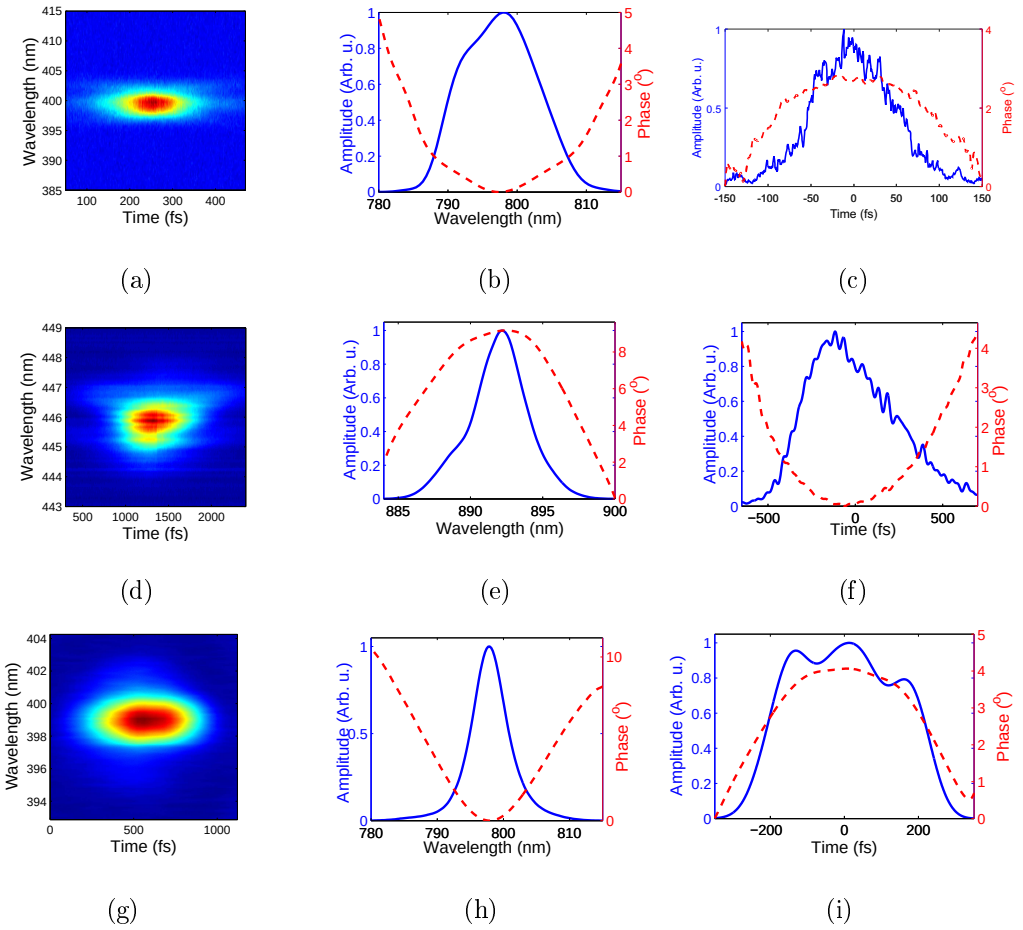

Figure 5.6: The spectral and temporal fields extracted from SHG-FROG trace measurements of the pump, Stokes and probe fields are shown. (a) is the SHG-FROG trace measurement of the unshaped pump field. (b) is the extracted spectral representation of the pump field exhibiting a 14 nm bandwidth while (c) is its temporal representation with a pulse duration of roughly 133 fs. (d) shows the SHG-FROG trace measurement of the Stokes field used to extract its spectral and temporal characteristics in (e) and (f), respectively. A spectral bandwidth of 3.882 nm is obtained which is slightly chirped to produce a pulse duration close to 587.7 fs. (g) is the SHG-FROG trace measurement of the probe field. (h) and (i) show the extracted spectral and temporal representations of the probe field exhibiting a bandwidth of 5.942 nm which is chirped to produce a pulse duration of 434.1 fs .

The pump, Stokes and probe powers were kept fixed at roughly 30, 15 and 10 mW, respectively. With minimal changes made to the experimental setup over the course of this work one assumes that the Stokes and probe fields did not change dramatically over time.

Experimental CARS Measurements

The CARS measurements shown in this section were collected without applying any pump shaping. The reaction cell was filled with 99 % pure CO_2 gas to 2 bar and the temperature was roughly 21°C. Figure 5.7 shows a typical frequency multiplex CARS signal measured

demonstrating good temporal and spatial overlap between the pump and Stokes fields. For this measurement the probe field was spatially overlapped with the excited molecules. To get the time-resolved CARS, spectra were collected while temporally delaying the probe field. One observes two peaks which correspond to the stretch and bend modes of CO_2. Time-resolved CARS measurements were now conducted while keeping the pump and probe fields fixed. This was achieved by collecting the maximum signal strength of each of the peaks in the frequency multiplex CARS spectra while increasing the time delay of the probe field. The TR-CARS spectra on the left of Figure 5.7 is for the stretch mode while that on the right is for the bend mode collected at intervals of 0, 50 ps, 100 ps, 150 ps, 200 ps and 1 ns displacements. These intervals provide information of the decoherence time of the various modes.

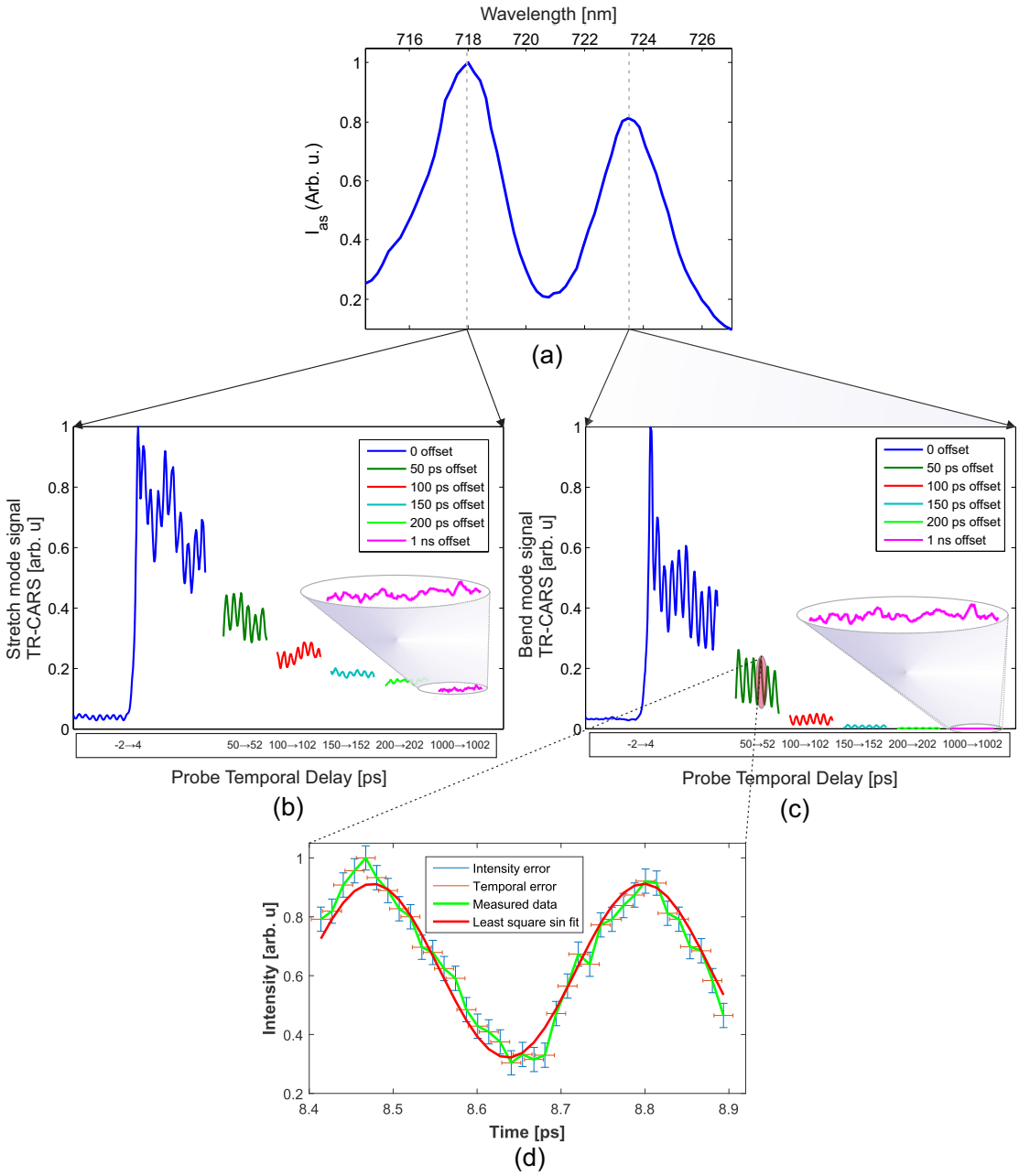

Figure 5.7: In (a) the measured frequency multiplex CARS while in (b) and (c) the time-resolved CARS for CO_2, when using an unshaped pump field, is shown for the stretch and bend modes respectively. The $(1, 0^0, 0)$ symmetric stretch mode (b) as well as the first harmonic bend mode $(0, 2^1, 0)$ (c) are excited simultaneously. The TR-CARS spectra at the bend mode show the mode decohered completely close to 1 ns while the stretch mode strength decreased quite significantly, but can still be observed. After 1 ns, as a result of the bend modes disappearance, the beating dissappeared in the TR-CARS trace for the stretch mode as expected. (d) Here each experimental point represents the average of 40 measurements accumulated over 10 ms of integration time of the spectrometer. Error-bars were calculated for the data obtained from the ocean optics spectrometer as well as the stepping motor (thorlabs). The error-bars represent the estimated deviation from the mean at each point resulting from shot-to-shot fluctuations. The temporal uncertainty was obtained from the translation stage position resolution as per manufacturer specifications. These error-bars are representative of all experimental traces to follow in which we only show the average of the data.

As expected the signal strength and beating contrast decrease in both modes as a result of some decay effect for longer temporal delays. We assume this is most likely due to collisions as the mean free time for a collision was calculated as 111 ps in section 4.3. For a probe delay longer than 1 ns only the stretch mode is observed. Consequently the TR-CARS beating in the stretch mode also disappeared as there is no coherence between the stretch and bend modes anymore. The signal in TR-CARS trace for the stretch mode shows the stretch mode decoherence time is longer than 1 ns while in the TR-CARS trace for the bend mode one can see the bend mode decoheres after roughly 150 ps. The decoherence time of the bend mode is comparable to the collisional time which indicate the decoherence is most likely due to collision and not spontaneous decay.

A Fourier transform of the TR-CARS traces will identify the underlying beat frequencies present without much effort. Figure 5.8 (a) shows the Fourier transform of the TR-CARS signal for the stretch mode while (b) is that of the bend mode for a temporal delay of roughly 2-3 ps. (c) Shows the Fourier transform of the TR-CARS signal for the stretch mode while (d) is that of the bend mode for a delay longer than 1 ns for the probe. In both (a) and (b) a strong beat frequency signal were obtained for the energy difference between the stretch and bend mode at 3.08 THz which closely match the calculated beat frequency of 3.09 THz. Other beat frequencies can also be seen whose origin could not be clearly identified in the frequency multiplex CARS. These were located at 0.56 THz which might be the beating between the ν_2 and ν_4 modes in table 4.3 and 0.41 THz which is unknown. This once again illustrates one of the advantages of using time-resolved CARS to observe extremely weakly populated modes not observable using frequency CARS methods. Above we claimed the bend mode decoheres roughly after 150 ps. In Figure 5.8(c) the Fourier transform of the stretch TR-CARS signal do not show any beat frequency between the stretch and bend modes while in Figure 5.8(d) the Fourier transform of the bend TR-CARS signal provide no information as the mode already decohered.

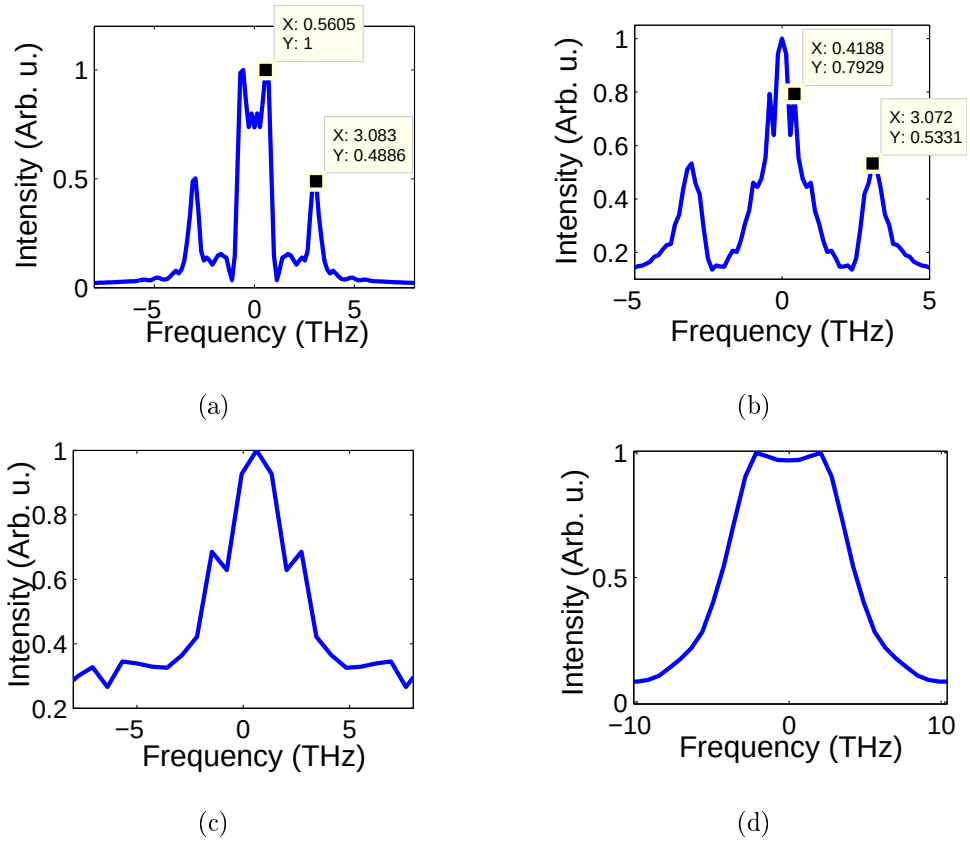

Figure 5.8: Fourier transform for time-resolved CARS measurements taken at different time intervals. (a) and (b) is the Fourier transform of the TR-CARS measurement of the stretch $(1, 0^0, 0)$ and bend $(0, 2^1, 0)$ modes considering 0 ps offset while (c) and (d) is for an offset of 1 ns. In (c) the beat frequency disappeared from the stretch mode TR-CARS measurement while in (d) the bend mode TR-CARS signal disappeared. At 0 frequency a high peak is observed due to the non-zero offset of the TR signal on the intensity axis.

The CARS signals obtained in this section are a consequence of an unshaped pump field and will be used in subsequent sections to compare the CARS signal outcome for shaped pump fields relative to the unshaped pump field.

5.4 Vibrational Control

5.4.1 Control of Vibrational Excitation and Population

In section 5.2 this study has shown numerical results and in section 5.3 experimental results for CARS of CO_2 using an unshaped pump field. Typical anti-Stokes signals obtained are shown in Figure 5.9(a) numerically and (b) experimentally.

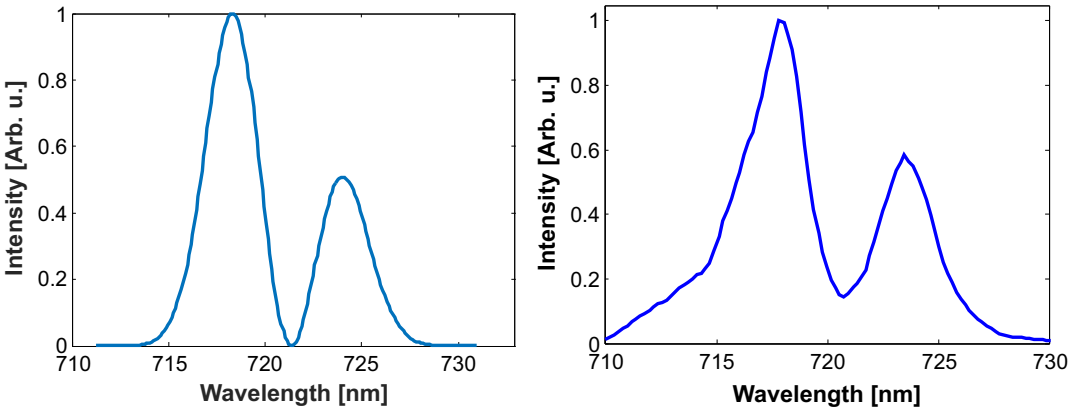

(a) (b)

Figure 5.9: (a) Simulated and (b) experimental anti-Stokes signal obtained making use of an unshaped pump field.

One would however like to control which mode will be excited as has been done before by other groups [95]. In this section we make use of the learning algorithm from chapter 3 to extract the pump field amplitude and phase profiles which will allow to select the mode. In doing so we will test the learning algorithm to see whether it finds the expected solutions. Examples of target functions which will lead to the enhancement of different modes as highlighted in section 5.2 are as follows,

$$F = -\frac{\max(Peak_2)}{\max(Peak_1)+\mathrm{c}}, \tag{5.2}$$

$$F = -\frac{\max(Peak_1)}{\max(Peak_2)+\mathrm{c}}, \tag{5.3}$$

and

$$F = -\frac{\max(Peak_1)+\max(Peak_2)}{\mathrm{abs}(max\,(Peak_1) - max\,(Peak_2))+\mathrm{c}}. \tag{5.4}$$

The aim of target function equation 5.2 is to maximize the bend mode occupation while minimizing the stretch mode occupation. Target function equation 5.3 aims to optimise the stretch mode occupation while suppressing the bend mode occupation. For both of these cases minimization of the value of the target function does not imply complete suppression of the unwanted modes, but rather imply an increase in the relative signal strength for a desired mode. The last target function, equation 5.4, is set to optimize occupation of both modes while trying to keep their signals strengths similar. For each of these target functions a constant c is added to the denominator to ensure dividing by 0 is not possible. For small c values in equation 5.2 more

emphasis is placed on suppressing the stretch mode than exciting the bend mode while larger c values place more emphasis on exciting the bend mode than suppressing the stretch mode. Careful consideration of the target functions or even evolving the target function as the learning algorithm progresses can significantly improve the optimal solution extracted. However, finding the best possible target function falls outside the scope of this study.

Maximize Bend Mode Occupation

Figure 5.10 shows the results obtained using the target function equation 5.2 to increase the intensity of the bend mode relative to the stretch mode; Figure 5.10 (a-c) show numerical simulations while Figure 5.10 (d-f) shows the experimental results. (a) Is the extracted pump field structure represented in the von Neumann basis and (b) is its Fourier domain counterpart which lead to the simulated frequency CARS spectra shown in (c). In Figure 5.9 (a) for an unshaped pump field the CARS spectra shows strong signals for both the modes while in Figure 5.10 (c) only the bend mode can be observed.

During experiments the extracted pump field were not directly measured, but rather the unshaped pump field measured in the previous section were used in conjunction with the field shaping applied to the unshaped field to estimate the shaped pump field afterwards. This was mainly done because an inline SHG-FROG trace measurement technique would have slowed down the optimization drastically. Laser drift also hindered us from allowing the experiment to run too long. The experimentally extracted field in the von Neumann basis, Figure 5.10 (d), and its equivalent counterpart in the frequency domain, Figure 5.10 (e), lead to the measured frequency CARS spectra shown in Figure 5.10 (f). For an unshaped pump field the CARS spectra shown in Figure 5.9 (b) shows strong signals for both the stretch and bend modes while the shaped field lead to CARS spectra where only the bend mode is observed in Figure 5.9 (f).

Figure 5.10 (c) and (f) show both simulation and experiment succeeded in suppressing the stretch mode relative to the bend mode. Subtle differences between simulation and experiments can be seen for the extracted shaped pump fields though. From the results we can see the mechanisms responsible for mode selectivity can either be energy conservation laws or temporal overlap considerations caused by the phase difference between frequencies of the various fields.

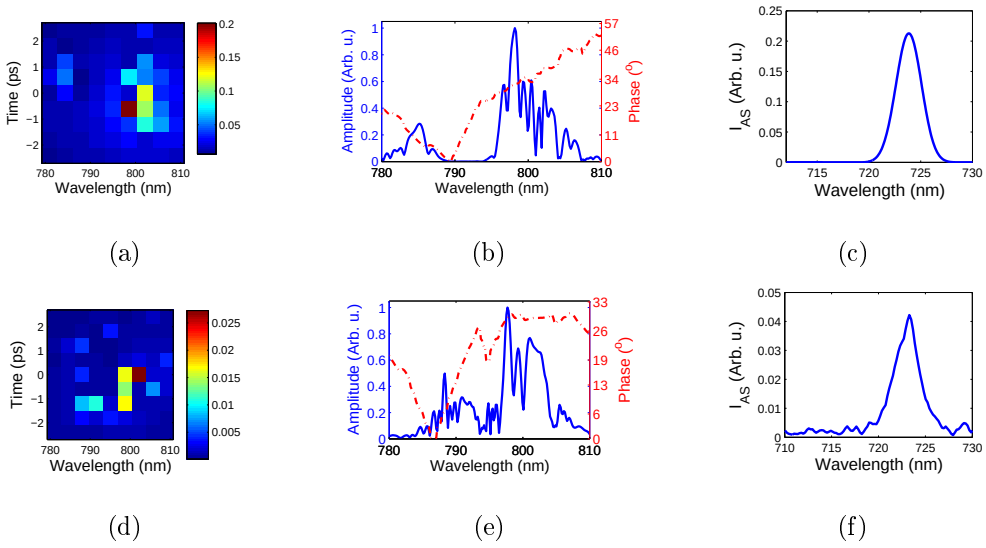

Figure 5.10: Simulation and experimental results for optimizing the bend mode as specified by the target function equation 5.2 is shown. (a-c) Show the simulations while (d-f) show the experimentally obtained results. The pump field in the von Neumann basis (a) or its frequency domain counterpart (b) extracted during simulations leads to the CARS spectra in (c) exhibiting a strong signal for the bend mode relative to the stretch mode. (d) and (e) is the experimentally extracted pump field within the von Neumann representation and frequency domain which produced the CARS spectra in (f) also exhibiting a strong signal for the bend mode relative to the stretch mode.

During simulations the learning algorithm suppressed the amplitude of the frequency components below 796 nm, but not those above 796 nm. This allows on resonant excitation for the bend mode and only off-resonant excitation for the stretch mode. The phase for frequency components resonant with the bend mode were also modified leading to a shift forward in time and consequently better temporal overlap with the Stokes field. The frequency components between 780-790 nm which might be on-resonant with the stretch mode were temporally shifted in the opposite direction than the bend mode on-resonant frequency components. Jointly these mechanisms suppressed the stretch mode while allowing bend mode excitation.

During the experiments this study found phase modifications were made to the frequency components on-resonant with the stretch mode such that they were temporally shifted backwards in time. These frequency components did not temporally overlap with the Stokes field. The frequency components on-resonant with the bend mode were not modified at all which lead to temporal overlap between these frequency components and the Stokes field. Once again these mechanisms lead to the suppression of the stretch mode and excitation of the bend mode.

Previously we showed that for unshaped pump fields two strong vibrational modes will be excited for CO_2. We also showed measurement of the beat frequencies in a mode lead to information with regards to other modes also occupied. In fact, a beat frequency was observed for a mode even though a direct measurement showed no trace of the mode. This is most likely due to a very weakly populated stretch mode. The absence of beat frequencies in the TR-CARS for the bend mode can therefore be used to verify the stretch mode were successfully suppressed.

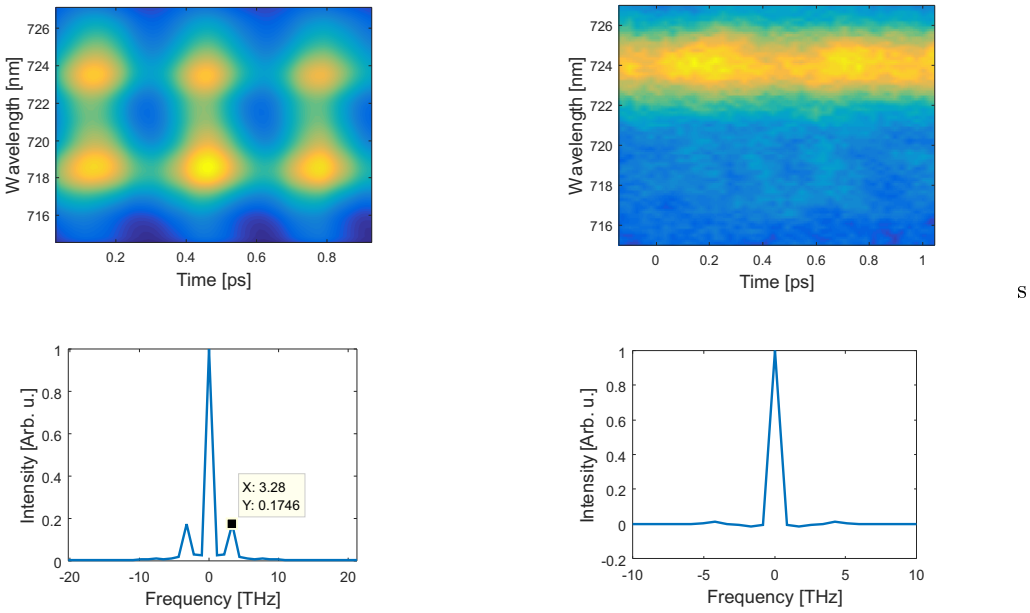

(a) (b)

Figure 5.11: (a) Experimental TR-CARS trace measured at the maximum signal value for the bend mode before shaping took place. A Fourier transform on the data for the bend mode shows a beat note of 3.28 THz (b) Shows the measured TR-CARS signal after pump shaping took place. A Fourier transform on the data for the bend mode shows no beating. This clearly states the stretch mode was effectively suppressed.

Figure 5.11(a) shows the TR-CARS before pump shaping took place exhibiting the beat between the stretch and bend modes. In (b) one sees the TR-CARS after shaping took place where the beating is strongly suppressed. As the beating is an indication of both vibrational modes populated one can say without a doubt that the stretch mode has effectively been suppressed. In (b) a Fourier transform on the TR-CARS spectrograph showed no trace of a beating between modes.

Maximize Stretch Mode Occupation

Using the target function specified by equation 5.3 this study obtained the results shown in Figure 5.12 (a-c) for simulations and 5.12 (d-f) during experiment. The figure structure is the same as explained in the section denoted "maximize bend mode". Once again the learning algorithm was successful in maximizing the stretch mode occupation relative to the bend mode occupation for both simulations and experiments. During simulations the frequencies on resonant with the stretch mode temporally overlapped with the Stokes field. The amplitude of the frequencies which overlapped with both vibrational modes were suppressed, while the frequencies on-resonant with the bend mode were shifted back in time.

The experimental results show mode suppression of the bend mode was achieved by temporally shifting the frequency components responsible for direct on-resonant bend mode excitation.

The frequency components which excite both modes were chirped, while the frequency components which lead to on-resonant stretch mode excitation had no phase change.

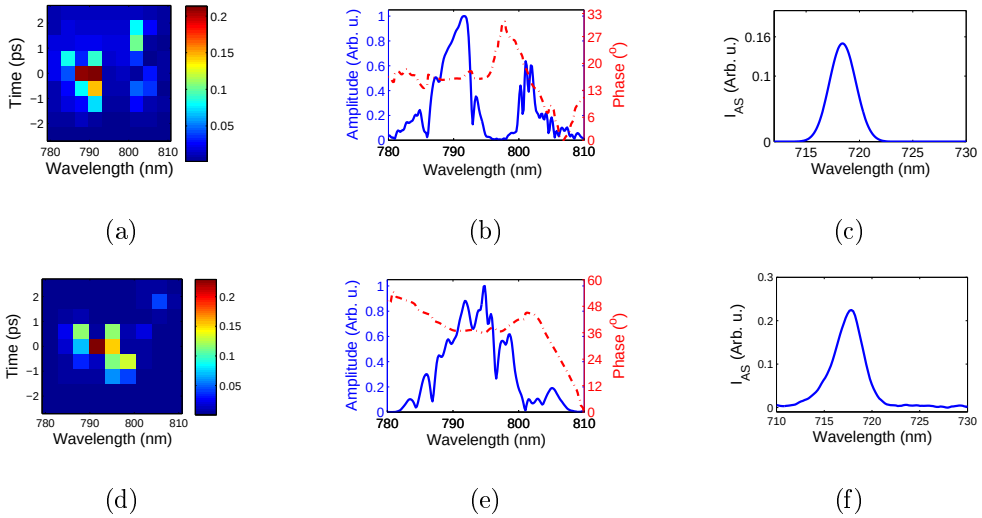

Figure 5.12: Simulation and experimental results for optimizing the stretch mode relative to the bend mode occupation as specified by the target function in equation 5.3. (a-c) Show the simulations while (d-f) show the experimentally obtained results. The pump field in the von Neumann basis (a) or its frequency domain counterpart (b) extracted during simulations leads to the CARS spectra in (c) exhibiting a strong signal for the stretch mode relative to the bend mode. (d) and (e) is the experimentally extracted pump field within the von Neumann representation and frequency domain which produced the CARS spectra in (f) also exhibiting a strong signal for the stretch mode relative to the bend mode.

Once again in both the simulations and experiments the study showed it was possible to suppress one particular mode relative to another.

Minimize Difference In Modes

As shown in Fig. 5.9 without shaping the signal strength of the stretch mode is stronger than the bend mode. The results obtained for the target function equation 5.13 to get the modes equal in strength can be seen in Figure 5.13. Once again the Figure numbering and sequence is the same as above. The simulations show a constant phase and the initial Gaussian field amplitude distribution lead to both modes populated almost equal in strength. However, for the experiments we found the side skirts of the Gaussian profile were ignored. This most likely imply the skirts do not contribute significantly to the solution while the main contribution was from the central frequency components leading to both bodes on resonant. The frequency components below 791 nm which will drastically enhance the stretch mode, but with little effect on the bend mode, were temporally shifted.

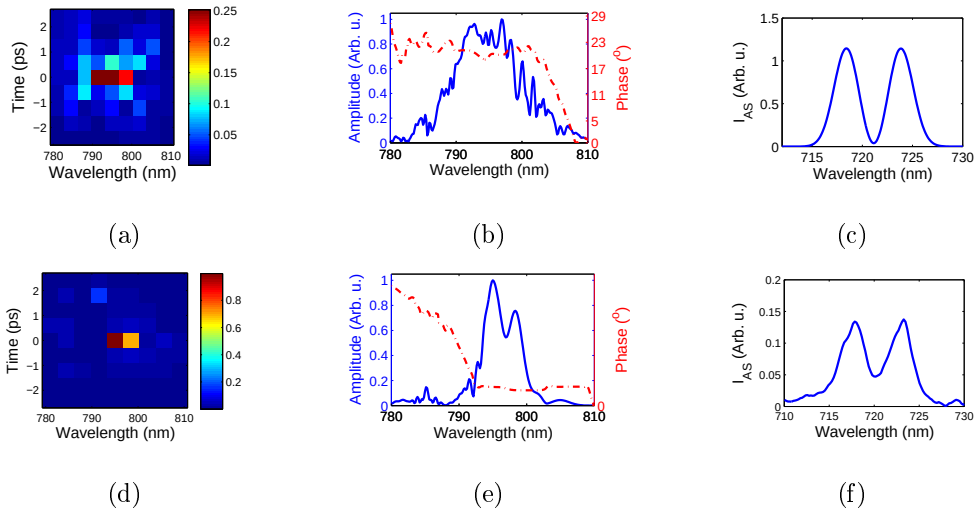

Figure 5.13: Simulation vs. Experiment for optimizing both modes as specified by the target function in equation 5.4. (a-c) Show the simulations while (d-f) show the experimentally obtained results. The pump field in the von Neumann basis (a) or its frequency domain counterpart (b) extracted during simulations leads to the CARS spectra in (c) exhibiting a small difference between the signal strength of the stretch and bend modes. (d) and (e) is the experimentally extracted pump field within the von Neumann representation and frequency domain which produced the CARS spectra in (f) also exhibiting a small difference in signal strength between the stretch and bend modes.

A notable difference between that the unshaped and shaped pump fields are the shaped fields results in lower CARS signals. This is a direct consequence of the target function chosen of which the main requirement was to minimize the difference between the amplitude of the stretch and bend mode.

5.4.2 TR-CARS (Coherence), Beat Contrast

Coherence between vibrational modes is a quantum mechanical feature which evolves over time. In this case coherence between the vibrational stretch and bend modes of CO_2 leads to the intensity of the CARS signals to fluctuate at a rate of 3.1 THz (322 fs between peaks of TR-CARS traces) as was shown in Fig. 5.7. As was shown previously (in section 4.4.4) the beat contrast between modes depends on the coherence between the modes as well as the intensity of each mode.

To the best of our knowledge there is no method currently in use which can enhance the beat contrast observed between the vibrational modes without making use of time-resolved spectroscopy. One can however change the relative intensity of the CARS signals associated with the two modes, which also influence the beat contrast. Comparing the beat contrast between the case of unshaped vs shaped pump fields allows us to observe the effects on the vibrational coherence of pulse shaping.

The first part of this section is dedicated to finding a pump field which will maximize the beat contrast in the intensity profiles (as a function of time) for the vibrational stretch and bend

modes of CO_2. As described in section 4.2.3 for time-resolved CARS the probe field is delayed while collecting frequency multiplex CARS spectra. The maximum value at each mode of the CARS signal is measured and collected for each delay time. The peak measured value of the CARS signal vs. time delay is collected for both modes. The learning algorithm is now used to find an optimized pump field based on the target function,

$$F = \frac{\max(peak1)\text{-}\min(\text{peak1})}{\text{mean}(peak1)} * \frac{\max(peak2)\text{-}\min(\text{peak2})}{\text{mean}(peak2)}. \tag{5.5}$$

Equation 5.5 attempts to increase both beat contrasts simultaneously. As expected, if only one mode is populated the beat in that mode disappears, making F zero. The results obtained for this target function is shown in Figure 5.14 (a) for simulations and Figure 5.14 (b) during experiments. (1) is the extracted pump field structure represented in the von Neumann basis while in (2) its frequency domain equivalence is shown. The pump fields extracted lead to the TR-CARS trace in (3). In (4) frequency slices are also selected from the spectrographs (in 3) resembling the maximum intensity at the stretch and bend modes.

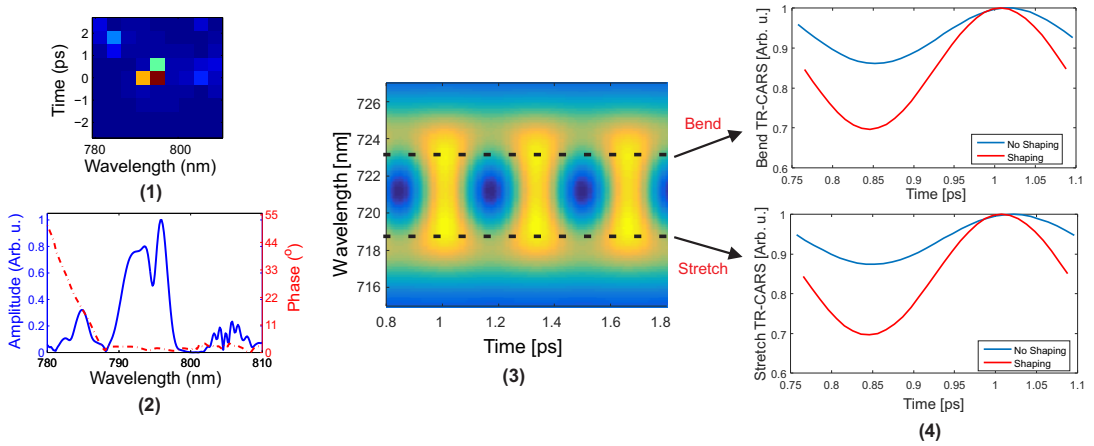

(a)

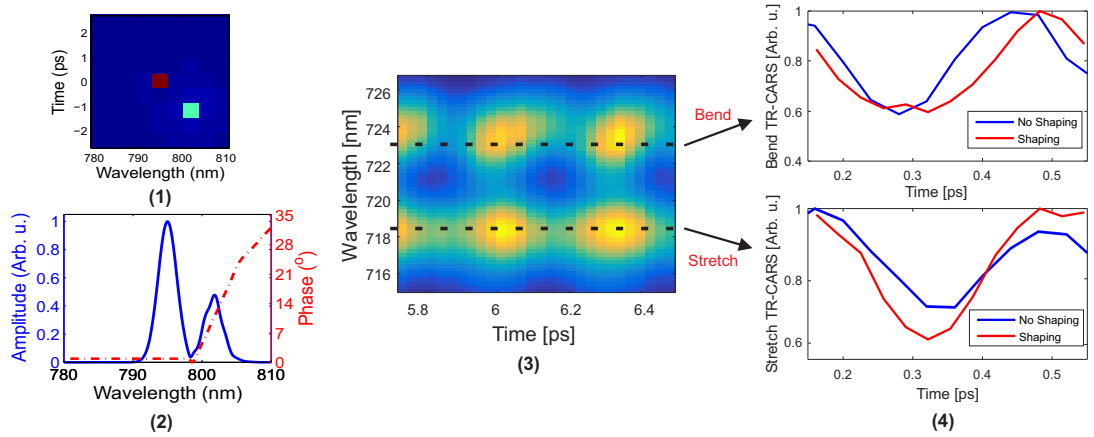

(b)

Figure 5.14: (a) Shows the simulated and (b) the experimental results obtained by the learning algorithm required to enhance the beat contrast within the TR-CARS spectrograph. In both cases (1) represents the von Neumann representation and (2) the Fourier representation of the extracted pump field. (3) Represents the TR-CARS spectrograph while (4) shows a temporal slice of (3) at the spectral location for both the bend and stretch modes compared to unshaped pulse fields. During simulations as well as experiments the shaped laser fields lead to a higher beat contrast in comparison to the unshaped cases.

During simulations the amplitude of the spectral components below 790 nm (predominantly on-resonant with the stretch mode) and above 799 nm (predominantly on-resonant with the bend mode) were suppressed. A spectral narrowband pump field will reduce the CARS signal strengths, but will also reduce the pump-Stokes frequency combinations on resonant with the various modes. As anticipated in section 4.4 this this type of behaviour leads to better beat contrast for the intensity of both the modes. Shown in Figure 5.14 (a4) the unshaped field exhibited a mode beating target value of 5.1e-3 while for a shaped laser field a higher target

values of 3.2e-2 was measured.

Similar results were obtained during experiments. The amplitude of the spectral components below 790 nm (predominantly on-resonant with the stretch mode) were suppressed. However, the spectral components above 799 nm (predominantly on-resonant with the bend mode) were temporally shifted so that no temporal overlap were achieved between these pump spectral components and the Stokes field. In essence this type of behaviour is equivalent to amplitude suppression found during simulations. In Figure 5.14 (b4) a slight increase can be observed during pulse shaping leading to a beating target value of 6.25e-2 relative to the case of no shaping of 4.46e-2. Even though the mechanisms are different for simulations and experiments both showed a larger beat amplitude for when using the extracted shaped pump fields in comparison to the case of using an unshaped pump field.

5.4.3 TR-CARS (Coherence), Phase Control

Finally we investigate whether our shaping capabilities allow control over the relative phase of oscillation of the bend vs. stretch mode. We conjectured that shifting the phase of the drive field resonant with the bend mode relative to that of the field resonant with the stretch mode would lead to a phase shift in the mode oscillation, and hence a phase shift in the beat pattern. This phase shift steps the direction of the electric field of that part of the frequency spectrum that is on resonant with the bend mode vs the stretch mode. Using a Gaussian pulse in amplitude while considering a phase shift of 0, $\pi/4$, $\pi/2$ and $3\pi/4$, as shown in Fig. 5.15(a), a temporal delay is observed for the simulated mode beating in Fig. 5.15(b). During experiments these phase values were applied to the pump field using a SLM which lead to the measured TR-CARS signal shown in Fig. 5.15(c). Changing the phase of the pump field influence the pump-Stokes overlap and consequently the intensity of the signals. At this stage of the study the signal intensity is not relevant such that the TR-CARS spectra in Figure 5.15 were all normalised relative to each other to reveal the effects of the pump phase on the coherence.

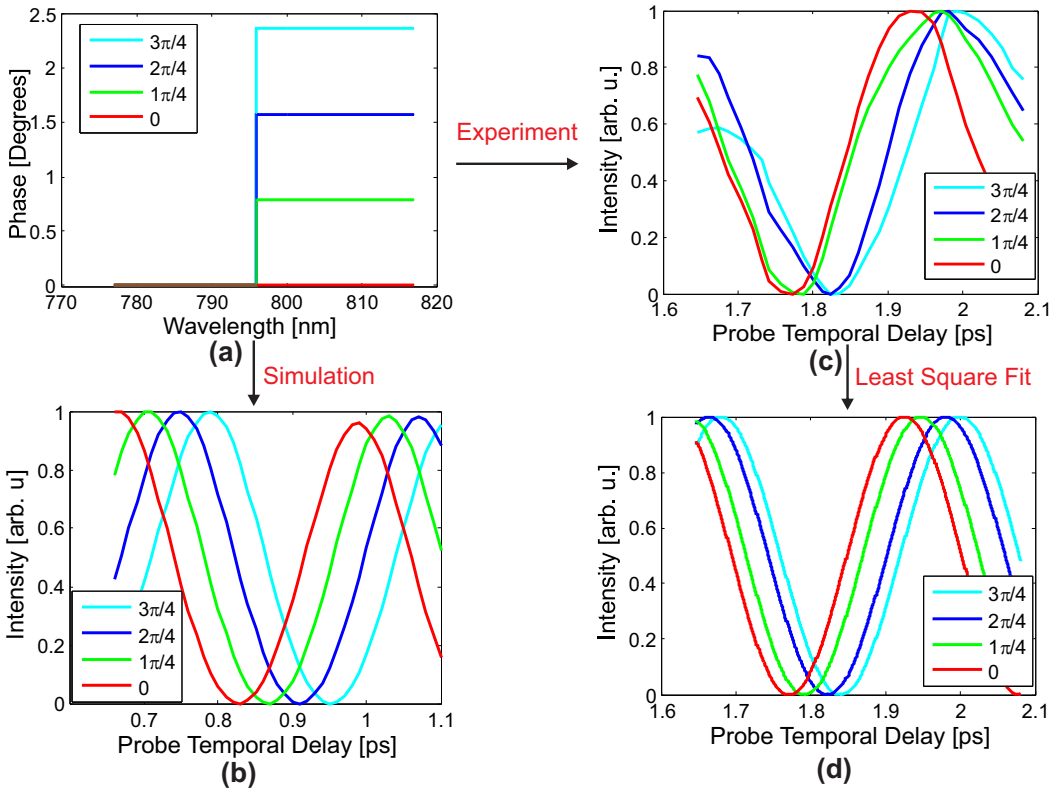

Figure 5.15: Changing the beat timing. Simulated results for when coherence will be created. (a) show the pump fields phase used while (b) show the TR-CARS traces measured for the stretch mode. Experimental results for when coherence will be created. (a) show the pump field phase while (c) show the measured TR-CARS traces. The variation in the traces were averaged out to only consider the temporal aspects of the traces.

A least square fit to the measure data can be seen in Figure 5.15(d). Similar to simulations Figure 5.15(c) and (d) show how the maximum value of the TR_CARS trace shifted forward (towards the right) in time with an increase in the phase jump value. Considering Figure 5.15 one once again sees good agreement between experiments and simulations. The temporal shift observed during experiments were however not as prominent as during simulations.

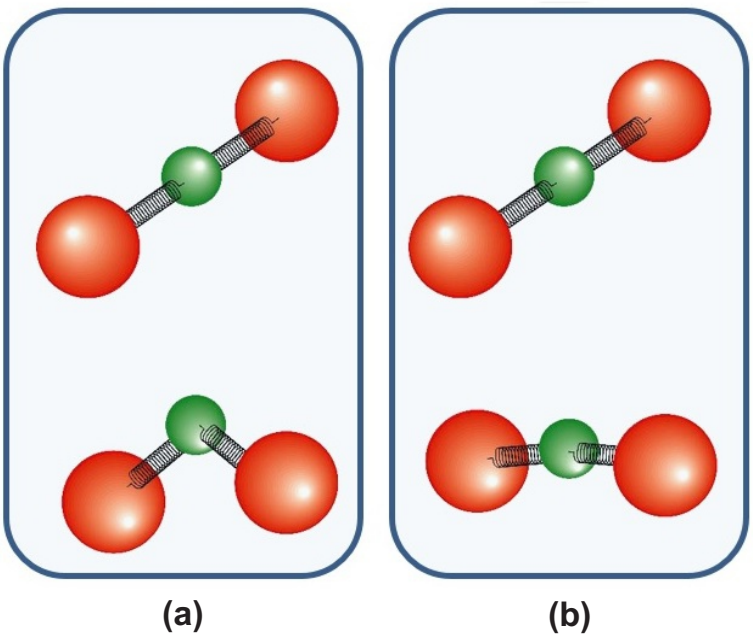

Figure 5.16: Relative phase between stretch and bend mode.

Physically what this means is that for the applied phase at a particular time you have that the molecule is fully stretched while also fully bent as shown in Fig. 5.16 (a) while in Fig. 5.16 (b) you have that the molecule is fully stretched while not bent when a πshift is made on the pump pulse. It was therefore possible to change the relative phase of vibration betwen the two modes. The work presented in this section demonstrates unambiguously that it was possible to manipulate the coherence created between vibrational modes of CO_2. It also shows excellent qualitative agreement between the theoretical model and the laboratory observations.

5.5 Summary

The aim of this chapter was to investigate to what extent one can control the vibrational modes of a molecule. The study clearly showed the selective excitation of two vibrational modes of CO_2 was achieved. It was not only possible to control the population of each mode, but using TR-CARS it was also possible to manipulate the coherence between the modes as well.

The learning algorithm clearly highlighted that both spectral as well as temporal attributes of the pump pulse played a big part in controlling the outcome. CARS is a process where the energy difference between a pump and Stokes field should match the energy required to excite a vibrational mode. Furthermore, due to the fact that no intermediate energy level is used during CARS it requires the pump and Stokes fields to temporally overlap. Therefore, vibrational excitation only occurred if the difference between the pump spectra and Stokes spectra matched the energy required for an excitation while the pump and Stokes field temporally overlapped. The learning algorithm made use of both spectral and temporal attributes of the pump to

populate and/or suppress the modes with no preference to any particular domain.

The experimental results were in good agreement with predictions from the theoretical model. The study also showed the theory developed in chapter 4 adequately model the vibrational behavior by directly using results obtained during simulations in experiments. This is a step in the right direction if one would like to completely control molecular excitations.

Chapter 6

Conclusion and Final Remarks

6.1 Summary and Conclusion

In summary, in this study we achieved coherent control of the vibrational quantum dynamics of CO_2 using the process of CARS. This was accomplished using a shaped broadband pump field and a narrowband Stokes field to selectively excite one of two vibrational modes of CO_2. Subsequently a narrowband probe field were used to de-excite the ensemble providing us with information of the modes populated as well as their dynamics. To experimentally find the pump pulse structure required for control a learning algorithm was developed which utilizes a SLM in a 4f-optical configuration to extract the pump shape. Both a time-frequency representation of the shaped pump pulse (called the von Neumann basis) and a standard Fourier domain representation were bench marked during optimization of a second harmonic generation (SHG) signal in a BBO crystal to ascertain which will suit the optimization problem best in terms of convergence rate and parameter space size. It was found that the von Neumann basis converged faster than the standard Fourier domain representation while still operating on a larger parameter space and therefore it was used to extract the pump fields which lead to selectivity.

The experimental work was accompanied by a quantum mechanical theoretical model we developed to compare and verify the results obtained. During both experiments and simulations we found the control mechanism for mode suppression is reducing the intensity that will be on resonant with the mode or by temporally shifting the onresonant frequency. We also showed control over the relative phase of oscillation of different vibrational modes. Our work demonstrates coherent quantum control of all relevant aspects of the molecular vibrational dynamics of two vibratoinal modes of CO_2.

6.2 Future Prospects with regards to Coherent Control

As mentioned, chemical reactions rely on the environment created before and/or during the time the reaction takes place. The study of using light to prepare molecules in states that favour particular chemical reaction path-ways plays a crucial role in understanding chemical reactions.

The work presented here lays the groundwork for our longterm objectives to manipulate chemical reaction dynamics. However, the work presented here only considered two modes of CO_2 which limits the information attainable when looking for path-ways towards several different chemical reactions. As example the work presented by Fleming and coworkers [8] showed 3rd overtone excitation of the stretch OD mode is required for the desired reaction path-way to be initiated. In the work presented by Zare [4] it was shown that different vibrational excitations of different molecules lead to different path-ways. A complete study of chemical reaction path-ways can only be conducted if complete control of all possible excitations can be achieved. For the work presented here it implies that not only the two modes investigated should be considered, but that overtone excitations, combination of modes as well as infrared (IR) excitations should all be considered.

Bibliography

[1] Antoine Monmayrant, Sébastien Weber, and Béatrice Chatel. A newcomer's guide to ultrashort pulse shaping and characterization. *Journal of Physics B: Atomic, Molecular and Optical Physics*, 43(10):103001, 2010.

[2] Sukesh Roy, Paul J. Wrzesinski, Dmitry Pestov, Marcos Dantus, and James R. Gord. Single-beam coherent anti-stokes raman scattering (CARS) spectroscopy of gas-phase CO2 via phase and polarization shaping of a broadband continuum. *Journal of Raman Spectroscopy*, 41(10):1194–1199, 2010.

[3] http://www.chem.latech.edu/ upali/chem281/notes/ch2-mo-theory.pdf.

[4] Richard N Zare. Laser control of chemical reactions. *Science*, 279(5358):1875–1879, 1998.

[5] Patrick Nuernberger, Gerhard Vogt, Tobias Brixner, and Gustav Gerber. Femtosecond quantum control of molecular dynamics in the condensed phase. *Physical Chemistry Chemical Physics*, 9(20):2470–2497, 2007.

[6] Patrick Nuernberger, Daniel Wolpert, Horst Weiss, and Gustav Gerber. Femtosecond quantum control of molecular bond formation. *Proceedings of the National Academy of Sciences*, 107(23):10366–10370, 2010.

[7] Anton Du Plessis, Christien Strydom, and Lourens Botha. Comparative study of the dissociative ionization of 1, 1, 1 trichloroethane using nanosecond and femtosecond laser pulses. *International journal of molecular sciences*, 11(3):1114–1140, 2010.

[8] Amitabha Sinha, Mark C Hsiao, and F Fleming Crim. Bond-selected bimolecular chemistry: H+HOD(4vOH)-> OD+H2. *The Journal of Chemical Physics*, 92(10):6333–6335, 1990.

[9] Amitabha Sinha, John D Thoemke, and F Fleming Crim. Controlling bimolecular reactions: Mode and bond selected reaction of water with translationally excited chlorine atoms. *The Journal of chemical physics*, 96(1):372–376, 1992.

[10] Christoph Kreher, Robert Theinl, and Karl-Heinz Gericke. State-to-state reaction dynamics of R+ HCN (v1vl22v3)-> RH+ CN (v, J) with R= Cl, H. *The Journal of chemical physics*, 104(12):4481–4489, 1996.

[11] Randy Alan Bartels. *Coherent control of atoms and molecules*. PhD thesis, The University of Michigan, 2002.

[12] David C Clary. Quantum dynamics of chemical reactions. *Science*, 321(5890):789–791, 2008.

[13] Denis L Rousseau. Laser chemistry. *Journal of Chemical Education*, 43(11):566, 1966.

[14] Nicolaas Bloembergen and Ahmed H Zewail. Energy redistribution in isolated molecules and the question of mode-selective laser chemistry revisited. new experiments on the dynamics of collisionless energy redistribution in molecules possibilities for laser-selective chemistry with subpicosecond pulses. *The Journal of Physical Chemistry*, 88(23):5459–5465, 1984.

[15] David J Tannor and Stuart A Rice. Control of selectivity of chemical reaction via control of wave packet evolution. *The Journal of chemical physics*, 83(10):5013–5018, 1985.

[16] David J Tannor, Ronnie Kosloff, and Stuart A Rice. Coherent pulse sequence induced control of selectivity of reactions: Exact quantum mechanical calculations. *The Journal of chemical physics*, 85(10):5805–5820, 1986.

[17] T Baumert, M Grosser, R Thalweiser, and G Gerber. Femtosecond time-resolved molecular multiphoton ionization: The Na2 system. *Physical review letters*, 67(27):3753, 1991.

[18] ED Potter, Q Liu, and AH Zewail. Femtosecond reaction dynamics in macroclusters. effect of solvation on wave-packet motion. *Chemical physics letters*, 200(6):605–614, 1992.

[19] Paul Brumer and Moshe Shapiro. Control of unimolecular reactions using coherent light. *Chemical physics letters*, 126(6):541–546, 1986.

[20] Ce Chen, Yi-Yian Yin, and DS Elliott. Interference between optical transitions. *Physical review letters*, 64(5):507, 1990.

[21] JR Kuklinski, U Gaubatz, Foek T Hioe, and K Bergmann. Adiabatic population transfer in a three-level system driven by delayed laser pulses. *Physical Review A*, 40(11):6741, 1989.

[22] Vadim V. Lozovoy, Yair Andegeko, Xin Zhu, and Marcos Dantus. Applications of ultrashort shaped pulses in microscopy and for controlling chemical reactions. *CHEMICAL PHYSICS*, 350(1-3):118–124, JUN 23 2008. 8th International Conference on Femtochemistry and Femtobiology, Magdalen Coll, Oxford, ENGLAND, JUL 22-27, 2007.

[23] Marcos Dantus, RM Bowman, and AH Zewail. Femtosecond laser observations of molecular vibration and rotation. *Nature*, 343(6260):737, 1990.

[24] S Adhikari, Sarin Deshpande, Manabendra Sarma, Vandana Kurkal, and MK Mishra. Selective control of photodissociation in deutereted water molecule HOD. *Radiation Physics and Chemistry*, 75(12):2106–2118, 2006.

[25] Li-Ping Ju, Ke-Li Han, and John Z. H. Zhang. Global dynamics and transition state theories: Comparative study of reaction rate constants for gas-phase chemical reactions. *Journal of Computational Chemistry*, 30(2):305–316, 2009.

[26] David C Clary. Theoretical studies on bimolecular reaction dynamics. *Proceedings of the National Academy of Sciences*, 105(35):12649–12653, 2008.

[27] C Kreher, JL Rinnenthal, and KH Gericke. Vibrational state control of bimolecular reactions. *JOURNAL OF CHEMICAL PHYSICS*, 108(8):3154–3167, FEB 22 1998.

[28] Brad Lehman, Irwan Widjaya, and Khalil Shujaee. Application of vibrational control to chemical reactions in a CSIR with delayed recycle stream. In *Proceedings of the American Control Conference*, pages 3538–3542, 1994.

[29] M Agúndez, JR Goicoechea, J Cernicharo, A Faure, and E Roueff. The chemistry of vibrationally excited H2 in the interstellar medium. *The Astrophysical Journal*, 713(1):662, 2010.

[30] FF Crim. Bond-selected chemistry: Vibrational state control of photodissociation and bimolecular reaction. *JOURNAL OF PHYSICAL CHEMISTRY*, 100(31):12725–12734, AUG 1 1996.

[31] F Fleming Crim. Vibrational state control of bimolecular reactions: Discovering and directing the chemistry. *Accounts of chemical research*, 32(10):877–884, 1999.

[32] Una Marvet and Marcos Dantus. Femtosecond photoassociation spectroscopy: coherent bond formation. *Chemical physics letters*, 245(4):393–399, 1995.

[33] Una Marvet, Qingguo Zhang, Emily J Brown, and Marcos Dantusb. Femtosecond dynamics of photoinduced molecular detachment from halogenated alkanes. i. transition state dynamics and product channel coherence. *spectroscopy*, 2:9, 1998.

[34] JP Heritage, RN Thurston, WJ Tomlinson, AM Weiner, and RH Stolen. Spectral windowing of frequency-modulated optical pulses in a grating compressor. *Applied Physics Letters*, 47(2):87–89, 1985.

[35] Richard S Judson and Herschel Rabitz. Teaching lasers to control molecules. *Physical Review Letters*, 68(10):1500, 1992.

[36] Randy Bartels, S Backus, E Zeek, L Misoguti, G Vdovin, IP Christov, MM Murnane, and HC Kapteyn. Shaped-pulse optimization of coherent emission of high-harmonic soft x-rays. *Nature*, 406(6792):164–166, 2000.

[37] D Meshulach, D Yelin, and Y Silberberg. Adaptive real-time femtosecond pulse shaping. *JOSA B*, 15(5):1615–1619, 1998.

[38] Jerry Prawiharjo, Nikita K Daga, Rui Geng, Jonathan H Price, David C Hanna, David J Richardson, and David P Shepherd. High fidelity femtosecond pulses from an ultrafast fiber laser system via adaptive amplitude and phase pre-shaping. *Optics express*, 16(19):15074–15089, 2008.

[39] Kimihisa Ohno, Takasumi Tanabe, and Fumihiko Kannari. Adaptive pulse shaping of phase and amplitude of an amplified femtosecond pulse laser by direct reference to frequency-resolved optical gating traces. *JOSA B*, 19(11):2781–2790, 2002.

[40] Nina Owschimikow, Burkhard Schmidt, and Nikolaus Schwentner. Laser-induced alignment and anti-alignment of rotationally excited molecules. *Physical Chemistry Chemical Physics*, 13(19):8671–8680, 2011.

[41] JH Posthunus, J Plumridge, K Codling, LJ Frasinski, AJ Langley, and PF Taday. Alignment of molecules on a vibrational timescale. *LASER PHYSICS-LAWRENCE-*, 9:163–170, 1999.

[42] Paweł Wnuk and Czesław Radzewicz. Coherent control and dark pulses in second harmonic generation. *Optics Communications*, 272(2):496–502, 2007.

[43] Vlado Zeman, Moshe Shapiro, and Paul Brumer. Coherent control of resonance-mediated reactions: F + HD. *Phys. Rev. Lett.*, 92:133204, Apr 2004.

[44] Christopher J Bardeen, Vladislav V Yakovlev, Kent R Wilson, Scott D Carpenter, Peter M Weber, and Warren S Warren. Feedback quantum control of molecular electronic population transfer. *Chemical Physics Letters*, 280(1):151–158, 1997.

[45] D Zeidler, S Frey, W Wohlleben, M Motzkus, F Busch, T Chen, W Kiefer, and A Materny. Optimal control of ground-state dynamics in polymers. *The Journal of chemical physics*, 116(12):5231–5235, 2002.

[46] A Rodenberg, S Fechner, F Dimler, DJ Tannor, and T Brixner. Experimental implementation of ultrashort laser pulses in the von Neumann picture. *Applied Physics B*, 93(4):763–772, 2008.

[47] Stefan Ruetzel, Christoph Stolzenberger, Susanne Fechner, Frank Dimler, Tobias Brixner, and David J Tannor. Molecular quantum control landscapes in von neumann time-frequency phase space. *The Journal of chemical physics*, 133(16):164510, 2010.

[48] WD Kulatilaka, JR Gord, and S Roy. Effects of O2–CO2 polarization beating on femtosecond coherent anti-Stokes Raman scattering (fs-CARS) spectroscopy of O2. *Applied Physics B*, 102(1):141–147, 2011.

[49] Claude Rulliere et al. *Femtosecond laser pulses*. Springer, 2005.

[50] Gavin D Reid and Klaas Wynne. Ultrafast laser technology and spectroscopy. *Encyclopedia of Analytical chemistry*, 2000.

[51] Malvin Carl Teich and BEA Saleh. Fundamentals of photonics. *Canada, Wiley Interscience*, 3, 1991.

[52] Stefan Witte and Kjeld SE Eikema. Ultrafast optical parametric chirped-pulse amplification. *IEEE Journal of Selected Topics in Quantum Electronics*, 18(1):296–307, 2012.

[53] Frederic Verluise, Vincent Laude, Z Cheng, Ch Spielmann, and Pierre Tournois. Amplitude and phase control of ultrashort pulses by use of an acousto-optic programmable dispersive filter: pulse compression and shaping. *Optics letters*, 25(8):575–577, 2000.

[54] Nicholas T Form, Robert Burbidge, Jan Ramon, and Benjamin J Whitaker. Parameterization of an acousto-optic programmable dispersive filter for closed-loop learning experiments. *Journal of Modern Optics*, 55(1):197–209, 2008.

[55] Rick Trebino. *FROG*. Springer, 2000.

[56] A Galler and T Feurer. Pulse shaper assisted short laser pulse characterization. *Applied Physics B*, 90(3-4):427–430, 2008.

[57] Andrew M Weiner. Ultrafast optical pulse shaping: A tutorial review. *Optics Communications*, 284(15):3669–3692, 2011.

[58] Tobias Brixner and Gustav Gerber. Quantum control of gas-phase and liquid-phase femtochemistry. *ChemPhysChem*, 4(5):418–438, 2003.

[59] Herschel A Rabitz, Michael M Hsieh, and Carey M Rosenthal. Quantum optimally controlled transition landscapes. *Science*, 303(5666):1998–2001, 2004.

[60] Thomas Bäck, Günter Rudolph, and Hans-Paul Schwefel. Evolutionary programming and evolution strategies: Similarities and differences. In *In Proceedings of the Second Annual Conference on Evolutionary Programming*. Citeseer, 1993.

[61] Alexander CW van Rhijn, Herman L Offerhaus, Peter van der Walle, Jennifer L Herek, and Aliakbar Jafarpour. Exploring, tailoring, and traversing the solution landscape of a phase-shaped CARS process. *Optics express*, 18(3):2695–2709, 2010.

[62] Sung-Hyuk Cha and Charles Tappert. A genetic algorithm for constructing compact binary decision trees. *Journal of Pattern Recognition Research*, 4(1):1–13, 2009.

[63] Russell R Barton and John S Ivey Jr. Nelder-mead simplex modifications for simulation optimization. *Management Science*, 42(7):954–973, 1996.

[64] Reza Akbari and Koorush Ziarati. A multilevel evolutionary algorithm for optimizing numerical functions. *International Journal of Industrial Engineering Computations*, 2(2):419–430, 2011.

[65] Reuven Eitan, Michael Mundt, and David J Tannor. Optimal control with accelerated convergence: Combining the krotov and quasi-newton methods. *Physical Review A*, 83(5):053426, 2011.

[66] A Chipperfield, P Fleming, H Pohlheim, and H Fonseca. *Genetic Algorithm TOOLBOX*. Matlab, 1.2 edition.

[67] K-H Hong, J-H Kim, Yong Hoon Kang, and Chang Hee Nam. Time–frequency analysis of chirped femtosecond pulses using wigner distribution function. *Applied Physics B*, 74(1):s231–s236, 2002.

[68] Susanne Fechner, Frank Dimler, Tobias Brixner, Gustav Gerber, and David J Tannor. The von neumann picture: a new representation for ultrashort laser pulses. *Optics express*, 15(23):15387–15401, 2007.

[69] Frank Dimler, Susanne Fechner, Alexander Rodenberg, Tobias Brixner, and David J Tannor. Accurate and efficient implementation of the von neumann representation for laser pulses with discrete and finite spectra. *New Journal of Physics*, 11(10):105052, 2009.

[70] VV Lozovoy and M Dantus. Coherent control in femtochemistry. *Chemphyschem*, 6(10):1970–2000, 2005.

[71] Abigail Nunn. *Experimental and theoretical investigations of the photochemistry of styrene and the creation and characterisation of shaped femtosecond ultraviolet laser pulses*. PhD thesis, UCL (University College London), 2010.

[72] R Simon and N Mukunda. Optical phase space, wigner representation, and invariant quality parameters. *JOSA A*, 17(12):2440–2463, 2000.

[73] T Baumert, T Brixner, V Seyfried, M Strehle, and G Gerber. Femtosecond pulse shaping by an evolutionary algorithm with feedback. *Applied Physics B: Lasers and Optics*, 65(6):779–782, 1997.

[74] Robert W Boyd. *Nonlinear Optics (Academic, New York, 1992)*, volume 8. 1992.

[75] B Fabre, JH Posthumus, V Adrianarijaona, J Jureta, and X Urbain. The vibrational excitation of after multiphoton ionization of H2. *Laser physics*, 13(7):964–974, 2003.

[76] G-Y Chen, ZW Wang, and WT Hill III. Adaptive control of the CO2 bending vibration: Deciphering field-system dynamics. *Physical Review A*, 79(1):011401, 2009.

[77] Igor Dotsenko. Raman spectroscopy of single atoms. *Diplom Theses, Bonn University*, 2002.

[78] Meng Cui. *Coherent Raman scattering: applications in imaging and sensing*. ProQuest, 2009.

[79] Fouad El-Diasty. Coherent anti-stokes raman scattering: spectroscopy and microscopy. *Vibrational Spectroscopy*, 55(1):1–37, 2011.

[80] Nadia Djaker, Pierre-François Lenne, Didier Marguet, Anne Colonna, Christophe Hadjur, and Hervé Rigneault. Coherent anti-Stokes Raman scattering microscopy (CARS):

Instrumentation and applications. *Nuclear Instruments and Methods in Physics Research Section A: Accelerators, Spectrometers, Detectors and Associated Equipment*, 571(1):177–181, 2007.

[81] Chandrasekhara Venkata Raman and Kariamanikkam Srinivasa Krishnan. A new type of secondary radiation. *Nature*, 121(3048):501–502, 1928.

[82] PD Maker and RW Terhune. Study of optical effects due to an induced polarization third order in the electric field strength. *Physical Review*, 137(3A):A801, 1965.

[83] RF Begley, AB Harvey, and Robert L Byer. Coherent anti-stokes raman spectroscopy. *Applied Physics Letters*, 25(7):387–390, 1974.

[84] Robert P Lucht, Sukesh Roy, Terrence R Meyer, and James R Gord. Femtosecond coherent anti-Stokes Raman scattering measurement of gas temperatures from frequency-spread dephasing of the Raman coherence. *Applied Physics Letters*, 89(25):251112, 2006.

[85] Conor L Evans and X Sunney Xie. Coherent anti-stokes raman scattering microscopy: chemical imaging for biology and medicine. *Annu. Rev. Anal. Chem.*, 1:883–909, 2008.

[86] Ji-Xin Cheng. Coherent anti-stokes raman scattering microscopy. In *Conference on Lasers and Electro-Optics*, page JWC2. Optical Society of America, 2008.

[87] Haowen Li, D Ahmasi Harris, Bingwei Xu, Paul J Wrzesinski, Vadim V Lozovoy, and Marcos Dantus. Standoff and arms-length detection of chemicals with single-beam coherent anti-stokes raman scattering. *Applied optics*, 48(4):B17–B22, 2009.

[88] David J Tannor et al. *Introduction to quantum mechanics*, volume 75. 2007.

[89] Wolfgang Demtröder. *Laser spectroscopy: basic concepts and instrumentation*. Springer Science & Business Media, 2013.

[90] VI Fabelinsky, BB Krynetsky, LA Kulevsky, VA Mishin, AM Prokhorov, AD Savel'Ev, and VV Smirnov. High resolution cw cars spectroscopy of the q-branch of the $\nu 2$ band in C2H2. *Optics Communications*, 20(3):389–391, 1977.

[91] Michael D Duncan, J Reintjes, and TJ Manuccia. Scanning coherent anti-Stokes Raman microscope. *Optics letters*, 7(8):350–352, 1982.

[92] Matthias Lütgens, Susana Chatzipapadopoulos, and Stefan Lochbrunner. Coherent anti-stokes raman scattering with broadband excitation and narrowband probe. *Optics express*, 20(6):6478–6487, 2012.

[93] H Graener and A Laubereau. High-resolution fourier transform raman spectroscopy with ultrashort laser pulses. In *Time-Resolved Vibrational Spectroscopy*, pages 11–14. Springer, 1985.

[94] Günther Krauss, Tobias Hanke, Alexander Sell, Daniel Träutlein, Alfred Leitenstorfer, Romedi Selm, Martin Winterhalder, and Andreas Zumbusch. Compact coherent anti-Stokes Raman scattering microscope based on a picosecond two-color Er: fiber laser system. *Optics letters*, 34(18):2847–2849, 2009.

[95] Shian Zhang, Liang Zhang, Xiangyun Zhang, Litao Ding, Guoliang Chen, Zhenrong Sun, and Zugeng Wang. Selective excitation of CARS by adaptive pulse shaping based on genetic algorithm. *Chemical physics letters*, 433(4):416–421, 2007.

[96] Aleksei M Zheltikov and Aleksandr Nikolaevich Naumov. High-resolution four-photon spectroscopy with chirped pulses. *Quantum Electronics*, 30(7):606, 2000.

[97] Peter Schön. *Phase and Polarization Pulse Shaping for Nonlinear Microscopy.* PhD thesis, Université Paul Cézanne-Aix-Marseille III, 2010.

[98] Jean-Louis Oudar, Robert W Smith, and YR Shen. Polarization-sensitive coherent anti-stokes raman spectroscopy. *Applied Physics Letters*, 34(11):758–760, 1979.

[99] Alan C Eckbreth and Robert J Hall. Cars concentration sensitivity with and without nonresonant background suppression. 1981.

[100] Dan Oron, Nirit Dudovich, and Yaron Silberberg. Femtosecond phase-and-polarization control for background-free coherent anti-Stokes Raman spectroscopy. *Physical Review Letters*, 90(21):213902, 2003.

[101] Dr. Alessandro Massaro. *Photonic Crystals - Innovative Systems, Lasers and Waveguides.* InTech, 2012.

[102] AHMEDH ZEWAIL. Laser femtochemistry. *Science*, 242(4886):1645–1653, 1988.

[103] Todd S Rose, Mark J Rosker, and Ahmed H Zewail. Femtosecond real-time observation of wave packet oscillations (resonance) in dissociation reactions. *The Journal of Chemical Physics*, 88(10):6672–6673, 1988.

[104] M Karavitis, R Zadoyan, and V Ara Apkarian. Time resolved coherent anti-stokes raman scattering of I2 isolated in matrix argon: Vibrational dynamics on the ground electronic state. *The Journal of Chemical Physics*, 114(9):4131–4140, 2001.

[105] Nirit Dudovich, Dan Oron, and Yaron Silberberg. Single-pulse coherently controlled nonlinear raman spectroscopy and microscopy. *Nature*, 418(6897):512–514, 2002.

[106] PR Regnier and JP-E Taran. On the possibility of measuring gas concentrations by stimulated anti-stokes scattering. *Applied Physics Letters*, 23(5):240–242, 1973.

[107] Hongqun Yang, Zhenghe Xu, Maohong Fan, Rajender Gupta, Rachid B Slimane, Alan E Bland, and Ian Wright. Progress in carbon dioxide separation and capture: A review. *Journal of Environmental Sciences*, 20(1):14–27, 2008.

[108] Zou Yong, Vera Mata, and Alı' rio E Rodrigues. Adsorption of carbon dioxide at high temperature-a review. *Separation and Purification Technology*, 26(2):195–205, 2002.

[109] Klaus S Lackner, Christopher H Wendt, Darryl P Butt, Edward L Joyce, and David H Sharp. Carbon dioxide disposal in carbonate minerals. *Energy*, 20(11):1153–1170, 1995.

[110] Le Minh Tuyen H. *Electrochemical Reduction of CO2 to Methanol.* PhD thesis, Louisiana State University and, 2011.

[111] Barbara Stuart. *Infrared spectroscopy.* Wiley Online Library, 2005.

[112] Roger L DeKock and Harry B Gray. *Chemical structure and bonding.* University Science Books, 1989.

[113] Linus Pauling. *The nature of the chemical bond and the structure of molecules and crystals: an introduction to modern structural chemistry*, volume 18. Cornell university press, 1960.

[114] S Cvejanovic and J Jureta. Threshold spectrum of co2. *Journal of Physics B: Atomic and Molecular Physics*, 18(12):2541, 1985.

[115] M Lewis, ZY Wu, and R Glaser. Polarizabilities of carbon dioxide and carbodiimide. Assessment of theoretical model dependencies on dipole polarizabilities and dipole polarizability anisotropies. *JOURNAL OF PHYSICAL CHEMISTRY A*, 104(48):11355–11361, DEC 7 2000.

[116] Gerhard Herzberg. *Molecular spectra and molecular structure*, volume 1. Read Books Ltd, 2013.

[117] Paul J Wrzesinski, Dmitry Pestov, Vadim V Lozovoy, Bingwei Xu, Sukesh Roy, James R Gord, and Marcos Dantus. Binary phase shaping for selective single-beam cars spectroscopy and imaging of gas-phase molecules. *Journal of Raman Spectroscopy*, 42(3):393–398, 2011.

[118] R Naaman, DM Lubman, and RN Zare. Vibrational energy redistribution in glyoxal following internal conversion. *The Journal of Chemical Physics*, 71(11):4192–4200, 1979.

[119] W Demtröder. Springer series in chemical physics. In *Laser spectroscopy*, volume 5, page 107. Springer Berlin, 1982.

[120] Xiaoji Xu. New methods of coherent anti-stokes raman spectroscopy based on broadband pulses. 2009.

[121] Alexander Abrashkevich, Moshe Shapiro, and Paul Brumer. Coherent control of reactive scattering. *Physical review letters*, 81(17):3789, 1998.

[122] Simon T Banks and David C Clary. Reduced dimensionality quantum dynamics of Cl+CH4-> HCl+CH3 on an ab initio potential. *Physical Chemistry Chemical Physics*, 9(8):933–943, 2007.

[123] Joel M Bowman. Reduced dimensionality theory of quantum reactive scattering. *The Journal of Physical Chemistry*, 95(13):4960–4968, 1991.

[124] T Brixner, A Oehrlein, M Strehle, and G Gerber. Feedback-controlled femtosecond pulse shaping. *APPLIED PHYSICS B-LASERS AND OPTICS*, 70(S):S119–S124, JUN 2000. Ultrafast Optics 1999 Meeting, CTR STEFANO FRANSCINI, ASCONA, SWITZERLAND, JUL 12-16, 1999.

[125] RJ Buenker, M Honigmann, HP Liebermann, and M Kimura. Theoretical study of the electronic structure of carbon dioxide: Bending potential curves and generalized oscillator strengths. *JOURNAL OF CHEMICAL PHYSICS*, 113(3):1046–1054, JUL 15 2000.

[126] E. K. Campbell, A. B. Alekseyev, G. G. Balint-Kurti, M. Brouard, Alex Brown, R. J. Buenker, A. J. Johnsen, D. B. Kokh, S. Lucas, and B. Winter. The vibrationally mediated photodissociation of Cl-2. *JOURNAL OF CHEMICAL PHYSICS*, 137(12), SEP 28 2012.

[127] Ji-Xin Cheng, Lewis D Book, and X Sunney Xie. Polarization coherent anti-stokes raman scattering microscopy. *Optics letters*, 26(17):1341–1343, 2001.

[128] David C Clary. Quantum dynamics of the O(3P)+CH4-> CH3+OH reaction. *Physical Chemistry Chemical Physics*, 1(6):1173–1179, 1999.

[129] David C Clary. Quantum theory of chemical reaction dynamics. *Science*, 279(5358):1879–1882, 1998.

[130] Chantal Daniel, Jürgen Full, Leticia González, Cosmin Lupulescu, Jörn Manz, Andrea Merli, Štefan Vajda, and Ludger Wöste. Deciphering the reaction dynamics underlying optimal control laser fields. *Science*, 299(5606):536–539, 2003.

[131] A Efimov and DH Reitze. Programmable dispersion compensation and pulse shaping in a 26-fs chirped-pulse amplifier. *OPTICS LETTERS*, 23(20):1612–1614, OCT 15 1998.

[132] Conor L Evans, Xiaoyin Xu, Santosh Kesari, X Sunney Xie, Steven TC Wong, and Geoffrey S Young. Chemically-selective imaging of brain structures with cars microscopy. *Optics express*, 15(19):12076–12087, 2007.

[133] J-M Hartmann and C Boulet. Molecular dynamics simulations for CO2 spectra. iii. permanent and collision-induced tensors contributions to light absorption and scattering. *The Journal of chemical physics*, 134(18):184312, 2011.

[134] Robert C Hilborn. Einstein coefficients, cross sections, f values, dipole moments, and all that. *arXiv preprint physics/0202029*, 2002.

[135] Julien Lamouroux, J-M Hartmann, Ha Tran, Bruno Lavorel, Marcel Snels, Stephania Stefani, and Giuseppe Piccioni. Molecular dynamics simulations for CO2 spectra. iv. collisional line-mixing in infrared and raman bands. *The Journal of chemical physics*, 138(24):244310, 2013.

[136] Haowen Li, D Ahmasi Harris, Bingwei Xu, Paul J Wrzesinski, Vadim V Lozovoy, and Marcos Dantus. Coherent mode-selective Raman excitation towards standoff detection. *Optics express*, 16(8):5499–5504, 2008.

[137] Vadim V Lozovoy, Xin Zhu, Tissa C Gunaratne, D Ahmasi Harris, Janelle C Shane, and Marcos Dantus. Control of molecular fragmentation using shaped femtosecond pulses. *The Journal of Physical Chemistry A*, 112(17):3789–3812, 2008.

[138] S. Ruetzel, A. Krischke, and T. Brixner. The von Neumann representation as a joint time-frequency parameterization for polarization-shaped femtosecond laser pulses. *APPLIED PHYSICS B-LASERS AND OPTICS*, 107(1):1–9, APR 2012.

[139] Stefan Ruetzel, Christoph Stolzenberger, Frank Dimler, David J Tannor, and Tobias Brixner. Adaptive coherent control using the von neumann basis. *Physical Chemistry Chemical Physics*, 13(19):8627–8636, 2011.

[140] Janelle C Shane, Vadim V Lozovoy, and Marcos Dantus. Search space mapping: getting a picture of coherent laser control. *The Journal of Physical Chemistry A*, 110(40):11388–11391, 2006.

[141] ShuFeng Wang and QiHuang Gong. Progress in femtochemistry and femtobiology. *Science China Physics, Mechanics and Astronomy*, 54(12):2103–2108, 2011.

[142] E Wells, J McKenna, AM Sayler, Bethany Jochim, Neal Gregerson, R Averin, M Zohrabi, KD Carnes, and I Ben-Itzhak. Closed-loop control of vibrational population in CO2+. *Journal of Physics B: Atomic, Molecular and Optical Physics*, 43(1):015101, 2010.

[143] E Woods, HL Berghout, CM Cheatum, and FF Crim. Controlling the bimolecular reaction and photodissociation of HNCO through selective excitation of perturbed vibrational states. *JOURNAL OF PHYSICAL CHEMISTRY A*, 104(45):10356–10361, NOV 16 2000.

[144] Sangwoon Yoon, Robert J Holiday, and F Fleming Crim. Vibrationally controlled chemistry: Mode-and bond-selected reaction of CH3D with Cl. *The Journal of Physical Chemistry B*, 109(17):8388–8392, 2005.

[145] Janne Savolainen, Riccardo Fanciulli, Niels Dijkhuizen, Ana L Moore, Jürgen Hauer, Tiago Buckup, Marcus Motzkus, and Jennifer L Herek. Controlling the efficiency of an artificial light-harvesting complex. *Proceedings of the National Academy of Sciences*, 105(22):7641–7646, 2008.

[146] VV Smirnov and VI Fabelinskii. Measurement of the temperature and spectroscopy of discharge-excited vibrational-rotational states by the CARS method. *ZhETF Pisma Redaktsiiu*, 28:461, 1978.

[147] Vadim V Lozovoy, Yair Andegeko, Xin Zhu, and Marcos Dantus. Applications of ultrashort shaped pulses in microscopy and for controlling chemical reactions. *Chemical Physics*, 350(1):118–124, 2008.

[148] Marija Kotur, Thomas Weinacht, Brett J Pearson, and Spiridoula Matsika. Closed-loop learning control of isomerization using shaped ultrafast laser pulses in the deep ultraviolet. *The Journal of chemical physics*, 130(13):134311, 2009.

Appendix A

Mathematical Preliminaries

A.1 Maths

A.1.1 Tensor calculations used

The following mathematical relations were used within this thesis

$$\nabla_i \equiv \frac{\partial}{\partial x_i} + \frac{\partial}{\partial y_i} + \frac{\partial}{\partial z_i}$$

A.1.2 Solving first order differential equations

If we have

$$y'(t) + p(t)\, y(t) = g(t) \tag{A.1}$$

Then $y(t)$ can be expressed as

$$y(t) = \frac{\int u(t)\, g(t)\, dt + c}{u(t)} \tag{A.2}$$

where we have

$$u(t) = e^{\int p(t)dt + k} \tag{A.3}$$

A.1.3 Integration over a negative area

$$\int_{-\infty}^{0} \frac{E(\omega)e^{-it\omega}}{(\omega_n - \omega)} d\omega = \int_{0}^{\infty} \frac{E*(\omega)e^{it\omega}}{(\omega_n + \omega)} d\omega \tag{A.4}$$